Time-resolved imaging of guided wave phenomena

Harikumar K Chandrasekharan

Submitted for the degree of Doctor of Philosophy

Heriot-Watt University
School of Engineering and Physical Sciences (EPS)
Institute of Photonics and Quantum Sciences (IPaQS)
June 2018

Abstract

In the past decade, increasing demand and rapid developments in classical and quantum sciences resulted in advanced novel multipixel single photon detector arrays engineered on a single electronic chip. Silicon single photon avalanche detector (Si-SPAD) is one of the mainstream solution for low level light detection in visible and near-infrared wavelength region due to the dependable amplification of light signal. This thesis mainly focusses on three key experiments to showcase the potential applications of a single photon detector (Megaframe 32) consists of 32×32 square array Si-SPADs with picosecond timing circuits. With $\approx$ 50 ps timing resolution, each SPAD can perform time-correlated single photon counting independently. First, the concept of multiplexed single-mode wavelength-to-time mapping (WTM) of multimode light was investigated. The space-time imaging capability of the Megaframe was then demonstrated by imaging the spatial modes emerging from a few-mode fibre enabling WTM of spatial modes. Finally, time-resolved discrete imaging in laser inscribed photonic lattices was demonstrated. By placing a photonic lattice in a linear cavity and re-injecting the output mode profile back to the lattice, the propagation of light was measured in quasi-real time manner. The experimental demonstrations using Megaframe will find applications in Raman spectroscopy, soliton imaging, quantum optics, and discrete waveguide optics.

To my teachers.

Acknowledgements

First, I whole-heartedly thank my academic supervisor, Prof. Robert R. Thomson for his invaluable advice and guidance throughout my Ph.D. Thanks for the Christmas dinner, karting and hill walks.

I would like to thank my supervisor Dr. Helen L. Bridle for the guidance and suggestions during my Ph.D.

I would like to thank Dr. Frauke Izdebski for the suggestions and support during my Ph.D.

I am extremely grateful to my collaborators, Dr. Paul A Dalgarno, Dr. William McPherson, Dr. Tim A. Birks, Dr. Itandehui Gris-Sánchez, Dr. Nikola Krstajić, Dr. Richard Walker, and Dr. Robert K. Henderson for their involvement in the research.

I am grateful to Dr. Sebabrata Mukherjee for teaching me waveguide optics and his support during my Ph.D.

Great thanks to my fellow Photonic Instrumentation Group mates- Dr. Sebabrata Mukherjee, Dr. David MacLachlan, Dr. Debaditya Choudhury, Vikram Kamaljith, Calum Ross, Katjana Ehrlich, Dr. Michael G. Tanner, Gillian Madden, Helen Parker, and Dr. Alexander Arriola for their encouragement and help.

I sincerely thank Dr. Ximing Ren for his valuable suggestions and help during my Ph.D, especially in solving Matlab issues.

I thank Dr. Michael G. Tanner for training me with Megaframe camera during the initial stages of my Ph.D. My most humble thanks to Dr. Jonathan Morton for his help during my Ph.D.

I thank my teachers, Dr. C. Selvaraju, Dr. N. Seshabamini, Prof. P. Predeep, and Mr. K.G Biju for their support and guidance. I thank all my teachers for their endless support and care.

I am thankful to my friends - Nirosh, Vikram, Anusha, Shradha, Nitin, Rishad, Hannah, Rose Mary, Stanley, Lijo, Stephy, Izabella, Aga, Thomas and many more - for their friendship and making my journey enjoyable with movies, parties, trips and games.

I thank all my friends in India, Suresh Karlad, Jemsheer, Rejith, Sujith, Refeek, Vineesh, Sanoop, Navitha, Rejani, Earnesto, Ajith, Susanth, Moideen, Ajinas, Shahina, Vimal, Nandu, Nirmal, Hemanthkumar, Sanal Raj, Sumesh, Aneesh J, Shafeer KB, Deenadayalan, Goutham Kumar, and many more for their valuable friendship, help and care throughout my life.

Lastly, I wish to thank my parents, brother, sister-in-law, and little Anaya for their endless love, care, and support. Thanks for everything.

ACADEMIC REGISTRY
Research Thesis Submission

Name*:*	HARIKUMAR K CHANDRASEKHARAN		
School:	EPS/IPaQS		
Version: *(i.e. First, Resubmission, Final)*	Final	Degree Sought:	Ph.D in Physics

Declaration

In accordance with the appropriate regulations I hereby submit my thesis and I declare that:

1) the thesis embodies the results of my own work and has been composed by myself
2) where appropriate, I have made acknowledgement of the work of others and have made reference to work carried out in collaboration with other persons
3) the thesis is the correct version of the thesis for submission and is the same version as any electronic versions submitted*.
4) my thesis for the award referred to, deposited in the Heriot-Watt University Library, should be made available for loan or photocopying and be available via the Institutional Repository, subject to such conditions as the Librarian may require
5) I understand that as a student of the University I am required to abide by the Regulations of the University and to conform to its discipline.
6) I confirm that the thesis has been verified against plagiarism via an approved plagiarism detection application e.g. Turnitin.

* *Please note that it is the responsibility of the candidate to ensure that the correct version of the thesis is submitted.*

Signature of Candidate*:*		Date:	

Submission

Submitted By *(name in capitals):*	HARIKUMAR K CHANDRASEKHARAN
Signature of Individual Submitting:	
Date Submitted:	

For Completion in the Student Service Centre (SSC)

Received in the SSC by *(name in capitals):*			
Method of Submission *(Handed in to SSC; posted through internal/external mail):*			
*E-thesis Submitted (**mandatory for final theses)***			
Signature:		Date:	

Please note this form should be bound into the submitted thesis.

Contents

List of Figures

List of Abbreviations

TCSPC	**T**ime-Correlated **S**ingle **P**hoton **C**ounting
MF32	**M**egaframe 32
PMT	**P**hoto**M**ultiplier **T**ube
WTM	**W**avelength-to-**T**ime **M**apping
MCF	**M**ulti**C**ore **F**ibre
FWHM	**F**ull **W**idth **H**alf **M**aximum
NEP	**N**oise **E**quivalent **P**ower
SNR	**S**ignal-to-**N**oise **R**atio
APD	**A**valanche **P**hotodiode
SPAD	**S**ingle **P**hoton **A**valanche **D**iode
TAC	**T**ime-to-**A**mplitude **C**onverter
ADC	**A**nalog-to-**D**igital **C**onverter
TDC	**T**ime-to-**D**igital **C**onverter
IRF	**I**nstrument **R**esponse **F**unction
CFD	**C**onstant **F**raction **D**iscriminator
GRO	**G**ated **R**ing **O**scillator
MFD	**M**ode **F**ield **D**iameter
SMF	**S**ingle-**M**ode **F**ibre
FMF	**F**ew-**M**ode **F**ibre
EA	**E**ffective **A**rea
MMF	**M**ulti**M**ode **F**ibre
PCF	**P**hotonic **C**rystal **F**ibre
SC	**S**uper**C**ontinuum
PL	**P**hotonic **L**antern
NA	**N**umerical **A**perture
CCD	**C**harge **C**oupled **D**evice
FP	**F**abry-Pérot
BP	**B**and**P**ass
AOTF	**A**cousto **O**ptic **T**unable **F**ilter
GVD	**G**roup **V**elocity **D**ispersion
DMD	**D**ifferential **M**ode **D**elay
LP	**L**inearly **P**olarised
1D	**1 D**imensional
ULI	**U**ltrafast **L**aser **I**nscription
CMT	**C**oupled **M**ode **T**heory

List of Symbols

h	Plank's constant
K	Boltzmann's's constant
α	secondary electron emission coefficient
R	resistance
C	capacitance
β	propagation constant
λ	wavelength
ν	frequency
k	wave number
v	normalised frequency
τ	modal delay
n	refractive index
η_{eff}	effective refractive index
a	lattice constant
κ	coupling constant

List of Publications

1) **Harikumar K. Chandrasekharan**, Frauke Izdebski, Itandehui Gris-Sánchez, Nikola Krstajić, Richard Walker, Helen L. Bridle, Paul A. Dalgarno, William N. MacPherson, Robert K. Henderson, Tim A. Birks, and Robert R. Thomson, *Multiplexed single-mode wavelength-to-time mapping of multimode light,* Nature Communications **8**, 14080 (2017).

2) Sebabrata Mukherjee, **Harikumar K. Chandrasekharan**, Patrik Ohberg, Nathan Goldman, and Robert R. Thomson, *State-recycling and time-resolved imaging in topological photonic lattices,* arXiv:1712.08145 (2017).

3) **Harikumar K. Chandrasekharan**, Katjana Ehrlich, Michael G. Tanner, Tim A. Birks, and Robert R. Thomson, *Multiplexed wavelength-to-time mapping of spatial modes in a few-mode fibre* - "to be submitted"

Conference presentations

1). **Harikumar K. Chandrasekharan**, Frauke Izdebski, Itandehui Gris-Sánchez, Nikola Krstajić, Richard Walker, Helen L. Bridle, Paul A. Dalgarno, William N. MacPherson, Robert K. Henderson, Tim A. Birks, and Robert R. Thomson, *Multiplexed single-mode wavelength-to-time mapping of multimode light,* Photon16, IOP Conference, Leeds 5th-8th September (2016).

2). **Harikumar K. Chandrasekharan**, Frauke Izdebski, Itandehui Gris-Sánchez, Nikola Krstajić, Richard Walker, Helen L. Bridle, Paul A. Dalgarno, William N. MacPherson, Robert K. Henderson, Tim A. Birks, and Robert R. Thomson, *Multiplexed single-mode wavelength-to-time mapping of multimode light,* Photonics West, SPIE, San Francisco 28 Jan-2 February (2017).

Chapter 1

Introduction and background

1.1 Introduction

Based on Einstein's light quantum hypothesis, light is composed of individual packets of discrete energy, referred as photons. Generation, detection, and applications of single photons acted as the emerging technologies in modern physics. In the visible and near-infrared spectral region, these photons have an energy as low as 10^{-19} J. The limits in measuring certain quantities of single photons are outlined by Heisenberg uncertainty principle [1]. One of the major area of single photon research is in quantum information applications, where single photons are used to encode, manipulate, and securely sharing informations [2]. Quantum computing relies on the superposition of quantum states known as qubits and detecting these states with high accuracy. As a potential candidate in quantum computing, photons can be replaced with qubits in advanced quantum computing applications [3]. In optical quantum simulators, N indistinguishable single photon states are used for the quantum information processes [4].

The explosive growth of quantum information technology have driven into the development of single photon detectors for sensing and imaging applications. A single photon detector is an extremely sensitive device capable of registering light at single photon level in most of the photon-starved applications. For example, in time-of-flight laser ranging, the energy of reflected laser signal from the target is extremely low and efficient single photon detectors are used for image acquisition [5]. In biophotonics and medical applications, the emission rate of the samples upon excitation is very low and the emission occurs in short time scale. In order to detect these low level signals, efficient and reliable single photon detectors are essential [6].

Early stage single photon detectors were single pixel detectors such as Photomultiplier

Tubes (PMT) and Avalanche Photodiodes (APDs). The poor mechanical stability and relatively larger physical size are the major drawbacks of PMTs despite of their larger active area. Also, the timing response of PMTs are of the order of 1 ns due to the fluctuations in the electron transit time from cathode to anode [7]. This means that PMTs are not a good candidate for applications were higher detection efficiency and low timing jitter is required. On the other hand, APDs requires higher operating voltage and they produces higher noise levels which forbids their applications in photon-correlation measurements. These single pixel detectors are not the mainstream solution for imaging applications since they are not offering any spatial resolution. Scanning the object and recording the data at specific position is a solution but this may lead to position related error and longer data acquisition time.

Single Photon Avalanche Diodes (SPADs) replaced PMTs and APDs in many applications due to its enhanced detector characteristics. The benefits of SPADs includes compactness, high photon detection probability, low biasing voltage, and ease to modify design for specific application. The SPADs are usually operate in room temperature, but they may be cooled to reduce the noises in detection. SPADs are based on avalanche photodiode structure reverse biased above breakdown voltage (Geiger mode) [8]. Once the photon is absorbed, the generated electron-hole pair is multiplied by avalanche process generating more electron-hole pair. Today, SPADs are extensively used in many scientific fields where the photon intensity is extremely low. Some of the applications of SPADs involve physics [9], chemistry [10], biology [11], fluorescence spectroscopy [12], single molecule detection [13], astronomy [14], optical time-domain reflectometry [15], sensing [16].

Silicon based SPADs (Si-SPADs) have been long used as single photon detectors in visible and near infrared spectral region due to the self-sustaining avalanche process [17, 18]. Si-SPADs offer low dark counts, high detection efficiency and high count rate in the visible to near infrared range. Due to the bandgap of silicon, the wavelength region of Si-SPAD is limited to 400 nm to 1100 nm. As a consequence of the enhanced efficiency of Si-SPADs below 1 μm, they are extensively used as a detector in single photon counting applications. Even though Si-SPADs offers high detection efficiencies in the visible to near infrared spectral region, conventional SPAD fabrication technology is complicated and expensive [19]. Also, the process required to produce reach-through APD structure limits the cointegration of electronic circuits in large array SPAD fabrication.

Recent developments in single photon detector technology enables many single photon detectors fabricated on a single electronic board providing both the temporal and spatial informations for space-time imaging applications. The integration of larger arrays

of SPADs with the electronic circuits is possible with complimentary-metal-oxide semiconductor (CMOS) process [20]. The cointegration enables individual detectors with low dark noise and low timing jitter. The technology provides special class of multipixel sensors which can measure the arrival time of photons with high precision similar to single pixel detectors. In time-of-flight and time-correlated single photon counting (TCSPC) applications, each pixel in the array can perform individual measurements with dedicated electronic circuitry.

Progress in nanometer scale CMOS technology have driven to the integration of detectors and converter functions on single chip to create monolithic TCSPC system. The Megaframe 32 (MF32) is one of such single chip array consisting of a 32×32 square array of Si-SPADs capable of performing independent time-resolved measurements with picosecond timing resolution. Each pixel acts as an individual detector channel with dedicated timer electronics reducing the power consumption and complexity [21]. Each SPAD has a 10 bit time-to-digital converter (TDC) fabricated with a combined coarse-fine architecture spanning a dynamic range of $\approx$ 54 ns. The fast timing response and low power consumption of the SPADs in the Megaframe are achieved by the two ring oscillator design [21]. This permits the array to perform TCSPC measurements such as florescence life time imaging (FLIM) [22], multiplexed wavelength-to-time mapping [23], and light-in-flight imaging [24]. Alternatively, the device can perform photon counting, where the pixels measures the number of photon events within a predefined exposure time.

1.2 Aim

The works presented in this thesis investigates the potential applications of the Megaframe in a variety time-resolved photonic applications. To show case the time-resolved imaging capability of the Megaframe, this thesis presents three experimental demonstrations- multiplexed single-mode wavelength-to-time mapping (WTM) of multimode states of light, real-time imaging and WTM of spatial modes in a few-mode fibre, and time-resolved discrete imaging in laser written optical waveguides.

Recent demonstrations in real-time Raman spectroscopy have exploited single-mode fibres (SMFs) and single photon detector in combination with TCSPC to acquire Raman spectra. The concept is based on WTM, a process occurs when a light pulse propagates in a dispersive medium. This demonstration of WTM for spectroscopy is restricted to the use of one single photon detector and SMF which drastically affects the signal acquisition rate [25]. The low light collection efficiency of SMF and increased tolerances

to misalignment is another key issue in the already demonstrated WTM system for spectroscopic application. To address these issues, the first experimental demonstration of multiplexed single-mode WTM of multimode states of light was performed using a multicore fibre-photonic lantern (MCF-PL) and the Megaframe. The efficient collection of light to the fibre is achieved at the multimode end of the lantern, at the same time enabling the transmission and processing benefits of SMFs by distributing the multimode states of light into the single-mode cores in a scalable manner. The temporal and spatial resolution for the WTM system can be provided by Megaframe by coupling the single-mode cores onto individual pixels. The pixels in the Megaframe can be used as individual detector channels for enhanced signal-to-noise ratio.

To investigate how the WTM system can be used in a multimode environment, multiplexed WTM of spatial modes was performed in a few-mode fibre (FMF). A quasi real-time imaging and WTM of propagating modes in a FMF was demonstrated for the first time using the TCSPC capability of the Megaframe. The conventional multimode fibre characterisation techniques such as interferometry and phase shift techniques are time consuming and requires complicated calibration of the propagating modes. The spatial mode WTM system offers mode parameter measurement resolution comparable to other existing characterisation techniques and does not require any complicated calibration. This spatial mode imaging technique will find applications in time-stretch spectroscopy offering more degrees of freedom by utilising higher order modes.

Lastly, the evolution of light in coupled optical waveguide lattices is studied using the Megaframe. In the current coupled optical waveguide lattices, the propagation loss of light in the waveguides limits the observation of discrete light phenomena over long lattice length. One way to overcome the loss is to use single photon sensitive detectors to detect light even at the single photon level. Using state-recycling technique, discretised propagation of light in 1-dimensional photonic lattices were demonstrated with the Megaframe. By imaging waveguide modes onto individual SPADs in the Megaframe, the propagation of light in the lattices were monitored in real-time. So far, the discrete imaging in waveguide systems is restricted with the use of charge coupled device (CCD) cameras which can only provide the spatial distribution of light in waveguide modes. Exploring the TCSPC capability of the Megaframe, the hopping of light in 1-dimensional (1D) lattices were demonstrated for the first time which cannot be possible with any other existing imaging techniques.

1.3 Impact in scientific community

The research presented in this thesis would have great impact on broad scientific community. The beneficiaries of the presented research includes life science researchers, optical scientists, and users of laser ranging systems. In life science, the demonstration using Megaframe would allow the user to acquire low intensity level fluorescence signals with fast time sampling capability. The most demanding medical applications such as FLIM, confocal microscopy, and biological analysis requires single photon sensitivity and large number of pixels. The conventional imaging systems such as CCD cameras and electron multiplying EMCCDs suffers slow readout and slow time response. With well calibrated Megaframe pixels inconjunction with the multiplexing capability of MCF-PL, the signals from biological samples can be recorded with high frame rates. The technique could be integrated in Mars/Moon rovers for designing a real-time light weight Raman spectrometer for acquiring Raman signal with high mechanical stability.

The time-resolved imaging capability of Megaframe would benefit scientists in monitoring ultrafast phenomena in wide range of applications. For example, time-resolved imaging of tissues deep inside human body can be performed with increased accuracy, fast sampling rate, and with increased contrast. In soliton physics, the Megaframe can be used to study the evolution of solitons for long time scale.

In laser ranging applications, the technique facilitate improved multimode signal collection efficiency along with excellent mode matching for heterodyne mixing. Similarly, in discrete optics, the scientists could benefit from the time-gated imaging capability of Megaframe in observing discrete phenomena. The long time scale photonic phenomena such as Bloch oscillations [26, 27] , Anderson localisation [28], and Talbot's effects [29] can be easily explained with individual detector channels of Megaframe which is impossible with conventional imaging systems. The research will open a new route towards the realisation of hybrid analogue-digital simulators.

Overview of the Thesis: This thesis discusses different experimental works performed to showcase the potential applications of the Megaframe. Theoretical backgrounds of single photon detectors and waveguide optics is given. Three experiments were performed and discussed with theoretical interpretation in this thesis.

Chapter 2: *Single photon detectors and their applications*: This Chapter reviews common single photon detectors and their applications, TCSPC technique, and the Megaframe 32 detector.

Chapter 3: *Guided wave optics - background*: This Chapter reviews guided wave optics. A literature review on fibre optics is given. Photonic lanterns and light propagation through a photonic lantern are explained briefly.

Chapter 4: *Multiplexed Single-mode wavelength-to-time mapping of multimode light*: Characterisation of a MCF-PL and the demonstration of multiplexed WTM using MCF-PL and the MF32 is given. The efficient coupling and reformatting of multimode states of light from the MCF-PL onto a subset of pixels at the Megaframe is discussed.

Chapter 5: *Quasi real-time imaging and wavelength-to-time mapping of spatial modes in a few-mode fibre*: Quasi real-time imaging and WTM of spatial modes in a FMF using the Megaframe will be explained in this Chapter. The relative modal delay, chromatic dispersion and effective group refractive index measurements of propagating modes will be given with relevant theory.

Chapter 6: *Time-resolved discrete imaging in photonic lattices using state-recycling*: In this Chapter, quasi real-time evolution of light in periodic photonic lattices using state-recycling technique will be explained with theoretical justifications.

Chapter 7: *Conclusions*: The summary of all experiments reported in this thesis is given in this Chapter. The future possibilities using the demonstrated experiments are also given.

Chapter 2

Single photon detectors and their applications

2.1 Introduction

Single photon detectors are a crucial element in classical and quantum sciences which can convert low level photon signal into some sort of measurable electrical signal. This review Chapter attempts to introduce some of the early stage single photon detectors and their applications along with a novel multipixel single photon detector for time-resolved imaging applications. Though there are detectors which are designed to resolve photon numbers in an optical signal, this Chapter only reviewing non-photon number resolving single photon detectors. The Chapter describes single photon detector technologies such as PMT, microchannel plate PMT (MCP-PMT), APD, and SPAD. A review on TCSPC technique and applications of TCSPC are also included in the Chapter. This Chapter also introduces a multipixel single photon detector, Megaframe 32, to the reader with its key characteristics and applications.

2.2 Single photon detectors

This Section describes the working principles and applications of commonly used single photon photoelectronic detectors such as PMT, MCP-PMT, APD, and SPAD.

The key parameters which describes the performance of single photon detectors are,

Timing jitter: Timing jitter represents the variation in the time interval between the absorption of a photon and the generation of an output electrical signal from the detector. A low timing jitter indicates better timing accuracy for photon counting applications.

Dead time: The time during which the detector unable to register photons after the detection of a photon. This is usually the reset time for a single photon detector.

Spectral range: The wavelength range over which the detector can operate.

Dark count: Number of false events registered by the detector. The common source of dark counts in single photon detectors is the thermal noise.

Detection efficiency: The ratio of number of photons detected to the input photons.

Photon number resolution: The ability of the detector to resolve multiple incident photons.

Noise equivalent power: The most widely accepted quantity in characterising a single photon detector is the noise equivalent power (NEP). The NEP can be expressed as [31],

$$NEP = \frac{hc}{\lambda\eta}\sqrt{2D} \tag{2.1}$$

where, h is the plank's constant, λ is the wavelength of incident photon, η is the detection efficiency and D is the dark count rate.

2.2.1 Photomultiplier tubes

PMT is a photoelectronic detector which can convert low intensity light signals into a measurable electric current, combining photoelectric effect and secondary electron emission. The PMT was the first device to demonstrate single photon counting capabilities [32]. A PMT is a non-thermionic vacuum tube consisting of an input window, focussing electrodes, dynodes and anode. The secondary electron multipliers used in PMTs are classified into two types: the normal discrete dynodes consisting of multiple stages and continuous dynodes such as microchannel plates [33]. In a PMT, photons pass through a window and impact on an electrode consisting of a photoelectric material known as the photocathode [34]. The photocathode absorbs energies at specific photon frequencies and emits electrons as a result. The dynodes emits secondary electrons when electrons from cathode are incident on them. The arrangement of dynodes are made in such a way that the electric field between them results the electrons produced by one dynode strikes the next one causing the multiplication of secondary electrons after many stages. A schematic diagram of a PMT is given in Fig. 2.1.

Light at shorter wavelength region passes through the input window is focussed onto the photocathode. The input window, usually made of glass limits the spectral sensitivity of the incident light. The light excites the electrons in the photocathode and photoelectrons

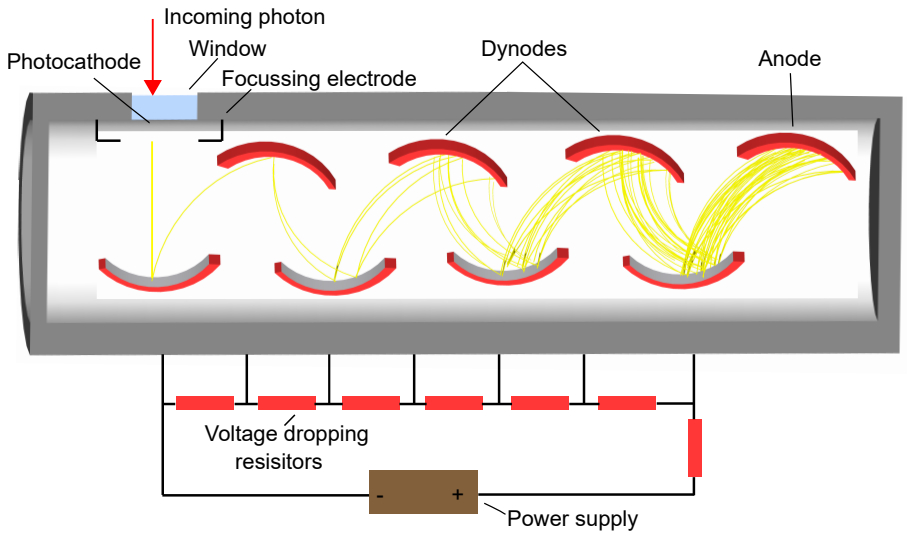

Figure 2.1: Schematic diagram of a photomultiplier tube.

are emitted into the vacuum. The emitted photoelectrons from the photocathode are focussed onto the first dynode using the focussing electrodes where they are multiplied by means of secondary electron emission. This process is repeated by each of the successive dynode and a large number of photoelectrons is collected at the anode. To accelerate the secondary electrons from the dynodes, a higher supply voltage must be provided to each successive dynodes. The voltage drop for each dynode is provided by a voltage-divider circuit [35]. The timing jitter of PMTs and other single photon detectors are expressed as the full-width half-maximum (FWHM) of the instrument response function. The typical timing jitter of a PMT in visible and near infra-red regions is $\approx$ 300 ps FWHM [36]. This time response is determined by the time required for the photoelectrons to travel from cathode to the anode after being multiplied and the the transit time difference between each of the photo-electron. For a PMT with N dynodes, each with secondary electron coefficient α, the multiplication factor M_{pmt} is given by,

$$M_{pmt} = \alpha^N \tag{2.2}$$

For a PMT with 10 dynodes and α = 4, the M_{pmt} is 10^6. Usually, PMTs have gain which lies in the range 10^4 and 10^7 [37].

Microchannel plate photomultiplier tubes (MCP-PMT) offer wide-band width range measurements down to the picosecond timing levels as well as low-light-level detection at the photon counting level. Figure 2.2, illustrates the structure and principle of a microchannel plate. A microchannel plate is a two dimensional array of glass capillaries with an

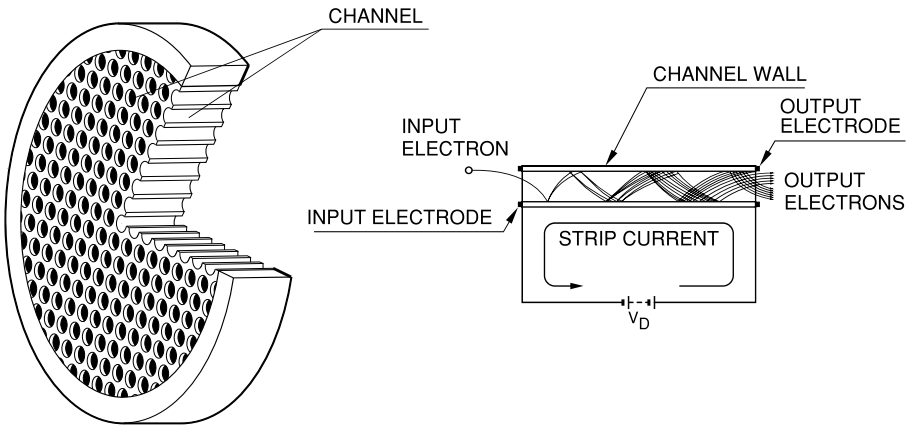

Figure 2.2: Schematic diagram of a microchannel plate. This figure is adapted from [35].

internal diameter of around 10-20 μm stacked into a thin disk. Each microchannel wall is secondary electron emissive and the wall ends are covered with a thin metal film that acts as an electrode. By applying a voltage across the capillary, an electric field is created in the direction of the channel axis. After a wall-electron collision, secondary electrons are accelerated by this field in the direction of the electric field. Due to the repeated secondary electron emission along the capillary, a large number of electrons are produced and collected at the end of the microchannel. As the result of this continuous multiplication process, the transit time for the photo-electrons is short and hence MCP-PMTs offers better timing jitters, down to $\approx$ 20 ps compared to basic PMTs [38].

The ability of PMTs to detect light at the single photon level makes them an efficient detector in TCSPC experiments [39]. Today, PMTs are extensively used as photodetectors in spectroscopy [12], medical diagnosis [40], environmental applications [41], fluorescence life time imaging (FLIM) [39], flow cytometry [42].

2.2.2 Avalanche photodiode

APD is a semiconductor based photodetector, which is operated with a high reverse voltage. The diode is formed by a junction of a p-type semiconductor and an n-type semiconductor. The semiconductor materials include silicon (Si), germanium (Ge) and compound semiconductors. A p-type semiconductor is formed by doping Si with a trivalent impurity such as boron. Since boron has only three valance electrons and Si has four valance electrons it would lead to a p-type semiconductor where holes are the majority charge carriers. An n-type semiconductor can be formed by doping Si with donor impurities such

as phosphor. The doping would lead to electrons as the majority charge carriers since phosphor has five valance electrons.

Semiconductors can be explained in terms of an energy band diagram [43, 44]. In semiconductors, the energy band diagram will show the electron energy levels such as the valance band (E_V) and the conduction band (E_C). The difference between the minimum conduction band energy (E_C) and the maximum valance band energy (E_V) is known as the bandgap energy (E_g). The Fermi level (E_F) lies within the energy bandgap of the semiconductor in which the position is determined by the carrier concentration. In an intrinsic semiconductor for temperature above 0 K, E_F is located approximately in the middle of the band gap energy as the concentration of the electrons in the conduction band is equal to the concentration of holes in the valance band as shown in Fig. 2.3 (a). At higher temperatures, the conduction band fills up as the electron-hole pair generates through thermal excitations. The rate of electron-hole pair formation is equal to the rate of electron-hole recombination in intrinsic semiconductors.

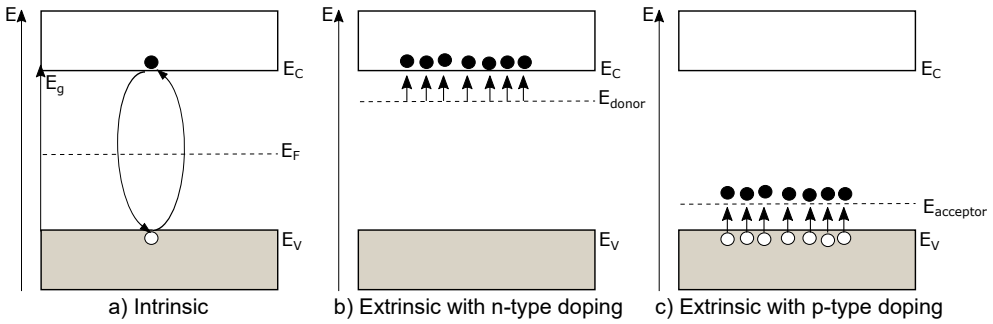

Figure 2.3: Energy band diagram of intrinsic and extrinsic semiconductors above 0 K: a) intrinsic semiconductrs without any impurities b) n-type semiconductor. At higher temperature, the conduction band fills with electrons and the Fermi level lies close to the conduction band. c) p-type semiconductor. At higher temperature, electrons from the valance band are promoted to the acceptor level leaving holes behind. The Fermi level lies closer to the valance band.

The Fermi level of extrinsic semiconductors lies close to the donor or acceptor energy level. For an n-type semiconductor above 0 K, the Fermi energy lies close to donor energy level as the concentration of electrons in the conduction band is higher than the concentration of holes in the valance band as shown in Fig. 2.3 (b). Similarly, for a p-type semiconductor at higher temperatures, the acceptor level fills up with electrons leaving holes behind. The Fermi energy lies close to the acceptor level due to the higher concentration of holes in the valance band, as shown in Fig. 2.3 (c).

When a p-n junction is formed, electrons diffuse from n-doped region into the p-type region where they combine with holes, and vice versa. The result is a depletion region that is depleted of majority carriers. When applying a voltage to the p-n junction, electrons and holes moves from one side to another depending on the biasing conditions. In forward bias, the positive terminal of the voltage source is connected to the p-type material and negative terminal is connected to the n- type material so that holes are injected into the p-type material and electrons into the n-type material.

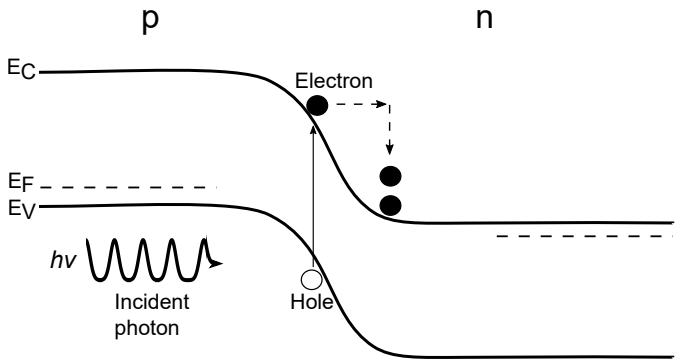

Figure 2.4: Energy band diagram of a p-n junction in reverse biased condition. When a photon gets absorbed in the depletion region, an electron is promoted from the valance band (E_V) to the conduction band (E_C), leaving a hole behind. A high internal electric field will generate in the depletion region which accelerates the electron.

However, when the diode is reverse biased, n-type is at higher potential than the p-type. At the barrier of the p-type and n-type semiconductor layers, more electrons and holes diffuse and recombine. The concentration of the majority carriers increases and the depletion area widens with a high internal electric field in the region. The strength of the depletion region electric field increases as the applied external reverse-bias voltage increases. When a photon is absorbed in the depletion region an electron-hole pair will be formed and become separated by the internal electric field [43]. Fig. 2.4 shows the energy band diagram of p-n junction in reverse biased condition.

If the external electric field is high enough, the drifting electrons gain kinetic energy and excite more electrons in the semiconductor lattice by colliding with the atoms in the lattice. In this case, the secondary electrons also excite more electrons and the internal current increases due to the impact ionization effect starting an avalanche of electrons (see Fig. 2.4). APDs have an internal region where electron multiplication occurs, by applying a high external reverse voltage, and the resulting gain at the output signal means that low light levels can be measured at high speed.

The basic APD design consists of a p-i-n structure given in Fig. 2.5. The diode consists of a thin region where the electric field is high and a low field substrate region. The diode is reverse biased under high voltage. A depletion region is formed between the highly doped n^+ and p region. Since n^+ region is heavily doped, the electric field is high in the depletion region. The spectral sensitivity of the APD depends on the side where the photon gets absorbed. If the photon strikes at the n^+ region, then the APD is sensitive from 450 nm to 1000 nm. If the photon strikes at the p^+ region, then the APD is sensitive from 200 nm to 800 nm [45].

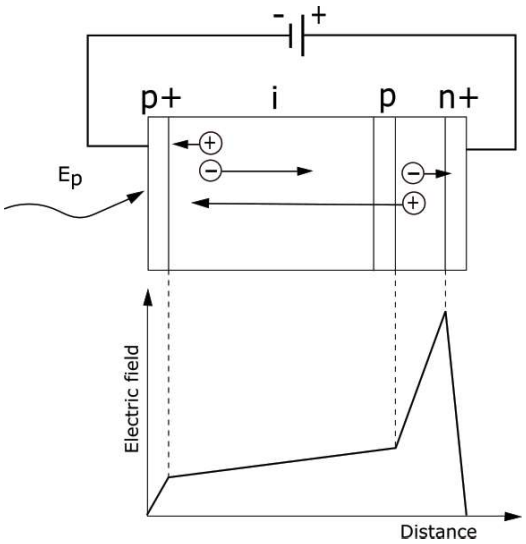

Figure 2.5: Schematic diagram of reach-through structure of an APD in reverse biased. n^+-heavily doped n region, p^+-heavily doped p region, p-lightly doped p region, and i- intrinsic region. The bottom Figure presents the electric field profile. This figure is adapted from [45].

Multiplication gain

When the applied electric field increases, the carriers gain the required kinetic energy to begin the impact ionisation. If α_e is the impact ionisation rate for electrons and β_h is the impact ionisation rate for the holes, the expression for impact ionisation rate vs electric field E is given by [46],

$$\alpha_e(E) = a_e e^{(-b_e/E)^{ce}} \tag{2.3}$$

$$\beta_h(E) = a_h e^{(-b_h/E)^{c_h}} \tag{2.4}$$

where a_e, b_e, c_e, a_h, b_h, and c_h are constants. The parameter which determines the bandwidth and noise in then material is the k-ratio, which is the ratio between the hole and the electron ionisation rates. the k-ratio is given by,

$$\mathrm{k} = \frac{\beta_h}{\alpha_e} \tag{2.5}$$

For an electron multiplication material, the k-ratio must be small and for a hole multiplication material, the ratio must be as larger as possible for low noise.

The gain can be expressed as the ratio of multiplied total current to the initial injected current. The multiplication gain M is classified according to the carrier which initiates the ionisation. For the case were the hole induces multiplication and $\alpha_e \neq \beta_h$, then gain M can be expressed as [46],

$$\mathrm{M} = \frac{1}{1 - \left[\int_0^w \alpha_e(E) \exp\Big\{ - \int_0^x [\alpha_e(E) - \beta_h(E)] dx' \Big\} dx \right]} \tag{2.6}$$

where w is the width of the multiplication region. The expression for electron multiplication gain can be obtained by interchanging α_e and β_h in Equation 2.6.

Noise and signal-to-noise ratio

The performance of any single photon detector is highly depends on the noise in the detector. These noise sources are classified into three: photon shot noise, detector dark noise, and amplifier noise.

Shot noise is inherent to the signal and arises due to the discreteness of photons in a signal. The shot noise can be expressed as [47],

$$\mathrm{i_{shot\ noise}} = \sqrt{2\mathrm{q}\mathrm{I_{ph}}\mathrm{M}^2\mathrm{F}\Delta\mathrm{B}} \tag{2.7}$$

where q is the electron charge, $\mathrm{I_{ph}}$ is the photogenerated signal current, M is the detector gain, F is the detector excess noise factor, and ΔB is the electrical bandwidth of the detector.

The detector dark current in an APD is not related to photon signal. It arises from two sources, the noise due to detector dark current and the excess noise from the internal amplification mechanism of the detector.

The expression for noise current due to detector dark current can be obtained by replacing I_{ph} with I_D in Equation 2.7. However, the noise source in an APD entirely depends upon the operation mode of the diode. The expression for shot noise for the diode in photoconductive mode can be obtained by replacing I_{ph} with I_{Dark} and setting F, M to 1 in Eq. 2.7. In this mode, the shot noise of the dark current is relatively large and dominates the noise of the diode.

In photovoltaic mode, the dark current is negligible. The expression for Johnson noise which arise from thermal fluctuations is given by [47],

$$i_j = \sqrt{\frac{4KT\Delta B}{R_{sh}}} \tag{2.8}$$

where K is the Boltzmann's constant, T is the absolute temperature of the photodiode, and R_{sh} is the shunt resistance of the photodiode. The Johnson noise measurement of different detector systems can be used to calculate the Boltzmann's constant with high accuracy [48].

There are two other sources of noise in APDs, noises from afterpulse and crosstalk. Afterpulses happens when the trapped carriers from the primary avalanche in the pixel releases and induces a secondary avalanche after a certain time compared to the primary avalanche. Crosstalk occurs when the emitted photons from the primary avalanche in one pixel triggers an avalanche in the neighbouring pixel.

The detector amplifier noise entirely depends on the amplifier combinations of the system. The amplifier feedback resistor is the predominant source of noise in the amplifier system. The load resistor should be small compared to the shunt resistor of the photodiode to minimise the noise. The second source of noise in the amplifier circuit depends on the terminal capacitance of the detector. The detector capacitance should be small to minimise this noise. The third component is the shot noise from the amplifier input bias current (I_b).

The total noise from the amplifier circuit is given by [47],

$$i_{tot} = \sqrt{I_{shot}^2 + I_{Rsh}^2 + I_b^2 + I_f^2 + I_v^2} \tag{2.9}$$

where I_{shot} = signal induced shot noise + detector dark noise, I_f and I_v are the amplifier resistor noise current and voltage noise current respectively.

The amplifier noise and the photodetector dark noise contributes the total noise of the detector system. The photon shot noise varies with different input signal level. The signal-to-noise ratio (SNR) of the detector system can be written as [47],

$$\mathrm{SNR} = \frac{I_{ph}M}{i_{tot}} \tag{2.10}$$

A low SNR in the photodetector is the limiting factor in most of the photonic applications. Therefore its crucial to select the detector specifications with low noise levels and high SNR.

Geiger mode

The current gain in an APD can be enhanced by operating the APD in the linear mode (Region III in Fig. 2.6). The internal current gain is determined by the bias voltage. If the bias voltage is set above the breakdown voltage then a self-sustaining avalanche current will be created. The difference between the applied bias and the breakdown voltage is known as overbias or excess bias. The probability that a carrier or an electron-hole pair initiates a current pulse is strongly depend on this parameter.

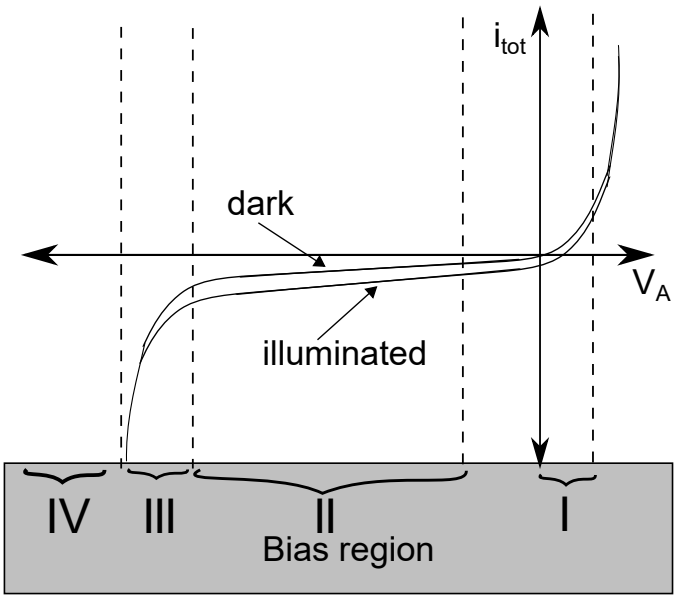

Figure 2.6: Current-voltage characteristic of a photodiode.

When biased above the breakdown voltage (Region IV in Fig. 2.6), APDs are capable of detecting light at single photon level. The operating mode is called Geiger mode. When a single photon is absorbed at the depletion region, a free charge carrier is generated which triggers an avalanche current. The generated carrier initiates further impact ionisation events and the current proportional to the excess bias voltage. A diode is in Geiger mode when it meets the condition [49],

$$1 \leq \int_0^w \alpha_e(E) \exp\Big(\int_x^w [\beta_h(E) - \alpha_e(E)] dx' \Big) dx \tag{2.11}$$

The biasing voltage at which the Equation 2.11 is an equality is termed as the biasing voltage.

The diode remains in the avalanche multiplication state which will only stops when the bias voltage drops. This is usually enhanced using a circuit known as quenching circuit. The Geiger mode is characterised by avalanche initiation probability [50], the probability that the avalanche become self-sustaining. The current formed by an avalanche in the Geiger mode has a fast rise time ($\approx$ 1 ns).

Quenching circuits

The self sustaining avalanche current must be quenched in order to prevent overheating and therefore the self destruction of the device before the next avalanche process. The design and selection of a quenching circuit is important since it effects the dead time of the SPAD. There are three types of quenching circuits applied to detectors: passive quenching, active quenching and gated quenching circuits. The simplest passive quenching circuit is a high impedance load connected in series with the APD as given in Fig. 2.7.

When a photon is absorbed in the active volume of the APD, the external current builds up by the consecutive multiplication process. The voltage drop across the load resistor (R_L) builds up so that the bias voltage on the APD reduces below the breakdown voltage. During the avalanche, most of the external bias voltage drops across (R_I). In a few nanoseconds, the external current becomes negligible and the device is again biased over the breakdown voltage waiting for the arrival of new photons. The maximum count rate of the device depends on the recharge time of the diode ($t = RC$), where C is the capacitance of the diode [43]. Passive quenching circuits have a slow recovery time compared to active quenching. For a Si-detector of active area 1 mm^2, the typical value for the series resistor is 2.5 MΩ and the typical diode capacitance is 1 pF. The reason for this high load

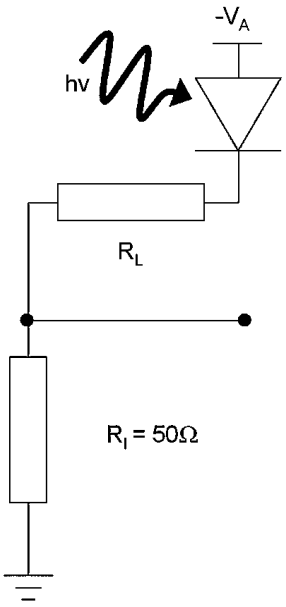

Figure 2.7: Simplest passive quenching circuit. This figure is adapted from [9].

impedance is that, the asymptotic current should be lower than the quenching current. This leads to a recharge time of 2.5 μs [8].

An alternative to passive quenching is active quenching [43]. Figure 2.8 is an example of active quenching circuit. Active quenching can be implemented by forcing the avalanche quenching using an external circuit that suddenly reduces the APD bias when a current pulse is detected. The diode is biased from a low load resistor (100Ω). The amplitude of the quenching pulse must be equal to or higher than the overbias. When a photon event induces an avalanche, it triggers a fast comparator in the circuit and switches the current in a transistor pair. A negative pulse is generated an superimposed with the bias current which quenches the avalanche. The external circuit can be a pulse-booster circuit or a combination of electronic switches and external DC power supplies. The purpose of this mode is to avoid the slow recovery from the avalanche pulses in the passive mode. Sufficient time must be given to the carriers to leave from the high electric field region and the bias voltage must be restored above the breakdown voltage value. If the carriers are trapped in the detector after an avalanche, they will initiate further avalanches once they are released and lead to the afterpulsing effect, which will distort the signal. However, active quenching is more complicated than the passive quenching since it requires more components in the quenching circuit.

In gated mode quenching the bias voltage is increased above breakdown voltage for a certain time. This time is the expected time for the photon event. However, this quenching

mode is only recommended when the distance from the target is known for the gating.

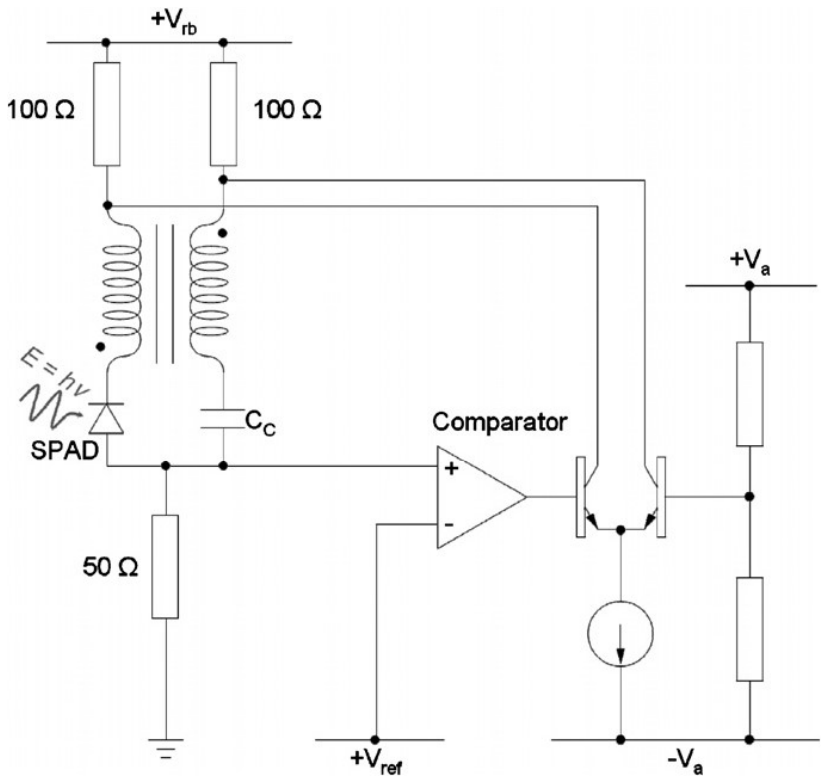

Figure 2.8: An example of active quenching circuit. This figure is adapted from [18].

2.2.3 Single photon avalanche diode

The APD that works in Geiger mode is called SPAD. When a single carrier is optically excited in the depletion region, a self sustaining avalanche current will develop in the depletion region. Figure 2.9 presents the structure of a SPAD with photo-absorption and multiplication region. The initial absorption of a photon generates an electron-hole pair at the photo-absorption region. The multiplication of carriers continuous as the applied reverse voltage sweeps the electrons to the multiplication region of the SPAD. Thus the avalanche proceeds after the carriers generated by the absorption of an incoming photon until the quenching current is applied. Following an avalanche, a SPAD is unable to detect further photons for a short period of time known as the dead time.

Si-SPADs have been used for a variety of applications in the 400 nm to 1100 nm spectral region for the past several decades [17, 18]. Depending on the volume of the depletion region, Si-SPAD detectors can be divided into two categories, thick junction SPADs, with depletion layer thickness of few tens of μm or thin junction SPADs with a depletion

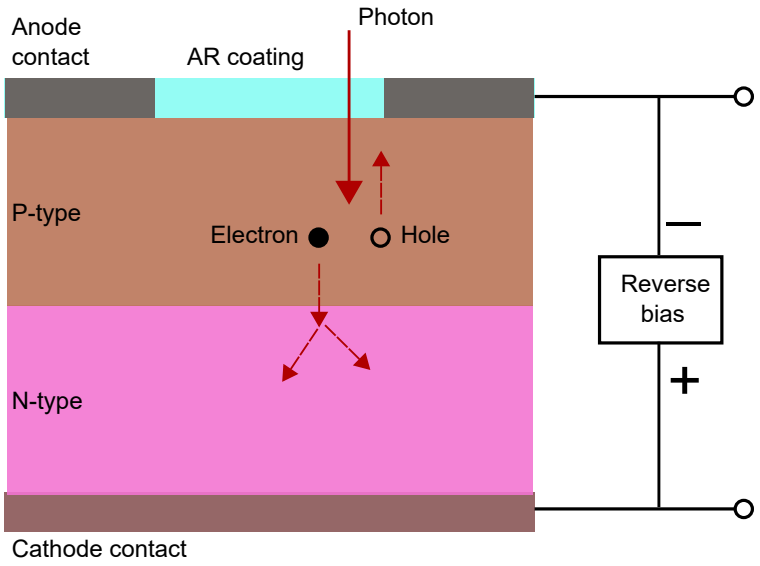

Figure 2.9: SPAD with photo-absorption and electron multiplication regions. The illumination side is coated with anti-reflection (AR) material for maximum photon absorption efficiency. A reverse voltage is applied to accelerate electrons to the multiplication region.

layer thickness of typically a few μm [51, 52]. The thick-junction silicon SPADs have a breakdown voltage (V_B) of 200–500 V with fairly wide active area, and diameters ranging from 100 μm to 200 μm. The quantum efficiency of thick-junction SPAD is very high in

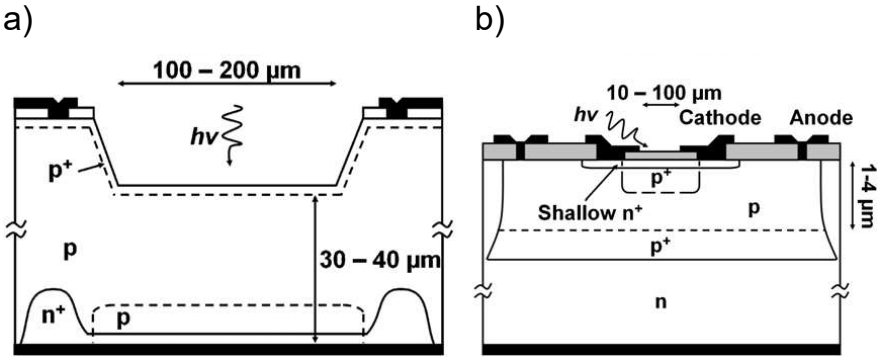

Figure 2.10: Comparison of thick (a), and thin (b) junction Si-SPAD designs. This figure is adapted from [9].

the visible region, above 50 % over all the range from 540 nm to 850 nm wavelength [8]. The highest peak efficiency of about 65 % at 650 nm is achieved using a 180 μm diameter thick high purity silicon absorber combined with an active quenching circuit and a cooling circuit [53]. Thin-junction SPADs have typical breakdown voltage (V_B) of 20–50 V with a small active area diameter ranging from 10 μm to 50 μm. The quantum efficiency of

thin-junction SPADs in the visible range is about 45 % at 500 nm and decreases to 32% at 630 nm and to 15 % at 730 nm and about 0.1 % at 1064 nm [8].

A comparison of thick and thin junction Si-SPAD designs is given in Fig. 2.10. The active area of the thick junction SPAD is heavily doped which is denoted as p^+. Once the photgenerated carrier is depleted in the p layer, diffusion of the carriers takes place in the surface p^+ layer. The lightly doped p layer acts as the guard ring which avoids edge breakdown. When the avalanche current is generated, the buried p^+ layer provides a low resistivity path to the current [52].

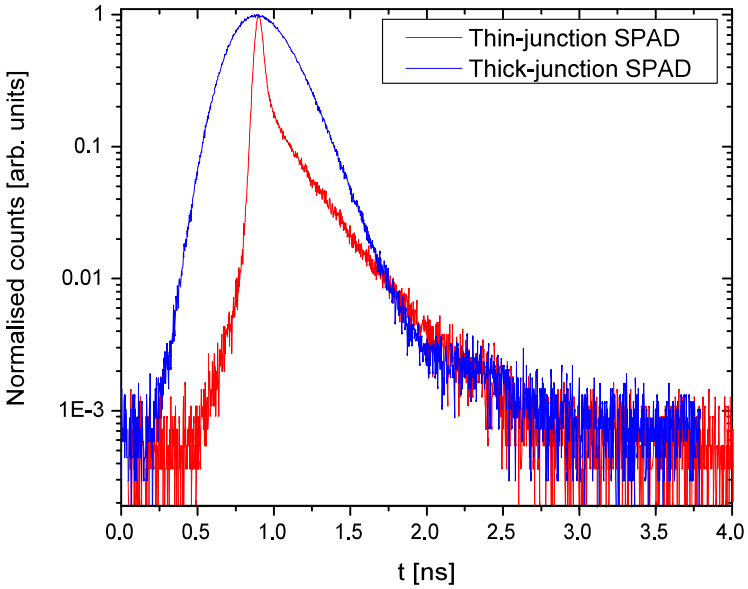

Figure 2.11: The timing jitter measured for thick-junction Perkin Elmer Si-SPAD and thin-junction MPD Si-SPAD. The thick-junction SPAD has higher timing jitter than thin-junction SPAD. The timing jitter of thick and thin-junction SPADs are 320 ps and 70 ps FWHM respectively. This figure is adapted from [44].

Like all other single photon detectors, SPADs can be characterised in terms of timing response. The time response of the SPADs can be measured using TCSPC technique (see Section 2.3). Figure 2.11 shows a comparison of timing jitter for a Perkin Elmer thick-junction Si-SPAD and a Micro-Photon-Device (MPD) thin-junction Si-SPAD measured at λ = 850 nm using TCSPC. The timing resolution is usually quoted with the FWHM of the curve. However, timing jitter obtained from TCSPC technique consists of jitter contributions from the laser source, SPAD, and the timing electronics [64].

The ability of SPADs to produce measurable external current in photon-starving conditions has positively contributed to numerous fields such as basic quantum cryptography [65], astronomy [14], single molecule detection [13], fluorescence spectroscopy [66],

Detector	Timing jitter (ps)	Detection efficiency	Dark count rate	Operation Temperature (K)
Si-SPAD (shallow junction) [54]	35	49% @550nm	25 Hz	250
Si-SPAD (thick junction) [55]	400	65% @650nm	25 Hz	250
InGaAs-SPAD (gated) [56]	370	10% @1550nm	91 Hz	200
InGaAs-SPAD (self diff-erencing) [57]	55	10% @1550nm	16 KHz	240
PMT (Visible-NIR) [58]	300	40% @500nm	100 Hz	300
PMT (infrared) [59]	300	2% @1550nm	200 Kz	200
NbN nanowire [60]	60	0.7% @1557nm	<10 Hz	3
ID281 nanowire [61]	50	80% @400-2500nm	<100 Hz	0.8
Hybrid photodetector [62]	95	25% @600nm	1 KHz	300
Tungston transition edge sensor [63]	90 000	88% @1550nm	10 Hz	0.1

Table 2.1: Comparison of single photon detectors and their relative merits.

sensor applications [16], photon correlation technique [71], 3D imaging [49].

The selection of single photon detectors for applications depends on the detector operating parameters and possible outcome. The wavelength of operation and the light power are important factors in detector selection. For example, in photon correlation measurements, the detectors with high efficiency and fast timing response are the desired parameters. Table 2.1 lists some of the single photon detectors with their performance characteristics taken from open literatures. It is crucial to understand these parameters when selecting detectors for the given application.

2.3 Time-correlated single photon counting technique

TCSPC [67] is a digital technique that counts photons that are time correlated with a pulsed light source. As shown in Fig. 2.12, the basic TCSPC set up consists of a master clock, pulsed light source, photon counting card, and the single photon detector.

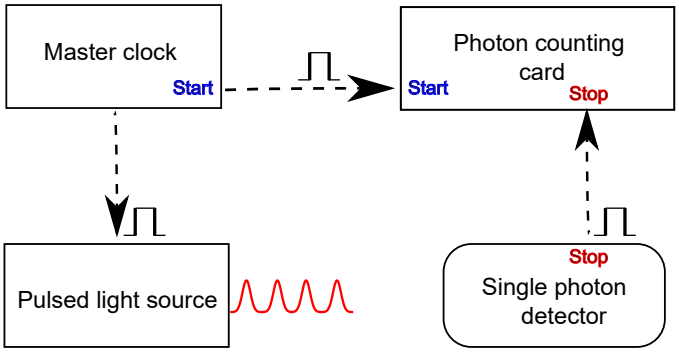

Figure 2.12: Basic experimental set up for TCSPC.

The counting process starts when the master clock sends an electrical signal to both the pulsed light source and the photon counting card. The detector sends the stop pulse to the photon counting card when a photon from the pulsed light source or a dark event is detected.

This process is repeated for many signal periods and the original optical waveform will be reconstructed by adding the individual signals from all measurements. The arrival time of each event within the signal period will be recorded and added in a memory location with an address proportional to the detection time of photons. This process is repeated for many signal periods and the original optical waveform of the pulse will build up in the memory from the distribution of the photon arrival times. The general principle of TCSPC is given in Fig. 2.13.

If the number of photons in the optical pulse is more than one, the system will only register the first photon in the histogram. The probability of detecting photons is therefore greatly reduced if more than one photon is present in a single signal period. The histogram will show an over-representation of early photons which results in the distortion of the optical signal. This effect is known as photon pile up. The intensity of the pulsed light source must be very low in order to avoid pulse pile-up and hence the distortion of the signal. Generally, one of the timing pulses (either START or STOP pulse) to the timing electronics will be a single photon.

Figure 2.14 represents a classic TCSPC setup. The TCSPC electronics for signal processing consists of constant fraction discriminator (CFD), Time-to-Amplitude converter

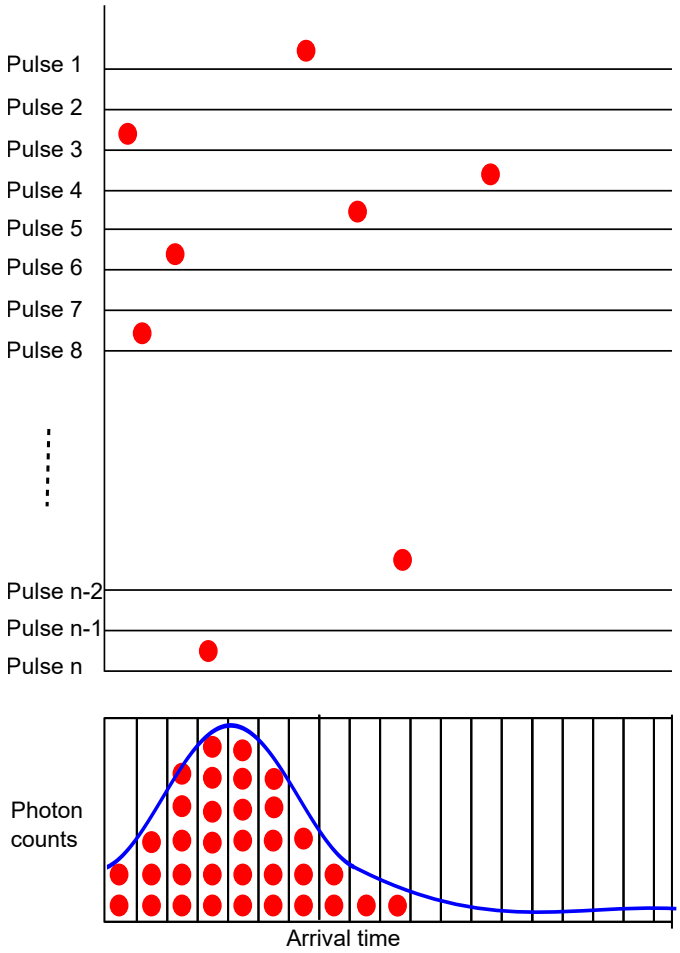

Figure 2.13: Principle of TCSPC. For each signal period, the TCSPC timer records the arrival time of photons. The original optical waveform is then reconstructed from the histogram of photon arrival times.

(TAC), Amplifier (AMP), Analog-to-Digital converter (ADC) and the digital memory. The CFDs in the START and STOP inputs analyse the shape of the individual pulses. Unlike a leading edge discriminator, the CFD module triggers at a zero cross point which is independent of input pulse amplitude. In a leading edge discriminator, the triggering occurs when the leading edge of the generated electrical pulse reaches a predefined threshold. The disadvantage of leading edge discriminator is that it would introduce a large amplitude jitter which will effectively increase the timing jitter of the detector in the order of pulse rise time. The principle of leading edge discriminator is given in Fig. 2.15.

In the constant fraction discrimination method, the input signal is split into two parts. One part is delayed and inverted while the other part is low pass filtered. A zero-crossing point is detected and recorded by summing the undelayed pulse and the delayed and inverted input pulse as given in Fig. 2.16. The cross over point is independent of the pulse

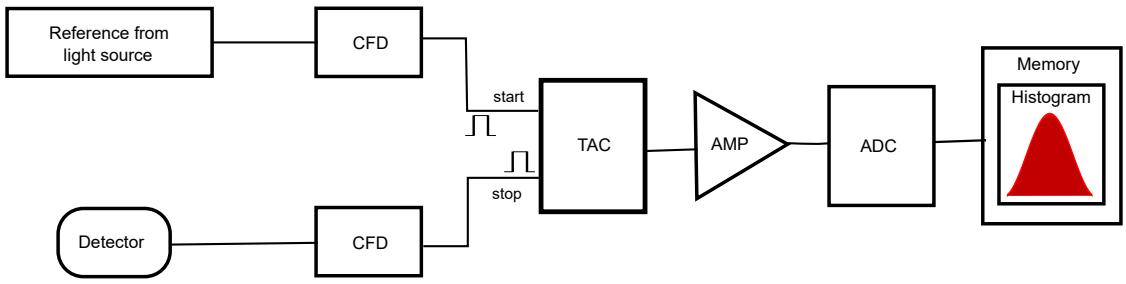

Figure 2.14: Classic TCSPC set up. CFD- constant fraction discriminator, TAC- Time-to-Amplitude converter, AMP- Amplifier, ADC- Analog-to-Digital converter.

amplitude.

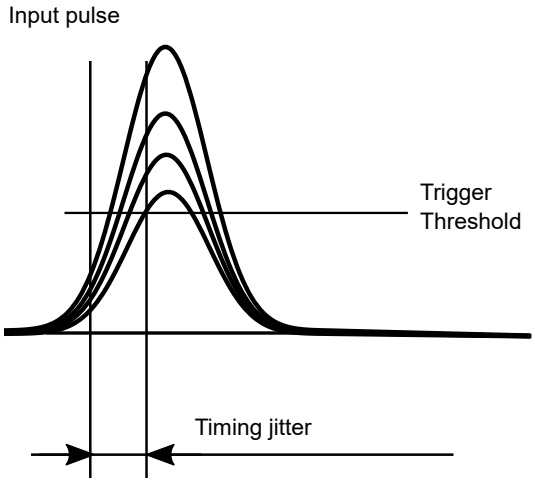

Figure 2.15: Example of leading edge triggering and the corresponding timing jitter. The resulting timing jitter is proportional to the rise time of the pulse.

The outputs from the CFD will feed into the TAC. The TAC is essentially a linear voltage ramp generator that is started by one signal and stopped by the other. The TAC generates an output voltage which is dependent on the temporal position of the photon. The result is a voltage signal that is proportional to time difference between the START and STOP signals. In conventional TCSPC setups, a capacitor is used as the TAC where the START signal switches the voltage on and the STOP pulse switches the voltage off. The signal from the TAC is then passed into the amplifier where it is amplified. The amplified signal is then fed to the ADC and the ADC will generate a digital equivalent of the photon detection time. This digital value will be added in the memory location corresponding to the arrival time of photons. This process is then repeated for each signal period and a histogram of photon distribution is constructed. The original waveform can be reconstructed from this histogram.

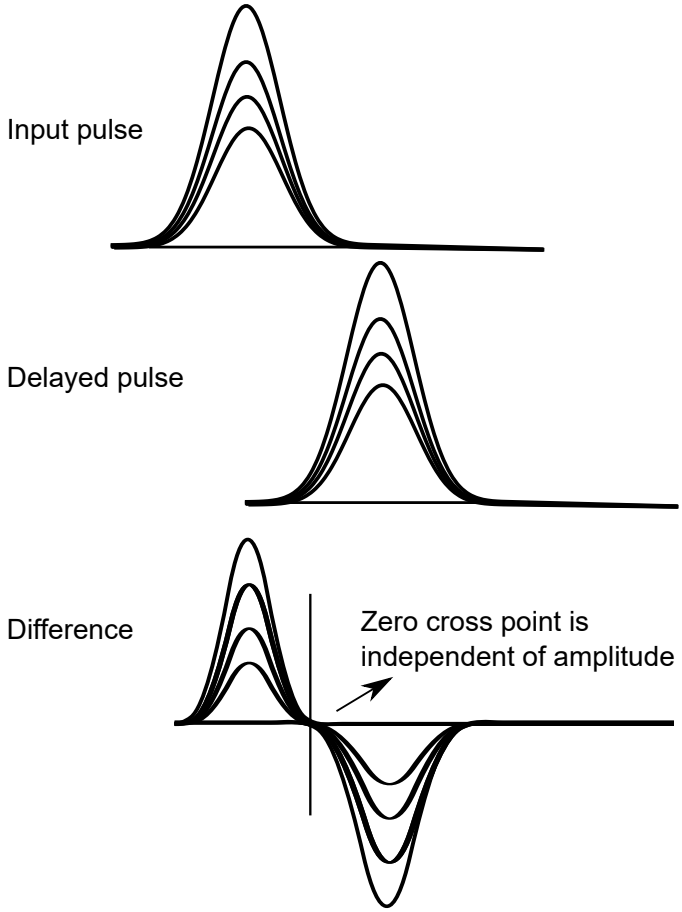

Figure 2.16: Principle of constant fraction triggering.

There are two different operating modes in TCSPC measurements. The forward START-STOP mode and the reverse START-STOP mode [67]. In the forward mode, the synchronisation pulses from the light source is connected to the START input. The advantage of this mode is that no shifting delay line is required and the photon events with long retardation time will be represented in the latter part of the histogram. The disadvantage of the forward mode is that the probability for the detector to detect the STOP signal is very low. If the TAC circuit is started by the START pulse, and does not detect the STOP signal, the circuit needs to reset. This will lead to a delay in the measurements. This can be avoided by operating in the reverse TCSPC mode. In the reverse START-STOP TCSPC mode, the signal from the single photon detector provides the START signal and the synchronisation signal from the light source will provide the STOP signal. The delay in the measurement from the electronics can be greatly reduced in this mode since the TAC always detects the STOP signal. The disadvantage of the reverse mode is that the triggering signal from the light source requires a long delay so that it reaches the TAC input after the signal from the detector [68].

2.4 The Megaframe 32 detector array

Single photon detectors in combination with TCSPC provide an insight into photophysical and photochemical reactions in numerous fields. However, the use of one single photon detector limits their applications in time-resolved photonic imaging due to longer acquisition time. Rapidly increasing demands in devices for imaging applications have driven the development of novel multipixel single photon detector arrays engineered on a single electronic chip which can provide both temporal and spatial informations for time-resolved photonic applications. One of such device is the Megaframe 32, which has already found application in fluorescence lifetime [22], multiplexed WTM [23], and light-in-flight imaging [24].

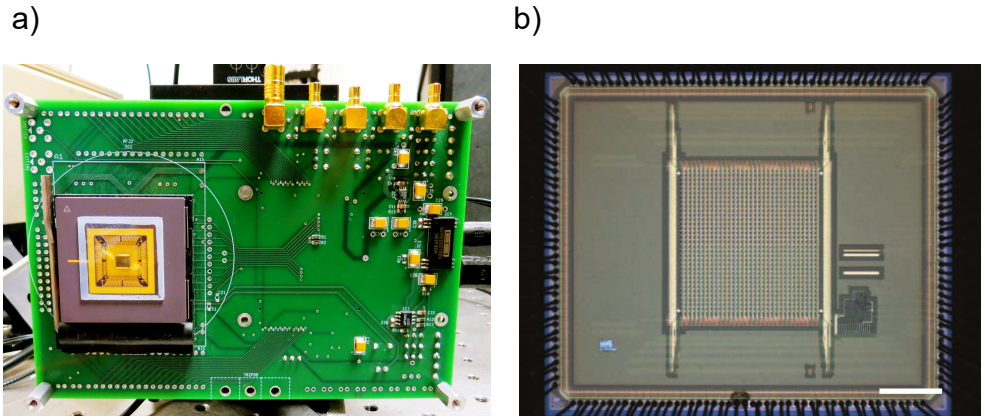

Figure 2.17: a) A photograph of Megaframe 32 detector on the electric board b) Micrograph image of MF32 with 32×32 SPAD pixel array. Scale bar, 800 μm.

The device was fabricated in the CMOS Sensors and Systems Group at the University of Edinburgh by Dr. Robert Henderson and team. The MF32 consists of 32×32 square array of Si-SPADs biased in Geiger mode with single photon sensitivity [22]. Figure 2.17 (a) shows a photograph of the Megaframe 32 with its electric board and Fig. 2.17 (b) represents a micrograph image of Megaframe with 32×32 array SPAD pixels. The pixels can act as individual detector channels which can operate either in the TCSPC or in the photon counting mode, forming an imaging array. The MF32 can be operated with a variety of light sources from high performance pulsed laser to cheaper pulsed diode lasers.

The SPADs are spaced on a 50×50 μm square grid with an active area of ≈ 6 μm and the SPAD array exhibits a physical fill factor of ≈ 1 %. The key SPAD characteristics are given in Table 2.2.

Active diameter	6µm
Pixel dimensions	50µm × 50µm
Pixel fill factor	1.1%
Breakdown voltage	≈13V
Typical excess bias voltage	1.2V
Peak photon detection efficiency at 1V excess bias	≈28%
Peak photon detection efficiency wavelength at 1V excess bias	500nm

Table 2.2: Key SPAD characteristics.

2.4.1 Megaframe design and TDC architecture

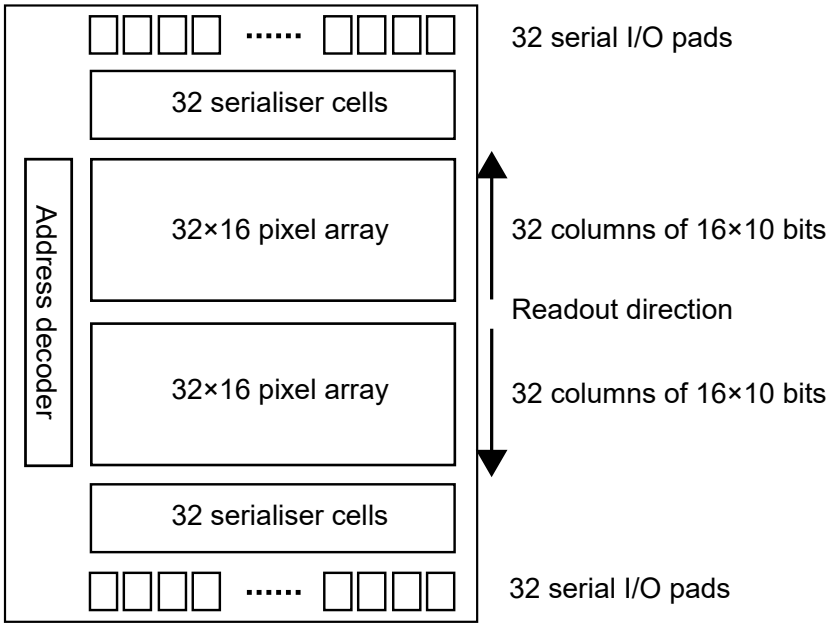

Figure 2.18: Megaframe camera block diagram

A block diagram of Megaframe camera is presented in 2.18. The 32×32 array is subdivided into top half and bottom half each with 32×16 array segments [69]. The 16 element columns in each segment are serialised with dedicated readout circuitry. The address decoder selects pixels from one row of each segments for the readout simultaneously. To transfer data off-chip, one serialiser cell and one I/O pads has been assigned to 16 pixel column in each segment. Therefore, a total of 64 I/O pads are used for the data readout.

The MF32 sensor can support a maximum frame rate of 1 Mfps with a readout bandwidth of 10.24 Gbps (or 500 Kfps at 80 MHz with a readout bandwidth of 5.12 Gbps). Two deserialiser blocks are used to read data from pixels from each half of the segments. The deserilaser generates 32×10 bit data from 32 pixels on the selected row. The sensor

supports a programmable region of interest, allowing specific rows and columns to be disabled. The disabled rows and columns are skipped in the data readout process. A detailed description of the Megaframe camera architecture and firmware can be obtained from [69]. Table 2.3 summaries the key readout system parameters.

Metric	Value
Maximum frame rate	500kfps/1Mfps
Pixel data width	10 bits
Pixel array dimensions	32 × 32
Frame size	32 × 32 × 10 = 10.24kbits
Readout interface	64 serial data pads @ 80/160MHz
Readout bandwidth	10.24kbits@ 1Mfps = 10.24Gbits/s

Table 2.3: Key readout system parameters.

The time-of-arrival measurement in the MF32 detector is performed with the TDC. As mentioned earlier, in the conventional TCSPC technique, the TDC module consists of TAC and the ADC. The tasks performed by the TAC and ADC can be performed with the TDC in the MF32 detector. The selection of TDC design in array detector is different from the single pixel devices as the system requires complicated readout and data processing circuitry. The resolution, power consumption and fast readout aspects are the key considerations in TDC design. Due to the flexibility in achieving high time resolution, complexity, and accuracy, Gated Ring Oscillator (GRO) approach is used in the Megaframe TDC.

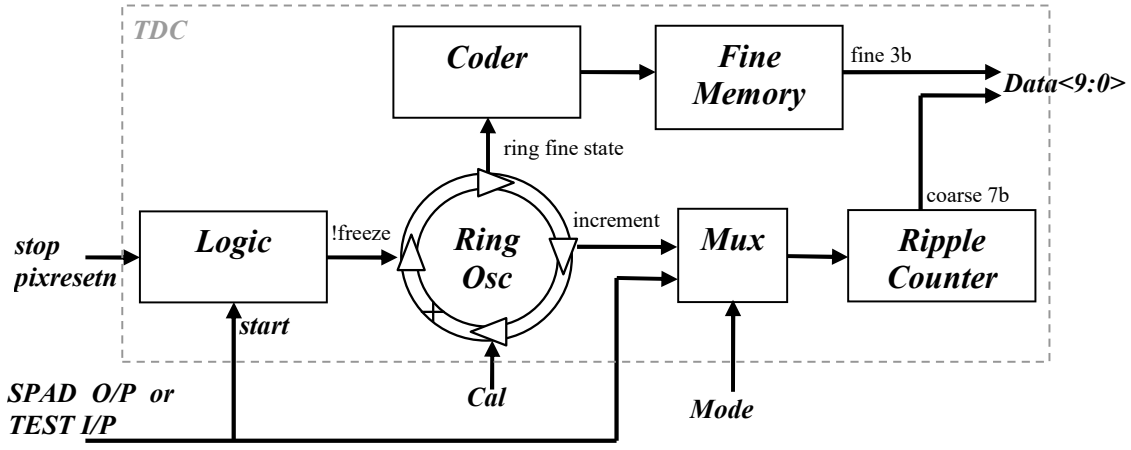

Figure 2.19: GRO TDC block diagram. This figure is adapted from [69].

The flexibility of GRO approach allows the TDC block configured to act in one of the two modes. In photon counting mode, the detector will detect and count the number of

photons within a particular time window. In TCSPC mode, the pixel performs a reverse START-STOP measurement. In this mode, the photon detected by the detector during a frame will trigger the START signal followed by the periodic STOP signal from the laser source. For each pixel, the TDC will generate the digital equivalent of the time difference between the START and the STOP signal based on delay times. Since the TDC is configured in the reverse START-STOP mode, the pixels only triggers when a photon is detected. This reduces the power consumption in pixels which is ideal for fast data read out process in photon detectors.

A combined coarse-fine architecture is employed in TDC design. The GRO TDC consists of a ring oscillator and ripple counter as shown in Fig. 2.19. The output signal from the pixel is fed to the logic block upon photon stimulation. The logic block enables the ring oscillator and ripple counter. The ripple counter generates coarse time to digital conversion for each ring period. For the fast data read out, the coarse and fine bits are combined and buffered to the memory. In photon counting mode, the multiplexer uses to bypass the detector output directly to the counter.

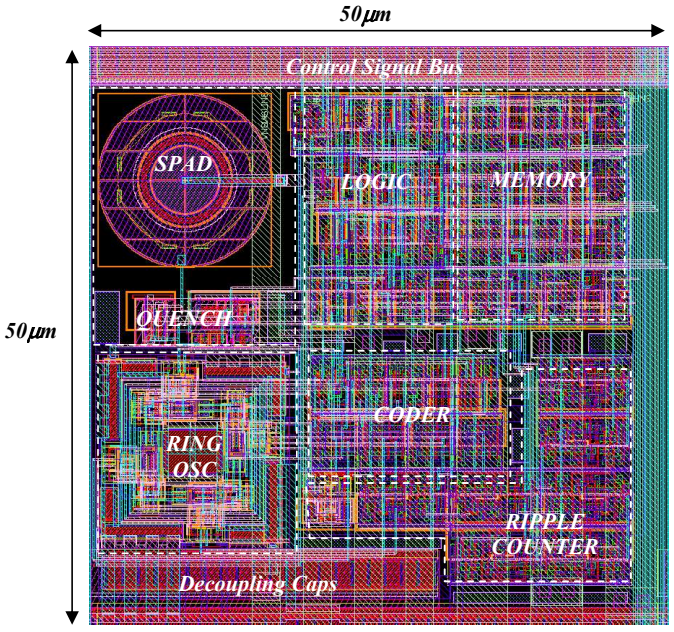

Figure 2.20: GRO TDC single pixel layout with its building blocks. This figure is adapted from [69].

A single pixel in the array is formed by tightly integrating the logic block, GRO, coder, ripple counter and memory along with the SPAD and quench circuit. The pixel layout is given in Fig. 2.20. As mentioned, the pixel forms an area of 50×50 μm. As the fill factor of the detector is very low, it is recommended to use microlens array for maximum fill factor enhancements.

In order to reduce the image distortion due to imperfect power supply along the array, a metal grid is used in each pixel. The low resistivity metal router is responsible for routing all the components deep in the pixel array. This routing conceals most of the pixel except GRO, SPAD and quench blocks. This is clearly visible in Fig. 2.21.

Usually, in the classical reverse mode, the TDC stop signal can be provided from a pulse picker or a photodiode. The picosecond timer in the Megaframe can register the arrival of photons with $\approx$ 50 ps timing resolution with a dynamic range of 54 ns. Since each pixel has its own dedicated TDC, the FWHM of the IRF,the maximum achievable timing resolution, across the entire Megaframe varied from 137 to 174 ps at 532 nm. Since the absorption depth of silicon is wavelength dependent, the IRF itself is wavelength dependent. Though the FWHM of the IRF remains the same, the diffusion tail of the IRF is longer towards the longer wavelength region.

The SPADs in the MF32 exhibit very low dark count rates at room temperature, $\approx$ 50 Hz, and the dominant source of dark count is the thermal generation within the depletion region. The reason for this low DCR is the virtual guard ring structure formed by the SPAD [70]. This structure provides a deep junction and wide depletion region with low tunnelling probability and low deep trap count. Also, the small active area of the pixels reduces the unwanted photon events from the ambient light.

The quality of the structure offers very low after pulsing probability, by minimising the charge flow during breakdown. Each pixel exhibits a maximum photon detection efficiency (PDE) of 28 % at 500 nm for an excess bias 1.4 V [70].

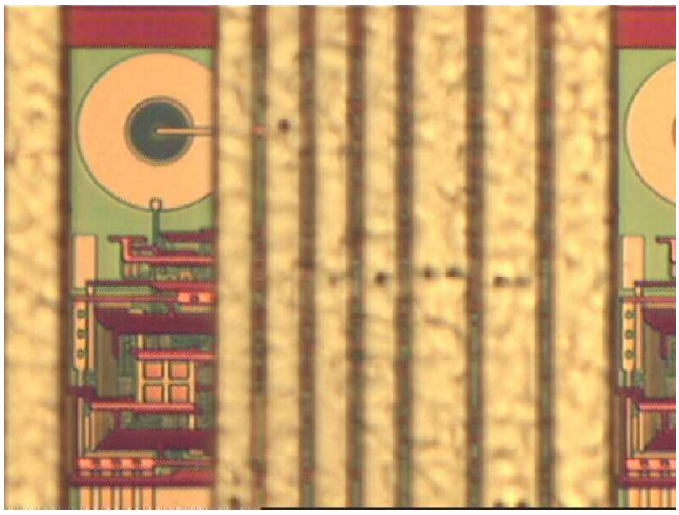

Figure 2.21: Micrograph of GRO TDC single pixel. This figure is adapted from [69].

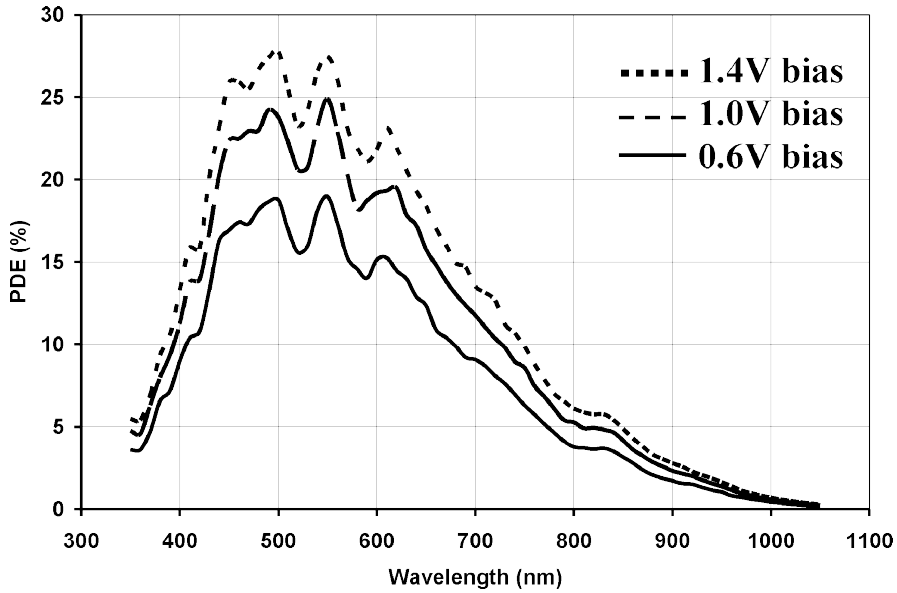

Figure 2.22: PDE versus wavelength for MF32 SPAD for three different excess bias voltages. This Figure is adapted from [70].

The factors affecting PDE are applied voltage, carrier which initiates the avalanche current, doping level, and electric field conditions. The PDE versus illumination wavelengths of the SPAD for three excess bias voltages of 0.6 V, 1 V and 1.4 V are presented in Fig. 2.22. The perturbation in the response is due to the constructive and destructive interference effects of light above the detector which consists of different stacks of optical layers with varying refractive indices.

2.5 Chapter summary

In this Chapter, a literature review on common single photon detectors is presented. The working principles and applications of early stage single photon detectors such as PMT, MCP-PMT, APD, SPAD were described. The basic designs of PMT and MCP-PMT are given with a comparison of their timing circuits. The timing jitter of PMTs with discrete dynodes is $\approx$ 300 ps FWHM. The main reason for this large timing jitter is the transit time difference between the emitted photoelectrons. With the multichannel plates, the timing jitter of the PMT can be greatly reduced due to the negligible transit time differences between the photoelectrons. The voltage-current characteristics of a p-n junction diode is explained. The electric field profile, gain, noise, and SNR of APD were presented. The Geiger mode in APD and the basic quenching circuits in APDs were explained. The

selection of quenching circuit in an APD is crucial as it affects the dead time of the detector. The timing jitter and physical parameters of thick and thin junction Si-SPADs were compared. A comparison of single photon detectors were listed with different performance parameters. TCSPC technique is explored with the basic TCSPC system and their applications. The imaging capability, key characteristics, and the applications of a novel multipixel single photon detector (Megaframe 32) were discussed. The device design and TDC architecture of the Megaframe were presented. With individual TDC, the Megaframe pixels offers a timing resolution of $\approx$ 50 ps for time-resolved imaging. Each pixel is 10 bit long making a total dynamic range of 54 ns. The timing jitter of Megaframe pixels varies from 137 ps to 174 ps due to the individual TDC design. The PDE of the Megaframe SPAD is discussed for different excess bias voltages. Due to the bandgap of silicon, the PDE of the SPAD is limited within the 400 nm to 1100 nm spectral region. The maximum PDE of Megaframe SPAD is found to be 28% at 500 nm for an excess bias 1.4 V.

Chapter 3

Guided wave optics - background

3.1 Introduction

Guided wave optics represents the propagation and manipulation of light in dielectric waveguides. Wave propagation in waveguides plays an important role in photonics and acoustics. The simplest and widely used waveguides are single-mode and multimode fibres along with more sophisticated photonic crystal fibres (PCF). These waveguides confine radiations in the visible portion of the spectrum as different modes by repeated reflections from the inner walls with different phase velocities. SMFs has a small core which enables tighter light confinements and effective light transmission owing the highest tolerances in optical alignments for photonic applications. Multimode fibres (MMFs) on the other hand, carry more informations because of the larger core size where the light can propagate in many modes over long distances. Photonic lantern (PL) is a special type of waveguide system which enables a low-loss transition between single-mode and multimode systems by merging them into a common platform [72]. This review Chapter introduces fibre optics and the mechanisms that take place when a light pulse propagates along the fibre. Dispersion, cross-coupling, loss in optical fibre are explained. Guided modes and coupled mode theory is explained with theoretical derivations. Fabrication of fibre-PL and light propagation through a PL are explored in this Chapter.

3.2 Fibre optics

Fibre optics is a technology that uses dielectric threads to transmit light. Conventional optical fibres consist of a higher refractive index region known as core, and a surrounding cladding region with lower refractive index. In such fibres, light remains in the fibre core by reflection at the core-cladding interface by total internal reflection (TIR). When the

light signal propagates along the fibre, different mechanisms can distort the signal quality. The aim of this Section is to provide a brief introduction about fibre optics and different mechanisms such as dispersion, cross-coupling, loss. Guided modes and coupled mode theory (CMT) in guided wave optics is explained with theoretical derivations.

3.2.1 Dispersion in optical fibres

The light transmission properties of an optical fibre is governed by bandwidth-length product. The bandwidth of an optical signal is influenced by dispersion effects in the fibre which causes the broadening of transmitted optical signal. The different types of dispersion mechanisms in fibre include, modal, material, and waveguide dispersions. Modal dispersion arise from the propagation delay differences between the mode groups within a MMF. As the different modes which constitute a pulse in a MMF travel along the channel at different group velocities, the pulse width at the output is dependent upon the transmission times of the slowest and fastest modes. Modal dispersion can be reduced by choosing parabolic refractive index profile as given by most of the graded index fibres [73].

The bandwidth-length product of a SMF is limited by the chromatic dispersion in the fibre. Chromatic dispersion in fibres results from the wavelength-dependent variation of the mode index which is caused by two effects- material and waveguide dispersions. Material dispersion results from the variation of refractive index profile with wavelength in the fibre. Waveguide dispersion arise from the spectral variation due to the guidance effects within the fibre structure. The expected pulse broadening due to chromatic dispersion is given by [74],

$$\Delta\tau = |D|\ L\ \Delta\lambda \tag{3.1}$$

where, D is the dispersion, L is the length of the fibre, and $\Delta\lambda$ is the spectral width of the optical source.

The contribution from waveguide dispersion can be used to design fibres with zero dispersion at desired wavelength window for fibre optic applications. As an example, Fig. 3.1 shows the material dispersion, the waveguide dispersion, and the total dispersion as a function of wavelength for a conventional step index SMF. Note that the waveguide dispersion compensates the material dispersion and the total dispersion goes through zero at a wavelength of 1.27 μm. This zero material dispersion point can be shifted by addition of suitable dopants during the fibre fabrication process. These type of fibres are

known as dispersion shifted fibres. For example, to operate with the lowest transmission loss possible, the G653 single mode fibre was designed to exhibit zero dispersion at a wavelength 1.55 μm [75]. However, at zero dispersion wavelength, the optical pulse still undergoes broadening due to third order dispersion (TOD) [76]. TOD is related to the third term in the expansion of spectral phase versus angular frequency offset. It is crucial to consider TOD in long distance transmission, as for larger TOD, the pulse width does not proportional to guide length [77, 78].

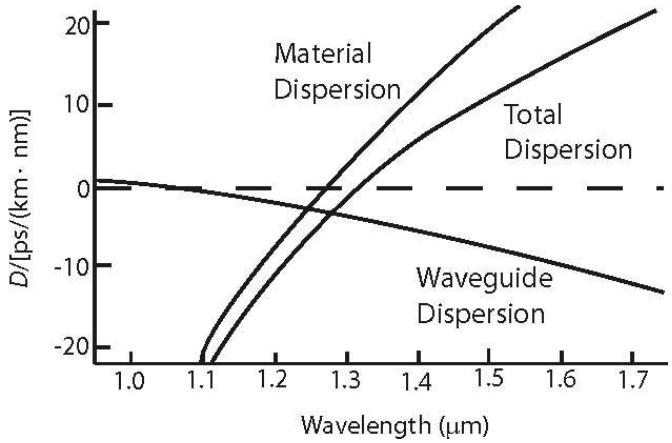

Figure 3.1: Dispersion characteristics of a standard step index single mode fibre. This Figure is adapted from [79].

Polarisation mode dispersion (PMD) is another type of dispersion present in optical fibres. Due to the birefringence in the fibre, the two orthogonal components of optical signal travels along the fibre as ordinary ray and extra-ordinary ray with different group velocities. This results the two components reaches at the output of the fibre at different time. PMD is a limiting factor in multigigabit long-haul optical fibre transmission systems [80].

3.2.2 Loss in optical fibre

The propagation loss is one of the most important factor in an optical fibre for transmitting optical. The loss should be minimised in order to achieve maximum transmission distance along the fibre. Loss in optical fibres is divided into extrinsic and intrinsic losses. Extrinsic losses are specific to geometry and handling of the fibre. There are three basic types of extrinsic losses; bending losses, coupling losses, and connector losses. Bending losses are induced by the distortion of fibre from the ideal straight-line configuration. Bending losses can occur as result of macro-bends or micro-bends. The loss occurs when the energy in the evanescent field at the bend exceeds the velocity of light in the cladding,

causing energy to be radiated from the fibre. For MMFs, the critical radius of curvature R_C of a macro-bend is given by [73],

$$R_C \simeq \frac{3n_1^2\lambda}{4\pi(n_1^2 - n_2^2)^{3/2}} \tag{3.2}$$

where n_1, n_2 are the refractive indices of the core and the cladding respectively.

Loss from micro-bends is caused by small radius bends in an optical fibre. Micro-bends arise from the manufacturing defects, mechanical constrains during the fibre laying process and environmental variations (temperature, humidity, pressure) during the fibre's lifetime. Although micro-bends causes loss in fibre optic applications, it is also beneficially exploited in designing fibre optics sensors for different applications [81].

The term coupling loss refers to an optical fibre not being able to propagate all the incoming light rays from an optical source. This can happen due to the mismatch in NA of the coupling optics such as lens with the NA of the optical fibre. The alignment of free-space optics with the fibre is another key factor in introducing insertion loss while coupling light into the fibre from the source [82]. The insertion loss of a fibre connector or a fibre splice is another key factor which decides the coupling loss. Connector losses are associated with the coupling of the output of one fibre with the input of another fibre, or coupling with detectors or other components. These losses can be minimised by choosing the fibres with same core size and NA or by improving the fibre splicing techniques. The most common and realistic method to evaluate fibre coupling loss is the ray-tracing method [83], which involves more effects in the fibre and not restricted to the mismatches only in core diameters or NA.

Intrinsic attenuation is caused by the impurities inherent to the fibre during the manufacturing process. When a photon hits the impurities in the fibre, it scatters or is absorbed. The most common impurity in the fibre is the hydroxyl (OH^-) molecules present in silica. OH^- absorbs near infra-red and infra-red (NIR-IR) light in the spectrum and therefore fibres with low OH^- concentration are preferred for transmission in telecommunication wavelengths [84]. The silica glass has little intrinsic absorption in the NIR region. However, the optical attenuation against wavelength characteristics for pure glass shows a fundamental absorption edge in the ultraviolet wavelength region [85]. This strong absorption band is due to the stimulation of electron transitions in the glass by higher energy excitations and the absorption by impurities. At wavelengths 2.7 μm-4.3 μm, the OH interactions in fused silica causes significant absorption bands. Also at wavelengths above 9 μm, the photons interact with the molecular vibrations within the glass, gives strong

absorption bands. The absorption bands of different glasses various as the light interacts differently with different glass composites [86]. Unlike scattering, absorption loss can be limited by controlling the amount of impurities during the manufacturing process.

Loss from scattering occurs when the light experiences a variation in refractive index in the fibre. Scattering losses are categorised into linear and non-linear scattering losses. Linear scattering can be divided into two types: Mie scattering and Rayleigh scattering. Mie scattering is caused by the non perfect cylindrical structure of the fibre and imperfections like irregularities in the core-cladding interface, diameter fluctuations, strains and bubbles. Rayleigh scattering arises due to the refractive index fluctuations induced by the density and composition variations in the core. Rayleigh scattering is characterised by effective scattering coefficient which is proportional to $1/\lambda^4$. Rayleigh scattering can be reduced to a large extent by operating in the longest wavelength possible. Nonlinear scattering losses results the optical power from one mode is transferred in either the forward or backward direction to the same, or other modes, at different frequencies. The two dominant types of nonlinear scattering are: 1) Stimulated Brillouin scattering; which is the modulation of light through thermal molecular vibrations. In this process, the incident photon produces a phonon of acoustic frequency as well as a scattered photon. 2) Stimulated Raman scattering; in which the incident photon produces a high energy photon along with the scattered photon.

3.2.3 Guided modes and mode parameters

This Section provides a brief introduction about guided modes in weakly guiding fibres. In a fibre with cylindrical geometry, light can propagate in different modes thorough the fibre. Two integers, l and m is needed to specify the modes as the cylindrical waveguide is bounded in two dimensions. When the electric field is perpendicular to the direction of propagation and hence E_z = 0, the corresponding magnetic field H is in the direction of propagation . Such modes are known as transverse electric (TE) mode. Similarly, when there is a component of electric field is in the direction of propagation but the magnetic field component, is zero (H_z = 0), then the modes are termed as transverse magnetic (TM) mode. When the total field lies in the transverse plane, both the E_z, H_z are zero, then transverse electromagnetic (TEM) waves exist. In weakly guiding approximation where the relative index difference is $\Delta \ll 1$, the approximate solutions for the modes are given by two linearly polarised (LP) components. The subscripts l and m corresponds to the electric field intensity profile for a particular LP mode. Here, the simplest formulas to

find the mode parameters and mode delay is outlined from Gloge [87] for weakly guiding fibres.

Consider an optical fibre with step index profile and cylindrical geometry with Cartesian coordinates (x, y) and cylindrical coordinates (r,ϕ) . Let n_1 be the refractive index of the core, n_2 be the refractive index of the cladding and the core radius be a. The propagation modes in the fibre are characterized by the dimensionless parameter, v-number or normalised frequency,

$$v = ka(n_1^2 - n_2^2)^{\frac{1}{2}} \tag{3.3}$$

where, $k = \frac{2\pi}{\lambda}$ is the wave-number in free space. The mode field inside the core can be expressed as Bessels function $J(ur/a)$ and the mode field outside the core is expressed as modified Hankels function $K(wr/a)$. The parameters u and w are defined as,

$$u = a(k^2 n_1^2 - \beta^2)^{\frac{1}{2}} \tag{3.4}$$

$$w = a(\beta^2 - k^2 n_2^2)^{\frac{1}{2}} \tag{3.5}$$

Where β is the propagation constant of the mode which has a value within the interval $n_1 k \geq \beta \geq n_2 k$. For a MMF, the mode-dependent β value depends on the effective refractive index of the mode in which the light propagates. The parameters u,w for all modes can be obtained by matching the field at the core-cladding interface. The propagation constant and all other parameters can be found from Equations 3.3, 3.4 and 3.5.

When v-number is less than 2.405, only the fundamental mode can propagate along the fibre. When the wavelength of the source reduces significantly, the v-number becomes greater than 2.405 and the fibre become multimode.

For weak guidance,

$$\Delta = (n_1 - n_2)/n \ll 1 \tag{3.6}$$

Following Equations 6, 7 and 8 of reference [87], the characteristics equation for the linearly polarised modes is derived as,

$$u[J_{l-1}(u)/J_1(u)] = -w[(K_{l-1}(w)/K_l(w)] \tag{3.7}$$

For weakly guiding fibres, the longitudinal components are weaker compared to the transverse component. Solving Equation 3.7, allows the calculations of eigenvalues u and w

and hence β as a function of normalised frequency. This will give the dependence of various modes on optical wavelength and the propagation characteristics of the various modes can be determined.

In order to calculate the propagation constant for any particular fibre configuration independently, we define a new parameter,

$$b = 1 - (u^2/v^2) = [(\beta^2/k^2) - n_2^2]/(n_1^2 - n_2^2) \tag{3.8}$$

For small index differences, the equation reduces to

$$b = [(\beta/k) - n_2]/(n_1 - n_2) \tag{3.9}$$

The quantity b is the normalised propagation constant which is proportional to β.

From Equations 3.6, 3.9, the propagation constant can be calculated as,

$$\beta = n_2 k(b\Delta + 1) = n_2 k(1 + \Delta - \Delta(u^2/v^2)) \tag{3.10}$$

Following reference [87], the group delay of the envelope of light signal is given by,

$$\tau_{gr} = (L/c)(d\beta/dk) \tag{3.11}$$

Differentiating Equation3.11 considering the k dependence of Δ, n_2, b we obtain,

$$\tau_{gr} = (L/c)[d(n_2 k/dk)] + n_2\Delta[d(vb)/dv] \tag{3.12}$$

The difference in group delay between any modes can be calculated from equation 3.12. For a MMF where light propagates as many spatial modes, we obtain a group spread of (L/c)[1-(2/v)]$(n_1 - n_2)$].

Coupled mode theory in guided wave optics

The basic coupled mode system consists of two or more dielectric waveguide systems placed in close proximity. The energy in any particular mode is distributed between the

core and the cladding of the waveguide. The light in a single-mode optical waveguide follows a distribution which peaks at the centre and then tails off at the core-cladding interface. Part of the light energy distributed in the cladding is called the evanescent tail [88]. If the evanescent tails of two adjacent cores of an optical waveguide overlap, mode energy beats back and forth between the two cores depending upon the core separation and interaction length. This coupling is termed as evanescent wave coupling. Due to the coupling of energy between cores, light initially incident on one core eventually coupled into other core of the waveguide. As an effective and simplest analysis tool, coupled mode theory (CMT) is extensively used to describe the interaction and propagation of light in guided-wave optics. Developed by Pierce [89] and Miller [90], the initial application of CMT was on microwave oscillations and propagation. The first demonstration on CMT in guided-wave optics was in early 1970's by Snyder [91], Marcuse [92], Yariv [93], and Kogelnik [94]. The theory of two coupled optical waveguides is explained below [95–97].

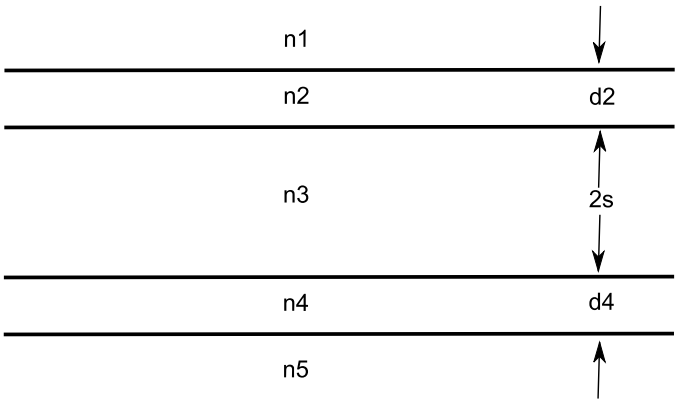

Figure 3.2: Schematic diagram of a directional coupler

When two straight waveguides are placed close to each other, the evanescent fields of the guided modes overlap and the modes interacts with each other. For simplicity, a uniform directional coupler consists of two identical waveguides placed in close proximity is considered (Fig. 3.2). Close proximity indicates that the distance between the waveguides is in the order of MFD of the waveguide modes so that their modes can overlap. The modal solutions for such a system is time consuming and difficult to find. Conventional CMT provides the accurate analytical solutions to mode coupling in directional coupler devices.

When two waveguides are far apart, there modes are isolated. The modal field varies along the direction of propagation (z) in a time dependent manner, exp ($i\beta' z$), where β' is the propagation constant of the mode. The variation of the mode electric field amplitudes

of two waveguides, a_1 and a_2 along the propagation direction can be expressed as,

$$i\frac{da_1}{dz} = -\beta_1 a_1 \tag{3.13}$$

$$i\frac{da_2}{dz} = -\beta_2 a_2 \tag{3.14}$$

where, β_1 and β_2 are the propagation constants of the two modes.

When the two waveguides are in close proximity, the modes interact with each other as a result of evanescent coupling. The mode amplitudes of one waveguide will be modified by the other. In such circumstances, the Equations becomes,

$$i\frac{da_1}{dz} = -\beta_1 a_1 - \kappa_{12} a_2 \tag{3.15}$$

$$i\frac{da_2}{dz} = -\beta_2 a_2 - \kappa_{21} a_1 \tag{3.16}$$

where κ_{12} , κ_{21} are the mutual coupling coefficients which describes the strength of evanescent coupling. To solve these equations, one can assume that two evanescently coupled waveguides support modes with a propagation constant β are a superposition of modes with amplitudes A and B,

$$a_1 = A \exp(i\beta z) \tag{3.17}$$

$$a_2 = B \exp(i\beta z) \tag{3.18}$$

Substituting Equations 3.17 and 3.18 in Equations 3.15 and 3.16 and rearranging,

$$\beta = \frac{1}{2}(\beta_1 + \beta_2) + \left\{\frac{1}{4}(\beta_1 - \beta_2)^2 + \kappa^2\right\}^{1/2} = \beta_{s,a} \tag{3.19}$$

where, $\kappa = \sqrt{\kappa_{12}\kappa_{21}}$. The coupled waveguides supports two independent modes, the symmetric mode with propagation constant β_s and asymmetric mode with propagation constant β_a. The solution of Equations 3.15 and 3.16 is given by,

$$a_1(z) = A_s \exp(i\beta_s z) + A_a \exp(i\beta_a z) \tag{3.20}$$

$$a_2(z) = \frac{\beta_s - \beta_1}{\kappa_{12}} A_s \exp(i\beta_s z) + \frac{\beta_a - \beta_1}{\kappa_{12}} A_a \exp(i\beta_a z) \tag{3.21}$$

If light is launched at the first waveguide at the input, ie; a_1 (z=0) = 1 and a_2 (z=0) = 0. Hence,

$$A_s = \frac{\beta_1 - \beta_a}{\beta_s - \beta_a} \tag{3.22}$$

$$A_a = \frac{\beta_s - \beta_1}{\beta_s - \beta_a} \tag{3.23}$$

If the waveguides are lossless, then the total power needs to be conserved. After normalising the mode amplitudes, the total power can be written as

$$P(z) = |a_1|^2 + |a_2|^2 \tag{3.24}$$

Substituting Equations 3.22 and 3.23 in Equations 3.20 and 3.21,

$$|a_1|^2 = 1 - \frac{k^2}{\frac{1}{4}(\beta_1 - \beta_2)^2 + \kappa^2} \sin^2 \left[\left\{ \frac{1}{4}(\beta_1 - \beta_2)^2 + \kappa^2 \right\}^{1/2} z \right] \tag{3.25}$$

$$|a_2|^2 = 1 - |a_1|^2 = \frac{k^2}{\frac{1}{4}(\beta_1 - \beta_2)^2 + \kappa^2} \sin^2 \left[\left\{ \frac{1}{4}(\beta_1 - \beta_2)^2 + \kappa^2 \right\}^{1/2} z \right] \tag{3.26}$$

From Equations 3.25 and 3.26, the maximum energy transfer between the modes occurs with a period $2L_c$ where,

$$L_c = \frac{\pi}{2\left[\frac{1}{4}(\beta_1 - \beta_2)^2 + \kappa^2\right]^{1/2}} \tag{3.27}$$

where L_c is the coupling length. For identical waveguides, $\kappa_{12} = \kappa_{21} = \kappa$ and $\beta_1 - \beta_2$=0. Then from Equations 3.25, 3.26 and 3.27,

$$|a_1|^2(z) = \cos^2(\kappa z) \quad \text{and} \quad |a_2|^2(z) = \sin^2(\kappa z) \tag{3.28}$$

$$L_c = \frac{\pi}{2\kappa} \tag{3.29}$$

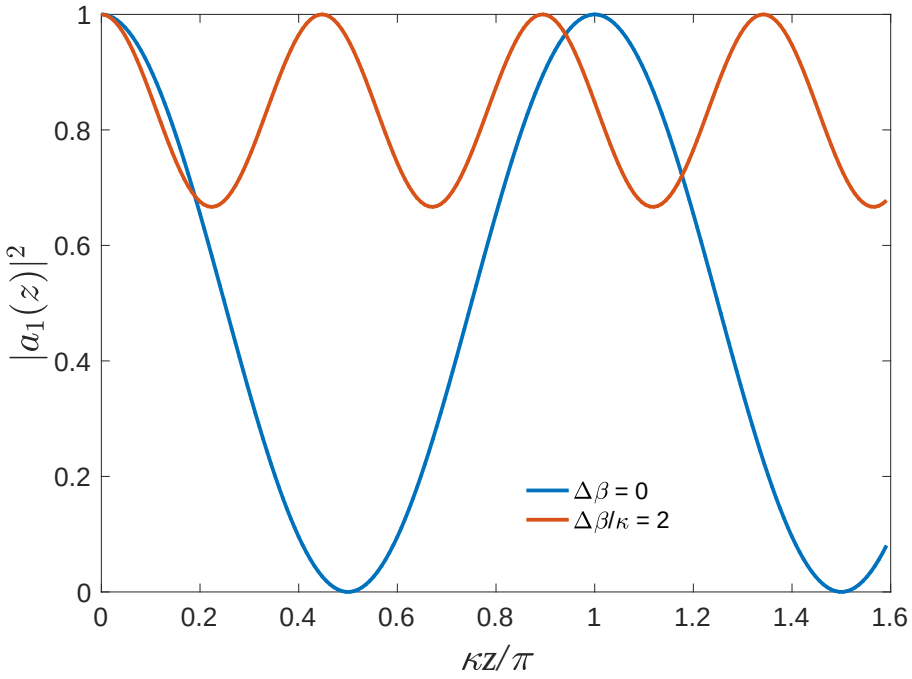

Figure 3.3: Variation of normalised optical power in directional coupler for $\Delta\beta = 0$ and $\Delta\beta/\kappa = 2$. Note that the complete power transfer occurs only when $\Delta\beta = 0$.

The variation of power in the waveguide mode a_1 as a function of interaction length for $\Delta\beta$= 0 and $\Delta\beta/\kappa$ = 2 is shown in Figure 3.3. Note that when the interaction length is equal to coupling length, L_c, maximum power transfers to the second waveguide.

For a coupled waveguide system consists of many waveguide modes, assuming the next nearest coupling is negligible, we can generalise Eq. 3.15 in the form,

$$i\frac{da_n}{dz} = -\beta a_n - \kappa(a_{n+1} + a_{n-1}) \tag{3.30}$$

3.3 The photonic lantern

A PL is a device which enables the efficient coupling of light between two multimode systems- the first being a set of single-modes, and the second being a traditional multi-mode system such as MMF or waveguide. The PL consists of a large multimode core and an array of single-mode cores with a slow optical transition region where the two regions

are connected. The light coupled into the multimode end of the PL will be distributed into the single-mode cores with minimal loss depending on the length of the transition region and the number of modes in each multimode system [98]. For a low loss transformation, the transition needs to be adiabatic and the number of single-mode cores should be equal to or greater than the number of modes supported by the multimode end. Both end can be used as input depending upon the application. Figure 3.4 shows a schematic diagram of a PL made by tapering a bundle of single-mode fibres.

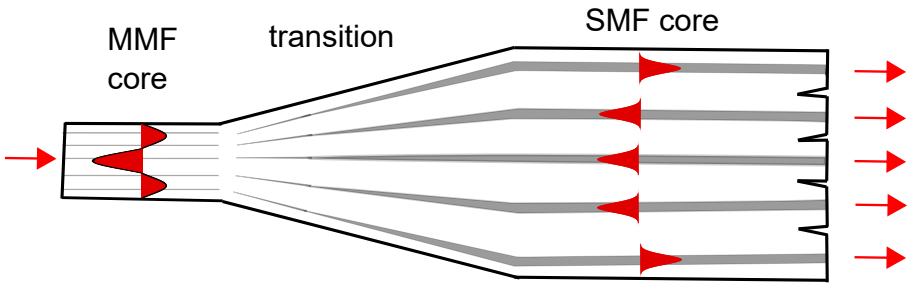

Figure 3.4: Schematic diagram of photonic lantern made by tapering a bundle of single-mode fibres.

3.3.1 Photonic lantern fabrication

Originally invented for next generation astronomical applications, a PL interfaces multimode and single-mode systems allowing the efficient use of single-mode photonics with multimode light. Two common approaches are used in PL fabrication. The first method is based on fibre tapering, where the single-mode cores are placed inside a capillary and tapered down to form a multimode core. The second method utilises ultrafast laser inscription (ULI), to inscribe waveguide structures in transparent optical chips. The fibre tapering process in fabricating fibre based photonic lantern is reviewed here.

Fibre PLs are made by narrowing down the fibre over a predefined length by heating and permanent stretching using a fibre tapering apparatus. The fibre held in an elongation stage and a heat is applied using a burner stage to a portion of the fibre. The controlled movement of the flame along the selected region on the fibre and pulling the fibre to either sides results in the formation of a waist region where the heat is applied. Figure 3.5 presents the fibre tapering process together with the tapered fibre structure. A uniform heat source is required for a tapered structure with uniform dimensions. This can be achieved by flame brush technique where the heat source scanned constantly along the fibre in a well controllable manner.

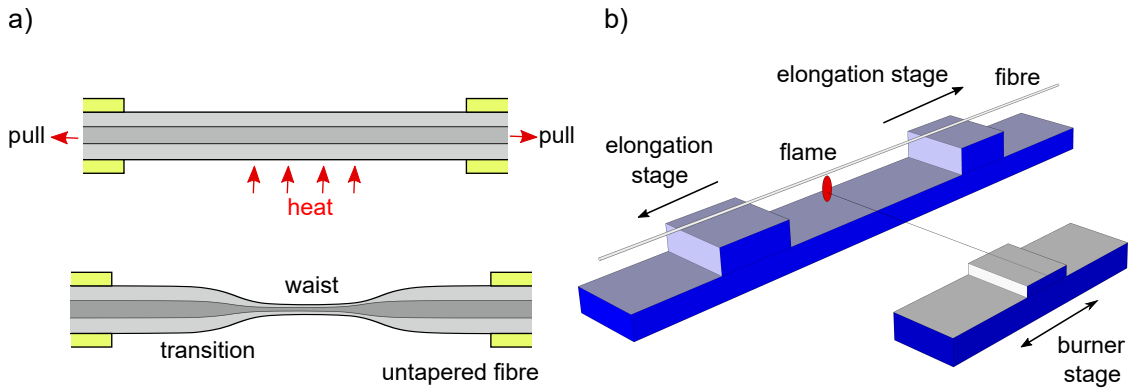

Figure 3.5: Schematic diagram of (a) Taper formation by heating and stretching the fibre. (b) The tapering apparatus consists of burner and elongation stages.

Two types of fibre-PLs are made using tapering. The first type involves stacking and fusing several SMFs in a capillary by hand and tapering down, forming a multimode core. The second type, MCF-PL, a MCF is placed in a low index capillary and tapered in a similar way forming a multimode core at the construction.

3.3.2 Light propagation through a photonic lantern

The effect of tapering a fibre and the light propagation through PL can be explained by first considering the simplified example of a tapered SMF. The SMF used in telecommunication application has a core diameter and cladding diameter of 9 μm and 125 μm respectively with an NA 0.11. As shown in Fig. 3.6, light at 1550 nm propagates along the untapered fibre region confined in the core as the fundamental mode due to the refractive index contrast of the core and the cladding. However, when the light reaches the tapered region, the size of the core is too small for the light to guide.

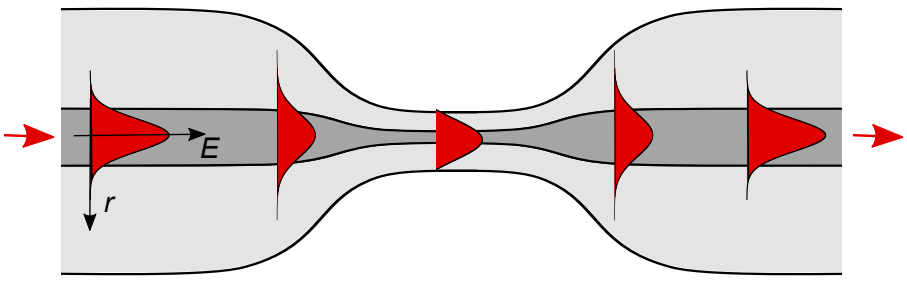

Figure 3.6: Pictorial representation of light propagation through a tapered SMF. The mode shape in red represents the transverse position of mode field as a function of position.

The light will then be progressively guided by the air which effectively acts as the cladding. To reach the untapered region, light has to pass through the transition region. If the transition is gradual enough, the transformation of light inside the core follows the successive versions of the same mode. As an example, from Fig. 3.6, light starting from the untapered region as fundamental mode spreads out at the tapered region and evolves as fundamental mode of the waist and recaptured as the light reaches the untapered region on the other end. Such type of transition is called adiabatic [99, 100] transition. For adiabatic transition, the taper angle should be small so that the power loss in the modes is negligible when its propagating along the taper. The parameters such as propagation constant and field of the modes can be obtained as the solution to the wave equations with the geometry of the local cross-section.

In order to understand how the mode loss relates to the taper angle and radius, consider the coupling between the first two modes. The coupling between modes in the transition region depends on the taper angle. The local taper angle at any position in the taper is defined by [100],

$$\Omega(z) = \big(\rho(z)/2\pi\big)\big(\beta_1(z) - \beta_2(z)\big) \tag{3.31}$$

where, $\Omega(z)$ is the taper angle at position z along the taper, $\rho(z)$ is the core radius, $\beta_1(z)$ and $\beta_2(z)$ are the propagation constant values of HE_{11} and HE_{12} modes respectively. For low loss transition and coupling, the measured angle should be below $\Omega(z)$. If the measured angle exceeds the $\Omega(z)$ value, then the local coupling is significant which leads to mode power loss.

A PL can be described as many SMFs tapered together and the light propagation through PL can be explained using the same logic given in Fig. 3.6. For the low propagation loss of light in PL, the number of modes supported by the multimode end should be equal to the number of single-mode cores,

$$N_{out} = N_{in} \tag{3.32}$$

Three factors can influence the light propagation loss in the PL: mode-number mismatch, non-adiabatic transitions, and asymmetry in the transition region. Light at certain multimode state at the multimode core will be distributed to the single-mode cores at certain phase and amplitude. When coupling from the other direction, light from a single-mode core can excite many multimode states at the multimode end. Figure 3.7 shows a

schematic representation of light propagation through a PL when light coupling from both ends.

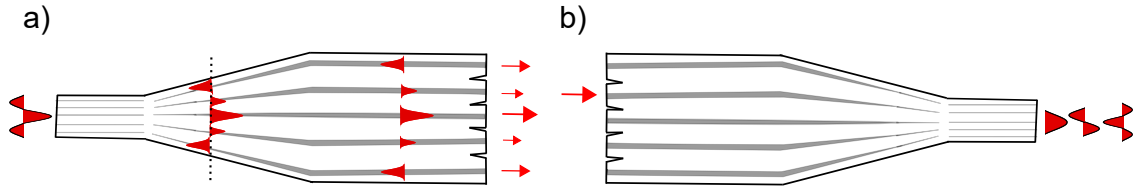

Figure 3.7: Schematic representation of light propagation through a photonic lantern. (a) Light coupled onto the multimode core of the PL will be distributed to the single-mode cores depending upon a region in the transition (dotted line) where the SM cores act as individual waveguides. (b) Light coupled from the single core to the multimode core.

The number of modes supported by the multimode end of a tapered multicore fibre is given by [72],

$$N_{MM} \approx \left(\frac{\pi d \mathrm{NA}}{2\lambda}\right)^2 \tag{3.33}$$

Where, d is the diameter of the multimode core, NA is the numerical aperture of the multimode core, and λ is the wavelength of light.

Assuming all the input modes are excited equally, the equation for loss is given by,

$$\text{loss} = 10 \log_{10}\left(\frac{N_{out}}{N_{in}}\right) \text{dB} \tag{3.34}$$

As the mode number in the multimode core of a PL changes with wavelength and the number of single-mode cores are fixed, mode matching is only possible with only one wavelength. In that case, the wavelength-dependant loss due to mode-mismatch is given by,

$$\text{loss} = 20|\log_{10}\left(\frac{\lambda}{\lambda_0}\right)| \text{dB} \tag{3.35}$$

where, λ_0 is the wavelength at which the mode-number is matched. The easiest way to avoid the loss due to mode number mismatch is the "light bucket" method where the output of the PL supports more modes than the input.

3.4 Chapter summary

A literature review on guided wave optics is presented in this Chapter. Different types of dispersions in fibres such as modal, material, and waveguide dispersions and their effects on signal transmission are briefly explained. Modal dispersion occurs in MMFs where different group velocities of the mode groups results in the broadening of the transmitted optical signal. This can be reduced by MMFs with parabolic refractive index profile. In SMF, the major contribution in pulse broadening is the material dispersion. Extrinsic and intrinsic losses in optical fibres have been presented. Extrinsic losses are classified into three types- bending losses, launching losses and connector losses. The effect of fibre bend radius on attenuation is outlined. The launching losses can be greatly minimised by choosing the coupling lens with the same NA that of the optical fibre. The intrinsic attenuation caused by the impurities presented in fibre. The common impurity present in the fibre is the OH^- molecule which absorbs light in the NIR-IR portion of the spectrum. It is observed that these impurities can cause significant absorption and hence the attenuation of the signal when propagates along the fibre. Intrinsic loss can minimise by choosing the best fabrication parameters during the fibre drawing process. Attenuation due to linear and non-linear scattering in optical fibres have been presented. Rayleigh scattering is the most predominant linear scattering mechanism in optical fibres which has a λ^{-4} dependence. Guided modes in optical fibres and derivation of mode parameters are presented. Coupled mode theory has been derived for a system of two evanescently coupled waveguides. The variation of power in two evanescently coupled waveguides is depends on the propagation constants of the waveguide modes. Finally, this Chapter introduced the PL to the reader. Fibre-PL tapering process and the dependence on taper angle on mode loss is explained. Light propagation through a PL was explained by considering the simplest example of a tapered SMF. The relation between mode coupling loss and the taper angle is explained. The loss due to mode mismatch and non-adiabatic transitions in the PL have been outlined.

Chapter 4

Multiplexed single-mode wavelength-to-time mapping of multimode light

4.1 Introduction

Optical fibres are a crucial component for a wide range of photonic applications. SMFs do not suffer from either inter-modal dispersion or inter-modal coupling, and therefore normally preferred over MMFs in application such as conventional telecommunications and fibre-optic imaging. MMFs on the other hand, enable efficient collection of light and offers the potential for increased data carrying capacity by utilizing space division multiplexing in advanced telecommunication systems. The group velocity dispersion (GVD) in the fibre can induce linear-WTM, which is the basis of time-stretch spectroscopy. A light-weight Raman spectrometer has recently been realised using SMF which allows the acquisition of hyperspectral Raman signal, making use of WTM in conjunction with TCSPC. Using advanced single photon detectors, the Raman peaks were collected at the output of the SMF in time domain [25]. The method can be applicable for most of the spectroscopic systems which suffers from excessive energy consumption and heavy weight. For example, in space-based applications and Mars/moon rovers, where the mechanical stability and heavy weight of the detection system forbids the application of conventional CCD based Raman spectrometer.

However, the use of one single pixel detector limits WTM-based Raman spectroscopy as higher acquisition time needed to build and resolve the Raman peaks. Also, the low signal collection efficiency of SMFs makes the detection system vulnerable to extreme environmental situations such as mechanical vibrations which is problematic. The use of MMFs in real-time Raman spectroscopy suffers low temporal resolution and long length of fibre is needed to get sufficient spectral resolution [30]. One solution to overcome these issues is to use an array of single photon detectors for multiplexed detection and

a PL for efficient collection and WTM of Raman signal. Megaframe 32 is a detector consisting of 32×32 square array of Si-SPAD pixels with individual TDC for TCSPC. The transmission and processing benefits of SMFs and the collection efficiency of MMFs can be achieved using a PL (see Section 3.3). As outlined before, the multimode end of the PL enables the efficient collection of multimode states of light and the single-mode cores ensures the single-mode confinement and transmission of optical signal. This experimental chapter discusses various experiments performed towards the development of a WTM system for multiplexed single-mode WTM of multimode states of light using a MCF-PL and the Megaframe 32 detector.

4.1.1 Wavelength-to-time mapping

WTM occurs when a wave packet of light propagates along a sufficient length of dispersive medium. Light pulse can be considered as a set of pulses with different central wavelengths travels with slightly different group velocities.

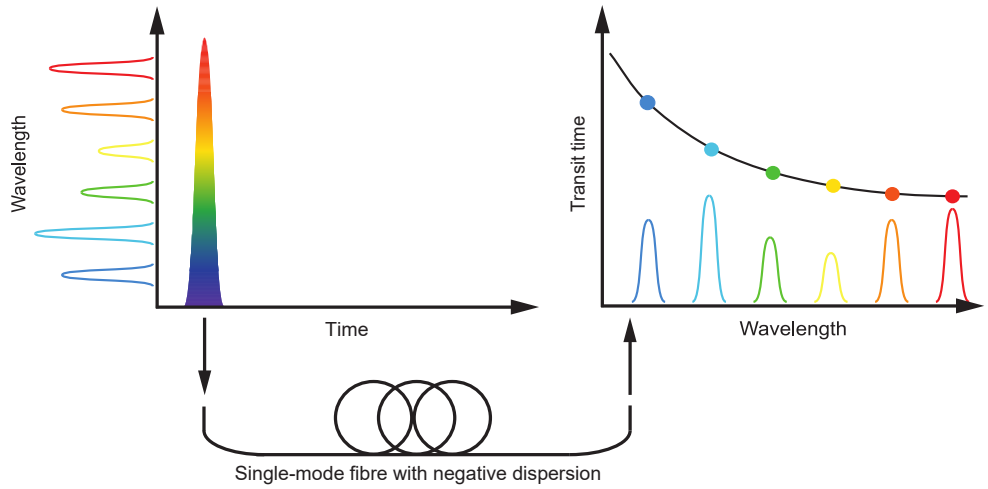

Figure 4.1: A schematic representation of WTM in fibre optics. A broadband pulse is coupled into a long length of SMF (on the left side of the figure). The chromatic dispersion in the fibre results the wavelength components being mapped into arrival time (on the right side of the figure). This figure is adapted from [23].

Figure 4.1 is a pictorial representation of WTM in fibre optics. In an optical fibre, GVD enables linear-WTM, where different wavelength components in the pulse travels at different time along the fibre. When a broadband pulse is coupled at the input of a sufficiently long length of fibre, the wavelength components will emerging out at the output of the fibre at different time. Thus the wavelengths can be mapped into arrival time at the output.

The major contribution in WTM in SMFs is the chromatic dispersion of the fibre. The temporal duration (Δt) of two pulses with central wavelengths (λ_1 and λ_2) is given by,

$$\Delta t = \int_{\lambda_1}^{\lambda_2} LD(\lambda) d\lambda \tag{4.1}$$

where L is the length of the single-mode fibre and D is the GVD of the fibre.

4.2 Experimental details

This Section describes the experiments performed towards the development of a multiplexed single-mode WTM instrument. Characterisation of a MCF-PL and multiplexed single-mode WTM of multimode states of light are explained.

4.2.1 Multicore fibre-photonic lantern

A MCF-PL used to build the multiplexed single-mode WTM instrument is detailed in this Subsection. A 290 m long 11×11 square array MCF which was attached to a PL was used in the experiment. The MCF was developed by Dr. Itandehui Gris-Sánchez and Prof. Tim A. Birks at the Centre for Photonics and Photonic Materials, University of Bath. The fibre was made up of germanium doped silica cores with a diameter of $\approx$ 1.63 μm. To fabricate the PL, the MCF was threaded into low refractive index fluorine doped silica capillary. By surface tension, this capillary was then collapsed on the top of the MCF by oxybutane flame. The structure was then softened by the flame and tapered forming a bioconical-fibre like structure. The multimode end of the PL was then revealed by cleaving the centre of the tapered waist. After tapering, multimode core of the fibre is $\approx$ 35 μm in diameter with a transition length of $\approx$ 4 cm. The core-core separation and the mode field diameter of cores were accurately measured and presented as follows. Figure 4.2 (a & c) presents a microscope image of 11×11 array of single mode cores and the multimode end of the PL respectively. Fig. (b & d) presents false colour images of the single-mode core end when coupling light at 532 nm at the multimode end and the multimode profile when coupling 532 nm light to a single core at the single-mode end respectively. Based on Equation 3.33, the multimode end of the PL supports 585 modes at 500 nm and 406 modes at 600 nm.

Before conducting any WTM measurements, the MCF-PL was characterized in detail. The following Subsections discusses the experiments performed towards the characterisation the MCF-PL.

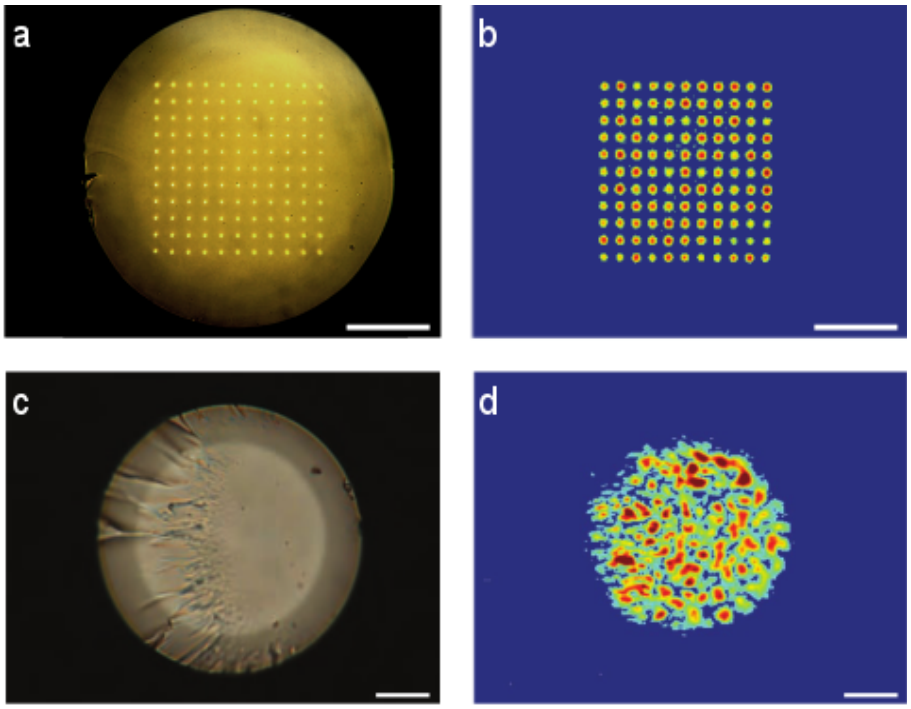

Figure 4.2: MCF-PL used in the experiment. (a) Microscope image of the 11×11 square array of SMF end. Scale bar, 50 μm (also in b). (b) False colour image of the single-mode end when illuminating the multimode end of the lantern with 532 nm light. (c) Multimode end of the PL. Scale bar, 10 μm (also in d). (d) False colour image of the multimode end when exciting a single core at the single-mode end with 532 nm light.

MCF core-to-core cross coupling

An initial characterisation of the MCF was performed to measure the core-to-core cross coupling. The cross coupling or cross talk is an important parameter in MCF based telecommunication and imaging. The cross talk between fibre cores can result in low data transmission capacity in space division multiplexing [101] and low detection performance in fibre based optical imaging [102, 103]. It was observed that cross talk increases with increase in wavelength according to coupled mode theory (see Section 3.2.3). The mean value of the statistical distribution of the crosstalk in a homogeneous MCFs is given by [104],

$$XT_{avg} = 2\,\frac{\kappa^2 R}{\beta\,\Lambda}\,L \tag{4.2}$$

where κ is the mode-coupling coefficient between neighbouring cores, R is the bending

radius, β is the propagation constant, Λ is the core-to-core separation and L is the length of the fibre. The cross talk in homogeneous MCFs can be easily estimated if the mode coupling coefficient κ is obtained.

An experiment was performed to investigate the cross talk between the cores of the 11×11 MCF. The cross coupling of signal in the fibre cores results in the overlap of signals between the cores which will lead to the temporal broadening of signals as the MCF cores has slightly different propagation constant values. A supercontinuum (SC) laser (Fianium supercontinuum SC400-6) was used as the source to investigate the cross coupling. A monochromator was used to select spectrally narrow pulses of light at different central wavelengths from the broad SC. The filtered light was then coupled onto one end of a SMF (SM600) and mounting the other end on a sub-micrometer precision *x*-*y*-*z* microstage. The SM600 fibre was then butt-coupled to a 300 m long MCF and different cores were selected by translating the SM600 fibre along *x*-*y*-*z* directions with high precision.

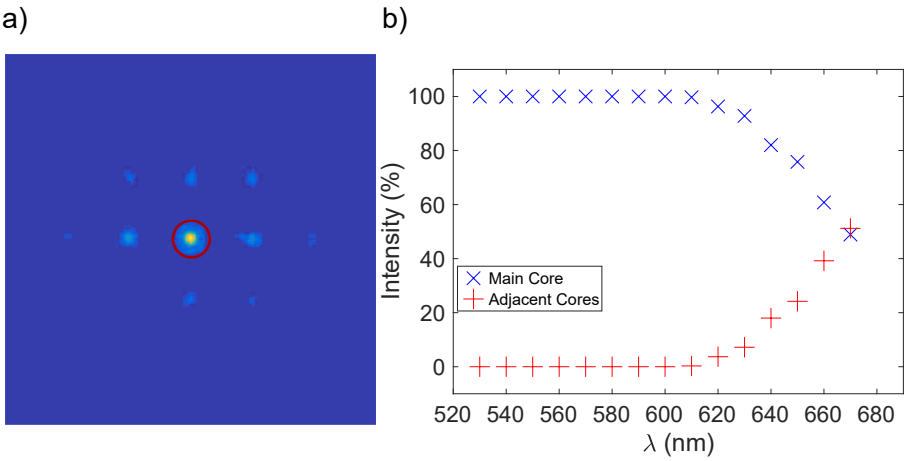

Figure 4.3: Cross coupling measurement of the MCF cores. (a) False CCD image for light transmission through the excited core and adjacent cores recorded at 650 nm light. (b) Intensity as the function of wavelength for the centre core.

A CMOS camera (Thorlabs DCC1645C) was used to image the output end of the MCF and the distribution of light at the MCF output was recorded for different central wavelengths within the 520-680 nm spectral region. For each wavelength, the FWHM of the passbands were measured using a conventional spectrometer (Ocean Optics USB2000+). The FWHM of the passbands were measured to be $\approx$ 3 nm for all the measurement wavelengths. From the camera images, the intensity of the light at the excited core and the adjacent cores are measured. A background correction was performed to remove the offset signal caused by camera's dark current.

Figure 4.3 (a) presents a CMOS camera image of the output intensity distribution of MCF cores when coupling light at λ = 650 nm to the central core. The intensity of light at the centre core and the adjacent cores for different wavelengths were then measured and Fig. 4.3 (b) presents intensity as a function of wavelength within the 520-680 nm spectral region. From the cross coupling measurements, it was observed that there is no significant cross-coupling between the cores below 620 nm. This indicates that the MCF cores can provide both spatial and temporal resolution for the WTM experiments below 620 nm.

MCF core positions

The core-to-core separation (pitch) in a MCF is an important parameter in designing fibres for telecommunication and imaging applications. From Equation 4.2, it is clear that, core-to-core separation effects the cross talk in an MCF which introduces signal scrambling at the fibre output. For an ideal square array MCF, the spatial arrangements of the MCF cores will be periodic with equal core-to-core separations. This ideal case cannot be achieved due to fabrication tolerances during the fibre drawing process, and the spatial arrangements of MCF cores will always deviate from a perfect square grid. To measure the MCF core positions precisely, one end of the MCF was flooded with white light while attaching the other end in a set of computer controllable nm-precision *x*-*y*-*z* Aerotech stages. The output of the MCF was then imaged with sufficiently high magnification onto a CCD camera. The relative positions of the MCF cores was then measured by translating the stages with nm-precision and monitoring different core mode positions on the camera. Figure 4.4 show the histograms of core-core separations in both horizontal and vertical axes of the MCF. The counts in y-axis represents the core number.

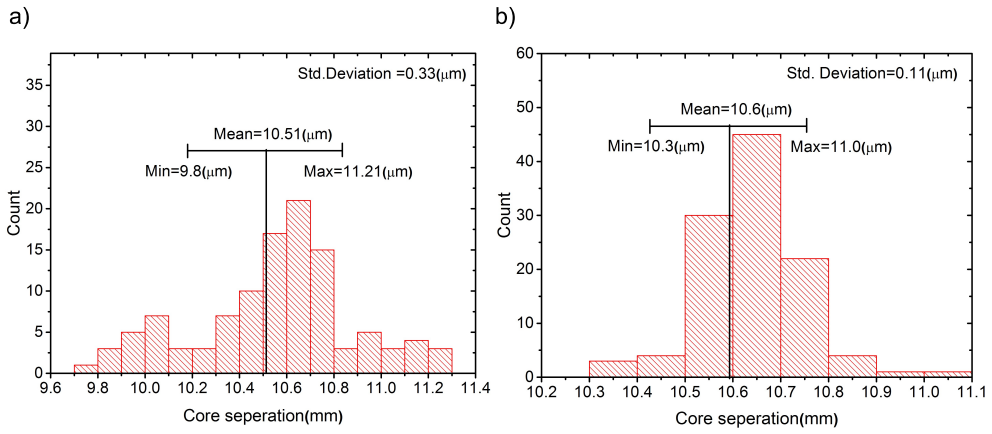

Figure 4.4: Histograms of core-core spacing in horizontal (a) and vertical (b) directions.

A computer simulation was then performed to investigate the deviation of the MCF core positions from a perfect square grid. An 11×11 perfect square grid was fitted to the measured MCF core positions by adjusting the rotation and dilation of the grid by keeping the central grid point on the central MCF core position. The root mean square (RMS) displacement between the grid and MCF core positions were measured and the parameters were optimised to minimize the RMS displacement between the grid and the MCF cores. The minimum RMS displacement of 0.54 μm was obtained for a grid spacing of 10.53 μm. The variations in the core pitches can results in an uneven distribution of cross talk across an MCF [105]. Similar type of core pitch measurements were reported for fibre bundle type MCFs. However, the fibre fabrication methods and fabrication parameters are different for various fibre drawing systems. A pitch variation of $\pm$ 0.4 μm was reported across a 19 core MCF [106]. This indicates that high standard fibre drawing system is required to fabricate MCFs with perfectly periodic core-to-core separation.

MCF mode field diameter

The mode field diameter (MFD) of the MCF cores were measured using calibrated near field imaging. A supercontinuum laser (SuperK EXTREME EXW-12 NKT photonics) was used as the source. One end of the MCF was mounted on a computer controllable nm-precision *x*-*y*-*z* translation stage. Light at central wavelength 550 nm from the laser was selected using an Acousto-Optic Tunable Filter (AOTF) and focussed onto each core of the MCF. The output of the MCF was then imaged on a CCD camera and the imaging system was calibrated using a US air force resolution test target. Light was coupled onto individual cores of the MCF by translating the *x*-*y*-*z* stages and the $1/e^2$ MFD of each MCF core was measured across the MCF. The MCF cores exhibit a $1/e^2$ MFD of 1.83 μm $\pm$ 0.04 μm in one axis and 1.85 μm $\pm$ 0.05 μm on the other. The uncertainties are the standard deviations (s.d) of the measured MFDs of the MCF cores. The repeatability and error in the MFD measurement were tested by defocusing re-imaging the central core mode and the error was found to be $\approx$ 2 $\%$ in both axes. The measured values are in good agreement with the theoretically evaluated MFD value of 1.93 μm from the fibre design [107].

To investigate how the MFD of the MCF cores varies with wavelength, a second set of measurement was performed over the 480 nm to 620 nm wavelength region for the central core of the MCF. Light at different central wavelengths were selected from the AOTF and coupled onto the centre core of the MCF. The MFDs were then measured from the well calibrated images from the CCD camera. Figure 4.5 (a) presents a false colour image of

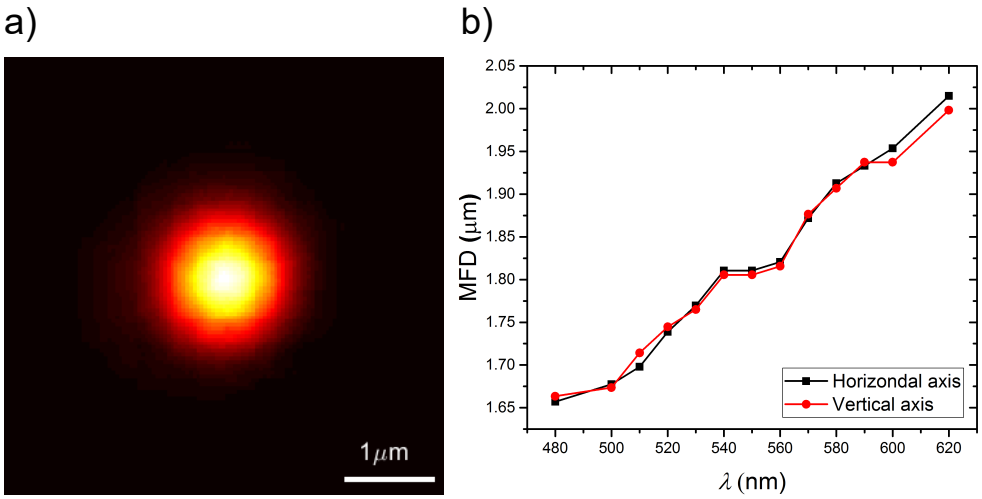

Figure 4.5: MFD of the MCF core modes at λ = 550 nm. (a) False colour image of the central core mode when coupling light at 550 nm. (b) Measured MFD as a function of wavelength for the central core of the MCF.

central core mode recorded at a wavelength, λ = 550 nm and Fig. 4.5 (b) represents the MFD as a function of wavelength for the central core.

The major source of uncertainty in MFD measurements of a step index fibre are the non-circularity of the fibre mode, non-linearity in measurement electronics, angular errors, and scattered light in the apparatus [108]. MFD measurements of fibre modes is crucial in characterising fibre splice loss. The conventional far-field pattern and variable aperture methods can be used to accurately measure MFDs of higher order modes in a fibre [109].

MCF propagation loss

The core specific propagation losses in the fibre was measured using fibre cutback method. Initially, one end of the fibre is perfectly cleaved and mounted on a nm-precision computer controllable *x*-*y*-*z* translation stages. Light at 550 nm from the supercontinuum laser (SuperK EXTREME EXW-12 NKT photonics) was selected using an AOTF and coupled onto each core of a 119.5 m long MCF using a high NA lens. The power of light emerges out from the selected core after the 119.5 m long MCF was then measured using a power meter (Thorlabs S121C). By translating the stages, light was coupled into individual cores across the MCF at the input end and the power values after each cores were noted. The accuracy and repeatability of the coupling can be controlled with $\approx$ 1 nm precision. The fibre was then removed from the output and the experiment was then repeated for 89.5 m, 10 m, and 0.97 m lengths of MCF, keeping the input fibre mounted on the translation stage. For each core, the total insertion loss as a function of MCF length was plotted. The

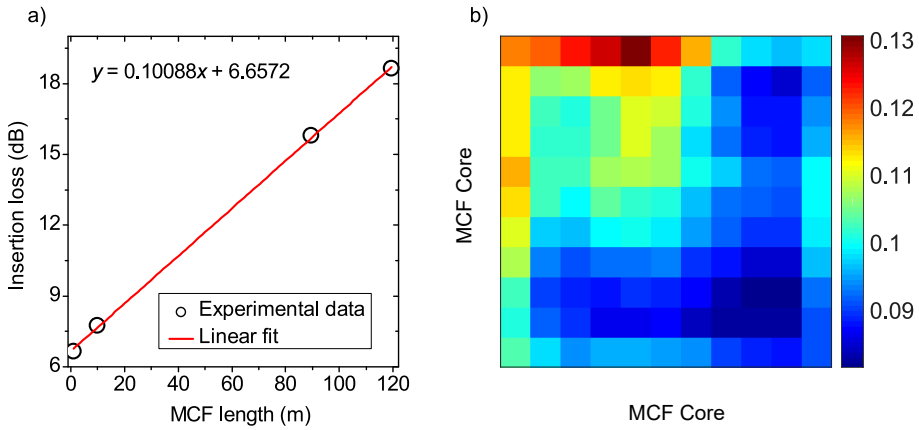

Figure 4.6: (a) Measured insertion loss as the function of MCF length for the central core of the MCF at λ = 550 nm. (b) A colour map of core specific insertion loss of the 11×11 square array MCF cores. Each square indicates a core in the MCF. The unit of colour bar is dBm^{-1}. This figure is adapted from [23].

results of the fibre cutback measurement are given in Fig. 4.6. Figure 4.6 (a) represents the cutback measurement data and the fit for the central core. The fit to the data was found to be linear with an extremely good r^2 value of 0.999554 and a residual sum of squares 0.0324 dB^2 indicating that the measurement was performed with high precision and accuracy. From the gradient of fit, the central core exhibits a loss of 0.1 dBm^{-1}. Similarly, the loss for all 121 MCF cores were calculated from the gradient of the fits from the four experimentally evaluated points. Figure 4.6 (b) shows a colour map of loss values for the 121 cores measured from the cut back measurements. Each square in the attenuation matrix represents a core and the unit of colour map is in dBm^{-1}. To check how the variation in the input alignment affects the accuracy of the measurement, the coupling was misaligned and optimal coupling was re-achieved with 0.5 $\%$ variations of the output power. This indicates that any change in the input MCF alignment has negligible impact on power measurement.

Most of the research in fibre attenuation has been focussed on the communication wavelengths from 1400 to 1600 nm. However, the experimentally measured propagation loss value is higher compared to previously reported loss values from literatures [110, 111]. The reason could be fabrication related as impurity levels in fibre may vary for different fabrication set ups. At the visible region, Rayleigh scattering is the dominant source of loss in optical fibres. In germanium doped fibres, the density fluctuation of GeO_2 can contribute to higher scattering losses compared to pure silica fibres.

Photonic lantern numerical aperture

The numerical aperture of the multimode end of the PL was measured using near field imaging technique. A PL which was attached to a 20 m long fibre was used in the experiment. The multimode end of the lantern was mounted on a computer controllable nm-precision *x*-*y*-*z* translation stage. Light at 550 nm was selected from the supercontinuum laser using an AOTF and flood illuminated the single mode end of the MCF. A CCD camera (Thorlabs DCC1545C) was held close to the multimode core and images were recorded for different multimode core positions by translating the stages in steps of 500 μm relative to the camera position.

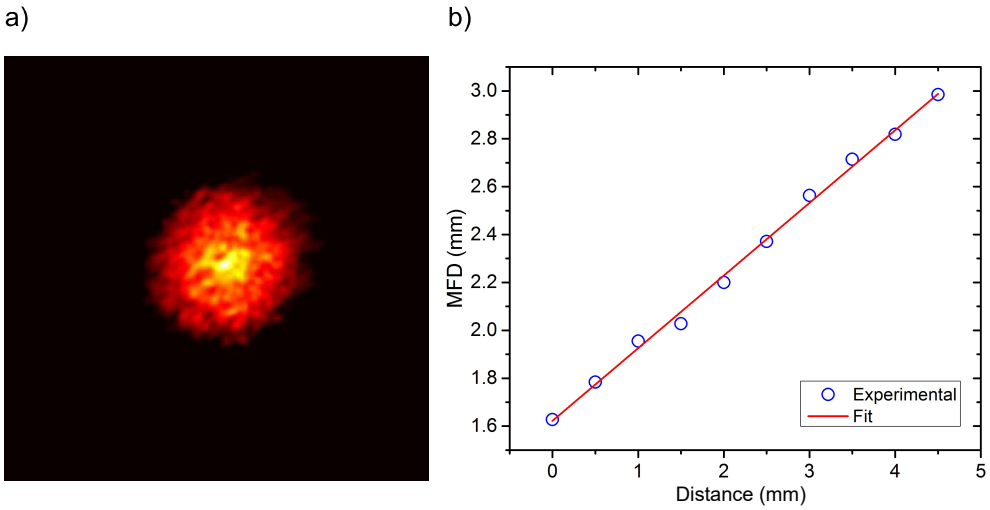

Figure 4.7: PL numerical aperture measurement. (a) False colour image of the multimode end of the PL when flood illuminating the single-mode end with 550 nm light. (b) MFD of the multimode end of PL as a function of transition length (circles) and the fit to the data (solid line).

As an example, Fig. 4.7 (a) presents a false colour image of the multimode end of the PL when flood illuminating the single-mode cores at the opposite end with 550 nm light.The $1/e^2$ MFD of the multimode end of the PL was then measured and plotted for each translation distances which is shown in Fig. 4.7 (b). The data follows a linear regression with an extremely good r^2 value of 0.99654. The NA of the multimode end of the PL was then measured from the gradient of the fit which was calculated to be 0.15. From the refractive index profile of the fibre and fluorine doped silica capillary, the theoretical value of NA was measured to be 0.22. The reason for this mismatch in NA for the theory and the experiment is that not all the higher order modes are excited at the multimode end upon light injection. The NA value 0.22 can only be achieved when all the supporting

modes are excited at the multimode end. It was observed that, from Equation 3.33, the number of modes excited at the multimode end is 225 for a light injection NA of 0.15.

Photonic lantern insertion loss

The loss experienced by the multimode end of the PL when coupling light to the single mode end of the MCF was measured. As discussed in Section 4.2.1, the cutback method was used to investigate the core specific PL transmission loss. A 20 m long MCF which was attached to the PL was used for the measurement. The single-mode end of the MCF was mounted on a computer controllable *x*-*y*-*z* nm-precision translation stage and light at 550 nm was coupled on the MCF cores. The output end contains the multimode end of the PL. By translating the stages, light was coupled to individual cores and for each core, the power of light emerges out from the PL was recorded. The loss experienced by the multimode end of the PL for each core was then measured by comparing the loss expected from the 20 m of MCF alone. The propagation loss values for the 20 m fibre was predicted from Section 4.2.1. Using this technique, the PL multimode end transmission loss was calculated to be 0.19 dB, with a standard deviation of 0.34 dB.

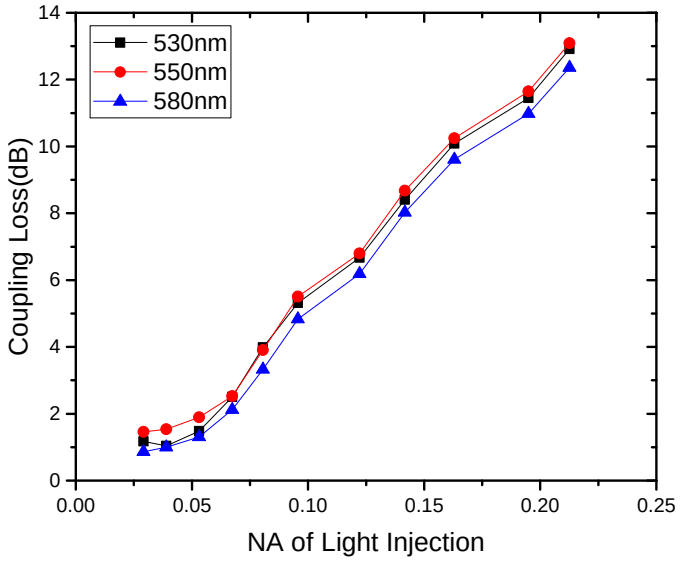

Figure 4.8: Coupling loss of the multimode mode end of the PL measured for three different central wavelengths as a function of NA of light injection.

A second method was used to investigate the loss experienced by the PL for different NA of light injection. Light at central wavelength 550 nm was selected, collimated, and projected to a lens through a variable iris. The light was then coupled onto the multimode end of the PL which was attached to a 20 m long MCF. The NA of the coupling light to the

multimode end of the PL can be changed by changing the aperture size of the variable iris. The diameter of the circular beam for each light injection was precisely measured using a digital vernier callipers. The coupling loss in the multimode end of the PL as a function of NA of light injection was then calculated. The contribution of MCF propagation loss and Fresnel reflections from the PL ends were taken into account. To investigate how the loss varies across the 500-600 nm spectral region, the experiment was repeated for two more wavelengths at 530 nm and 580 nm. Figure 4.8 presents the plot for coupling loss as a function of NA of light injection to the multimode end of the lantern. A minimum coupling loss value of $\approx$ 1.2 dB was obtained for an injecting light with NA = 0.03 at λ = 530 nm. This value is still $\approx$ 1 dB higher compared to the value measured using the above discussed method. The reason for this higher value is the loss induced due to mode mismatch at the multimode end. In a perfectly adiabatic situation, only 121 lowest order modes in the multimode end of PL can couple to the 121 single mode cores. As the NA increases, the higher order modes in the PL excites more and cannot be coupled into the single mode cores due to mode mismatch. In reality, the low loss condition can only be achieved when the spatial profile of input coupling spot matches perfectly with the spatial mode profile supported by the multimode end of the PL.

The dependence of NA of light injection on throughput of the PL was previously investigated and found to be similar compared to the experimental results presented [112, 113]. However, most of the research on photonic lanterns are mainly focussing on near infra-red wavelength region where the brightest OH lines present.

4.3 WTM - experimental details

The experimental layout for the multiplexed WTM instrument is given in Fig. 4.9. A femtosecond laser (Fianium HE-1060-1 μJ-fs) operating at 500 kHz and emission wavelength 1064 nm was used as the source. As the Megaframe works in the reversed START-STOP TCSPC mode, the set-up consists of two arms. Here, the signal from a 290 m long MCF-PL starts the TCSPC measurement and the periodic trigger signal from the laser source stops the measurement. The optical signal for the TCSPC measurement was generated from a PCF. By pumping a 20 cm long PCF with femtosecond pulses using lens L1 ($f = 8$ mm), broad SC spectrum was generated spanning from 400 nm to 1 μm. The spectrum from the PCF was then collimated using lens L2 ($f = 30$ mm).

The wavelength region for WTM was selected using the band pass (BP1), short pass (SP) and long pass (LP) filters. This allows a spectral region of 500 nm to 600 nm for the

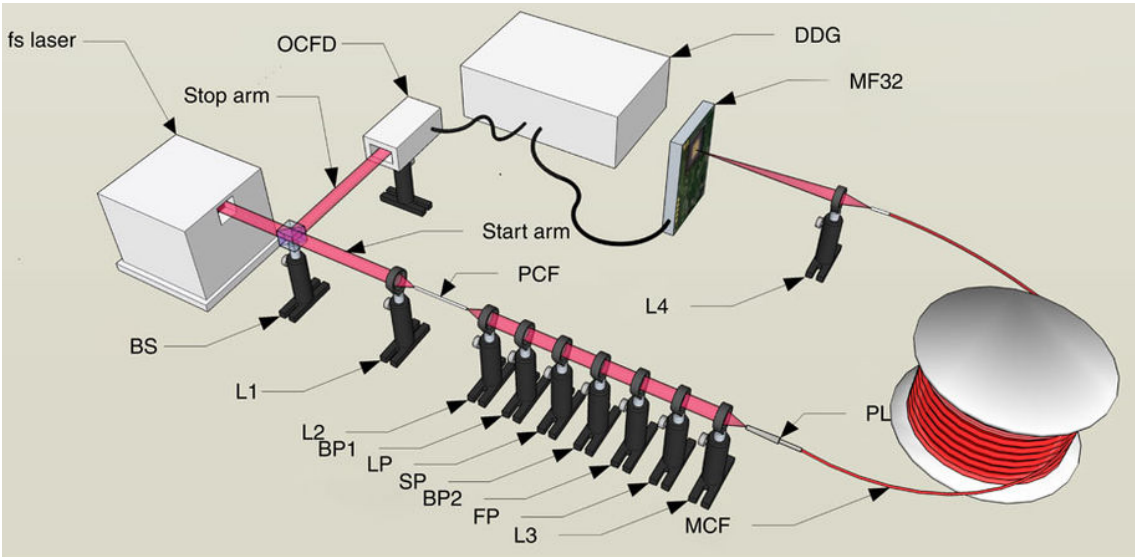

Figure 4.9: Experimental set up used for multiplexed wavelength-to-time mapping. This figure is adapted from [23].

TCSPC measurements. For the calibration of the WTM measurements, a Fabry-Pérot (FP) filter (developed by Edinburgh Biosciences and Delta Optical Thin Films) was introduced in the beam path in combination with bandpass filters to generate narrow passbands of light. The 8^{th} order FP filter was designed for a wavelength, λ = 550 nm. The narrow pulses of light were then coupled to the multimode end of the PL using lens L3 ($f = 8$ mm). At the output, the 121 single-mode cores of the fibre was then imaged on 11×11 array subset of pixels on the Megaframe using an achromatic lens L4 ($f = 30$ mm). The lens L4 was chosen in such a way that the single-mode MCF cores could be efficiently mapped to individual SPADs at the Megaframe. For each measurement, the central wavelength of the reference spectrum was recorded using a conventional spectrometer (Ocean Optics USB2000+ spectrometer). The arrival time of photons for the passbands within the 500 nm to 600 nm spectral region was then recorded for each core-SPAD combination at the Megaframe.

For the stop-arm, a portion of the laser was tapped onto an optical constant fraction discriminator (OCF). The OCF generates stable electrical pulse for each periodic pump pulse which stops the TCSPC measurement. The triggering is based on zero cross point of the electrical pulse which is explained in Section 2.3. The 290 m length MCF introduced a time delay of 1.33 μs for the start signal. To match this delay, a digital delay generator (DDG- Stanford Research Systems) was used which delays the electrical signal from the OCF electronically. With a resolution of 5 ps, the 8-channel delay generator can delay electronic signals from 0 to a maximum of 2000 seconds.

4.3.1 Calibration of wavelength-to-time mapping

Initially, the WTM system was calibrated over the 500 nm to 600 nm spectral region. For this, spectrally narrow pulses of light was selected from the SC by inserting bandpass (BP2) and FP filters. The central wavelength and the band width of light after the bandpass filter was controlled by angle tuning the FP filter. The reference spectrum recorded with the conventional spectrometer for each passbands are given in Fig. 4.10. The filtered light was then coupled onto the multimode end of the PL. Due to the different propagation constant values of the cores, the arrival time of photons for each passbands varies across the MCF. As an example, Figure 4.11 (a) shows the difference in arrival time of photons in the mapped SPADs at a wavelength, λ = 531 nm. The maximum difference in arrival time was calculated to be $\approx$ 1.7 ns. The black square in the colormap indicates the hot pixels across the 11×11 subset of mapped pixels. These pixels are excluded from the data processing as they possesses high noise levels compared to other pixels. The experiment was then repeated for different central wavelengths across the 500 nm to 600 nm spectral region.

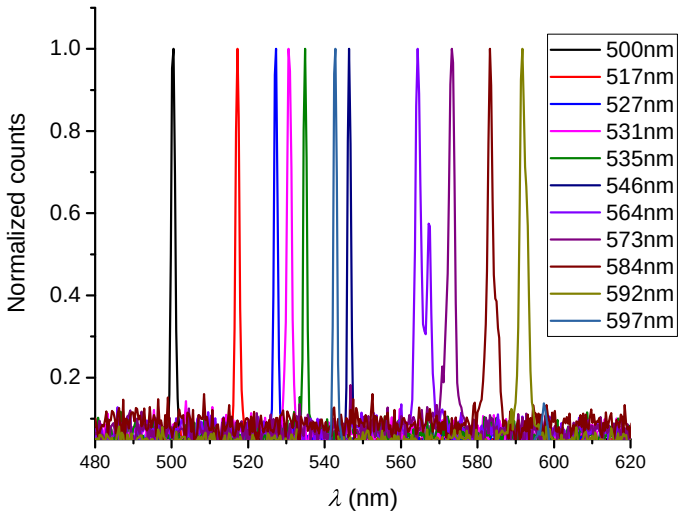

Figure 4.10: Reference spectra for the calibration of the WTM instrument recorded with a commercial spectrometer.

The arrival times of photons for different wavelengths was then calculated for each core-SPAD combinations. The recorded arrival times fitted well with the fourth order polynomial and the equation of these fits was used to convert the arrival time into wavelengths as a calibration for the WTM. Figure 4.11 (b) shows the recorded and the fitted arrival times for the central core, the core with lowest and fastest group velocities.

The core specific dispersion in the MCF was also calculated from the arrival time of photons at the Megaframe. As an example, Fig. 4.12 (a) presents the arrival time of photons

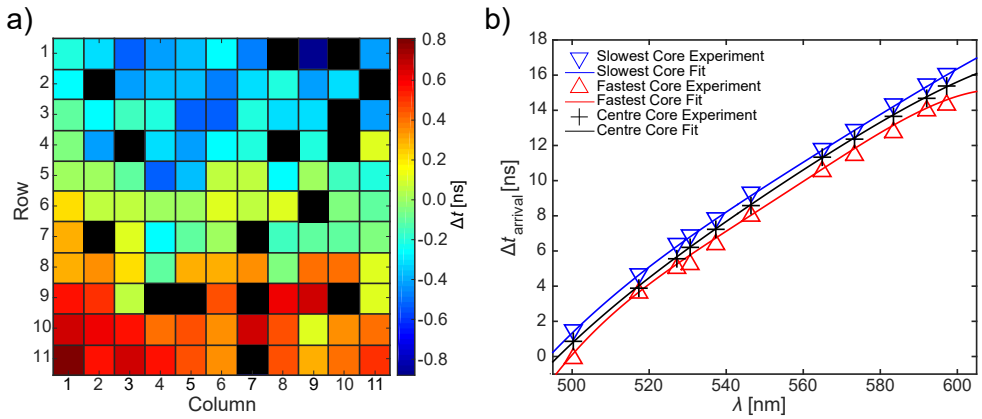

Figure 4.11: (a) Difference in arrival time for each core at the 11×11 square array of MCF measured at λ = 531 nm. Black square indicates a hot pixel. (b) Measured (symbols) and fitted (solid lines) wavelength-dependent arrival times for the central core and the cores with fastest and slowest group velocities. This figure is adapted from [23].

for different central wavelengths and the 4^{th} degree polynomial fits to the data for the central core. The dispersion of the central core was then calculated from the derivative of the fit. Figure 4.12 (b) shows the typical dispersion curve for the central core of the MCF as a function of wavelength across the 510-590 nm spectral region. Similarly, dispersion values of all mapped MCF cores were calculated from the arrival time of photons at each pixel. The dispersion varies across the MCF cores which indicates that the resolution of the WTM spectra across the MCF cores will vary according to Equation 4.1. The dispersion across the MCF cores at 550 nm was measured to be 500.34 $\pm$ 30.86 ps nm^{-1} km^{-1}.

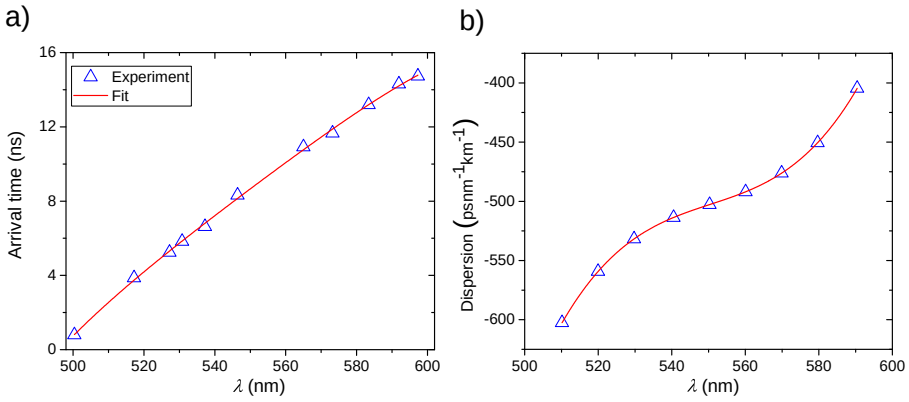

Figure 4.12: (a) Wavelength-dependent arrival time of photons for the central core and the fits to the data. (b) Dispersion in the central core of the MCF measured from (a).

To investigate the spectral resolution of the WTM instrument, a spectrally narrow pulse of light at around 550 nm was selected by angle tuning the FP filter. The FWHM of

the passband was measured to be 0.5 nm using a commercial spectrometer with 0.1 nm resolution. The light was then coupled onto the multimode end of the PL and the time-resolved spectrum for the central core was recorded. The FWHM of the WTM spectrum was found to be 1.2 nm FWHM. The resolution of the WTM spectrum was then obtained by convolving the filter passband with a Gaussian profile of increasing width until the FWHM of the convolved passband matched with the 1.2 nm FWHM of the WTM spectrum. This was achieved at a Gaussian FWHM value of 0.96 nm which is the approximate line-width of the WTM spectrum obtained from the central core. The theoretical value of spectral resolution was then calculated from Equation 4.1.

From Fig. 4.11 (b), the dispersion of the central core at 550 nm was measured to be $\approx$ 505.9 ps nm^{-1} km^{-1}. Substituting this value in Equation 4.1, the separation between two pulses should be 1.02 nm if they are to be well resolved at the Megaframe. This value is very close to 0.96 nm that we obtained from the FP filter measurement which gives an indication that the WTM instrument operating in-line with the theory.

The spectral resolution across the entire wavelength range can be easily calculated from Equation 4.1. The resolution of the WTM spectra depends on the wavelength, and increases for shorter wavelengths as the chromatic dispersion in the MCF increases. For the central core, the dispersion was measured to be as -621.6 ps nm^{-1} km^{-1} at 510 nm and -417.8 ps nm^{-1} km^{-1} at 590 nm. Based on these dispersion values, we expect the resolution of the WTM spectrum ranging from 0.8 nm to 1.2 nm according to Equation 4.1. The final spectrum from the WTM instrument can be obtained by adding all the WTM spectra from each core pixel combinations. In that case, the spectral resolution of the final spectum at any specific wavelength can be achieved by summing all the line-functions from the cores of the MCF.

4.3.2 Broadband wavelength-to-time mapping

After careful calibration of the WTM system, WTM was performed over a broad range of wavelengths. For the wavelength selection, the BP2 and FP filters were removed and the SC was spectrally narrowed within the 500 nm to 600 nm spectral region using SP, LP and BP1 filters. The filtered light was then coupled directly onto the multimode end of the PL, keeping the output imaging system unchanged. As the result of wavelength dependent coupling in the multimode end of the PL, it was observed that each MCF core exhibits very different spectra. To show the impact of this on photon counts in pixels, Fig. 4.13 (a) presents summed counts in each pixel at the Meagaframe with spectrum in three representative pixels (b). There is a clear variation of total counts across the 11×11

subset of pixels and as discussed in Section 4.2.1, the reason for this is the variation in the core specific propagation losses in the MCF. In an ideal situation, the MCF cores would

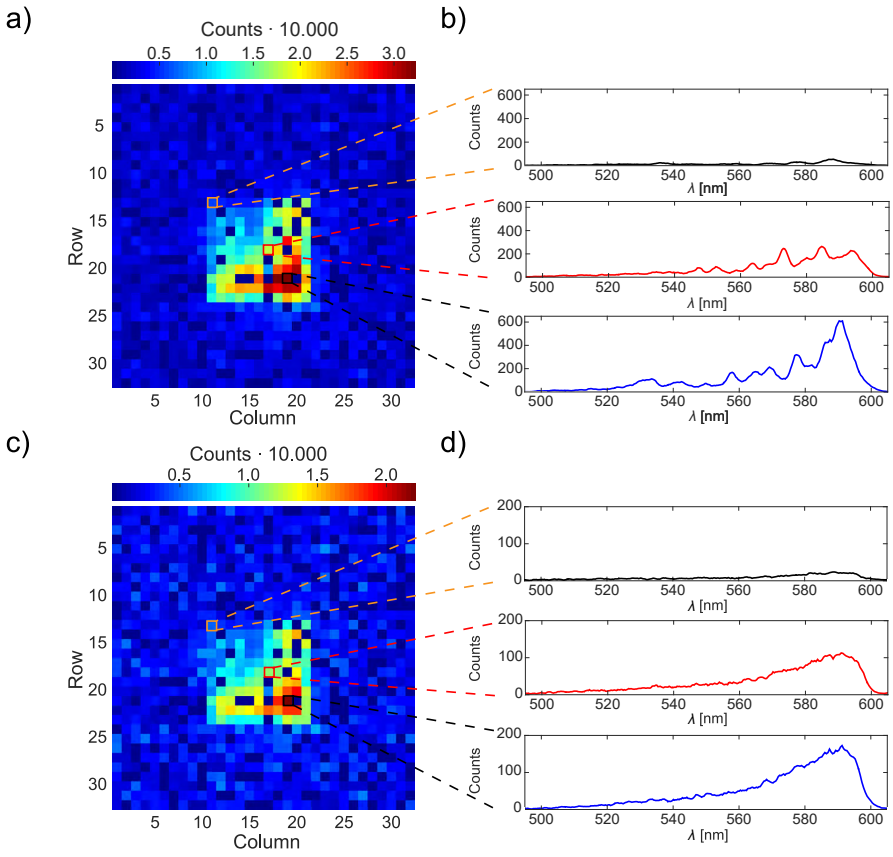

Figure 4.13: Summed counts in each pixel of the Megaframe without the rotating diffuser plate (a) with the WTM spectra of three representative pixels (b), summed counts in each pixel of the Megaframe with the rotating diffuser plate (c) with the same three representative pixels (d) given in b. This figure is adapted from [23].

have same propagation losses and the cores should exhibits same coupling efficiency to SPADs and the total counts across the 11×11 subset of pixels would have uniform intensity distribution. This situation is not achieved as there are some loss of information in the final spectrum due to the wavelength-dependent coupling at the multimode end. To investigate how this wavelength-dependent coupling and loss impacted on the final WTM spectrum, a second set of measurements were performed by placing a rotating diffuser plate directly in front of the multimode end of the lantern. The diffuser plate was used to remove the high intensity bright spots by spreading the light evenly across the surface. A stepper motor was used to rotate the diffuser at a rate of 20 Hz. By transforming the laser light into many scattered laser spots, the rotating diffuser plate ensures the even spreading of coupling light onto the multimode port. This enables excitation of all the modes in the

multimode end of the PL equally in a time averaged manner for all wavelengths. This time, the cores would produce same WTM spectra similar to the one if there are no loss of information due to wavelength dependent coupling since all wavelength couple into the lantern equally. Figure 4.13 (c) and (d) presents the summed counts in each pixel of the 11×11 subset of SPAD array with the spectra in the same three pixels presented in Fig. 4.13 (b) after introducing the rotating diffuser plate. In this case, since all the wavelengths are coupled onto the PL equally, the time-resolved spectrum from all the mapped pixels should exhibit similar spectrum. It is clear that with the rotating diffuser plate, all the MCF cores exhibits similar WTM spectra. However, due to the reflection from the input surface of the diffuser plate, the intensity of light after the diffuser plate reduces significantly. This is more evident in the TCSPC measurement (Fig. 4.13 c) as the photon counts reduces drastically.

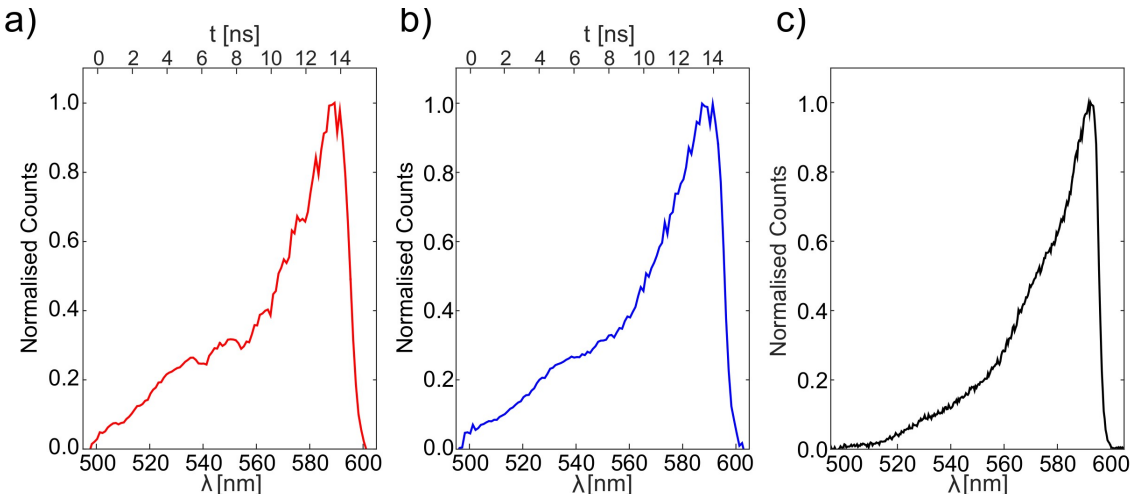

Figure 4.14: (a) Final summed spectra obtained after adding all the spectra from the illuminated pixels at the Megaframe with (a) and without (b) the rotating diffuser plate, and the reference spectrum recorded with a conventional spectrometer (c). This figure is adapted from [23].

The final WTM spectra from the instrument without and with the rotating diffuser plate was obtained by adding all the individual WTM spectra from the mapped 11×11 subset of pixels. Figure 4.14 (a) presents the normalised final WTM spectra without the diffuser plate and Fig.4.14 (b) presents the normalised spectra with the diffuser plate. Figure 4.14 (c) presents a reference spectrum recorded with the conventional spectrometer. Both the WTM spectra match well with the reference spectrum except there are some loss of information in the spectrum recorded without the rotating diffuser plate. The reason for this is the loss introduced by the wavelength-dependent coupling at the multimode end of

the PL. There is a clear increase of counts in the WTM spectra towards the shorter wavelength region compared to the reference spectrum. This is likely due to the wavelength-dependent MFD of the MCF cores (see Section 4.2.1) in which the shorter wavelengths are confined more tightly to the SPAD active area compared to the longer wavelengths. Also, as given in Section 2.4, the photon detection probability of the Megaframe SPADs varies significantly by $\approx \pm$ 15 $\%$ to the mean within the 500-600 nm region. For the future applications these effects needs to be taken into consideration. Clearly, a SNR of 10 was achieved with the demonstrated WTM system which is a significant improvement compared to other existing single pixel WTM systems.

Fill factor enhancement

The mapping of 121 MCF single-mode cores to 121 SPADs will effectively increase the fill factor of a subset of SPADs in the Megaframe. To measure this fill factor enhancement, light at 532 nm was coupled onto the multimode end of the PL which was attached to a 9 m long MCF. A single-mode core at the output was selected and mapped to a single pixel at the Megaframe. Different magnifications of the single core mode was selected ranging from 1.4 to 5.1 and the counts for each magnification was recorded at the SPAD pixel for a set time. For the magnification 1.4, it is reasonable to assume that the light from the mode with a $1/e^2$ MFD of 1.84 μm falls inside the SPAD active area of $\approx$ 6 μm. The total counts for a set time in the pixel was then recorded for this magnification. This would be the maximum achievable counts for the core-pixel combination with 100 $\%$ coupling efficiency. To couple 121 MCF cores with a core-core spacing 10.53 μm to 121 SPADs with each separated by 50 μm, the MCF core spacing should be magnified by M = 4.75. This value matches one particular measured M value (M = 4.7) to within experimental error. By comparing the counts with a magnification of M = 1.4 and M = 4.7, a single core-SPAD efficiency of 64 $\%$ is achieved which is a significant improvement over the SPADs fill factor of 1 $\%$.

The diameter of the SPAD's active area was evaluated by considering the fibre mode as a circular aperture of diameter 1.85 μm dilated by a magnification of 4.75. By considering the SPAD's active area as a circular aperture, the fraction of the beam passing through the active area was calculated for different magnifications and fitted to the data using a χ^2 fitting procedure. The best fit was achieved for a radius 3.15 μm which matches with the $\approx$ 6 μm SPAD diameter reported. Figure 4.15 (a) show the efficiency of a single core-SPAD pair as a function of magnification of the core mode at 532 nm.

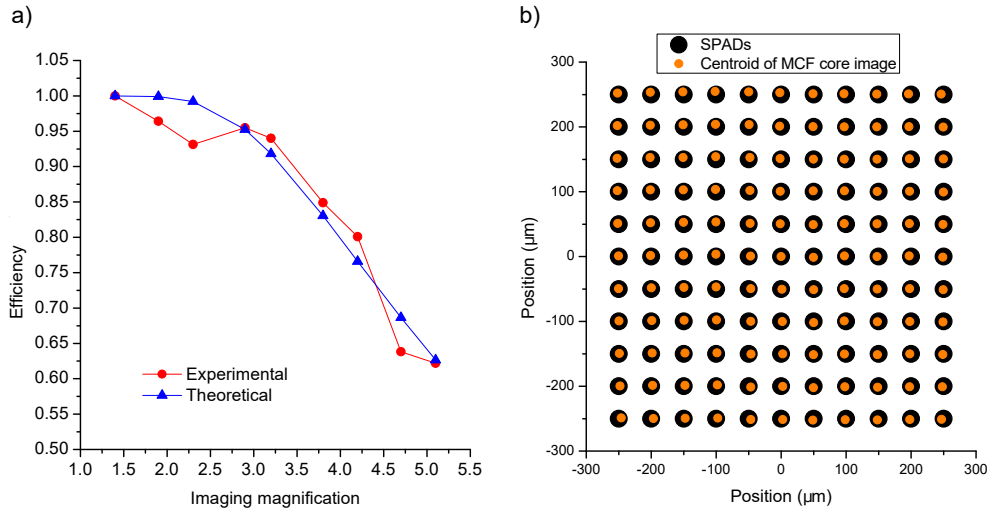

Figure 4.15: (a) Coupling efficiency of a single core-SPAD pair as the function of magnification. Efficiency 1 indicates the maximum counts achieved when the light falls completely within the active area of the pixel. (b) A representation of how the MCF cores could be images on a perfect square array of SPADs for optimum coupling condition. The sizes of the cores and SPADs are not representing the actual sizes. This figure is adapted from [23].

To calculate the overall efficiency of coupling with 121 MCF cores being mapped to 121 SPADs, a computer simulation was performed. Clearly, an overall efficiency of 64 % can only be achieved if the MCF cores are spatially oriented in a perfect square grid. Since this is not the case for the MCF, the method described in Section 4.2.1 was used to calculate the over all core-SPAD coupling efficiency. The measured RMS displacement of the cores in the MCF, 0.54 μm, dilates to 2.54 μm for a magnification of 4.75. The impact of this mismatch on overall cores-SPADs coupling was evaluated by calculating the fraction of circular Gaussian beam passing through a circular aperture with 121 mode-SPAD lateral offsets. An average overall efficiency of 45.8 % was achieved using this technique. This value is an underestimation of the efficiency we achieved in the experiment since we are not considering the translation of MCF matrix with respect to the central grid point. Figure 4.15 (b) is a visual representation of MCF cores being mapped onto the perfect square array of SPADs in the optimum coupling condition. In the future applications, the SNR of the WTM instrument can be greatly improved by fabricating a MCF with more number of single-modes with periodic core-core spacing.

4.4 Chapter summary

This Chapter discussed in detail about the experiments performed towards the development of a multiplexed single-mode WTM instrument. A MCF-PL was introduced for the efficient collection and reformatting of multimode states of light into an array of 121 SPADs on a single photon sensitive detector array. The MCF was characterized in-terms of cross coupling between cores, MCF-core positions, MFD of the MCF cores, core specific propagation loss, and the dispersion in the MCF cores. From the cross coupling measurements, it was observed that the MCF cores are ideal for the WTM measurements in the 500 nm to 600 nm spectral region. The coupling was found to be negligible below 620 nm. This indicates that the MCF can provide the spatial resolution required for the time-resolved imaging. The variation of the MCF core positions from an ideal square structure was investigated. A computer simulation was performed to investigate the variation of the measured core-core separations with a perfectly square grid. A minimum RMS value of 0.54 μm was obtained between the measured core separations and the grid for a grid spacing of 10.53 μm. In future, with state-of-the-art fabrication systems, it is possible to fabricate MCFs with perfectly square structure. The MFD of the MCF cores were measured using calibrated near field imaging. The MCF cores exhibit a $1/e^2$ MFD of 1.83 μm $\pm$ 0.04 μm in one axis and 1.85 μm $\pm$ 0.05 μm on the other. The core specific propagation loss was calculated from fibre cut back method. From the measurements, the central core exhibits a propagation loss of ≈ 0.1 dBm^{-1}. The NA of the multimode end of the PL was measured from near field imaging and measured to be 0.15 at 550 nm. An insertion loss of $\approx$ 1.2 dB was obtained for an injecting light with NA = 0.03 at λ = 530 nm. The WTM of multimode states of light was then performed making use of the TCSPC capability of the Megaframe. Using custom imaging syatem, the 121 core modes in the MCF was mapped onto 121 SPADs on the Megaframe. The WTM was well calibrated over a spectral range of 500 nm to 600 nm. From the arrival time of photons at the SPADs and fitting the data with the 4^{th} order polynomial, the calibration equations were derived across the wavelength region. The core specific dispersion across the 500 nm to 600 nm was calculated from the differentials of the calibration equations. The dispersion across the MCF cores at 550 nm was measured to be 500.34 $\pm$ 30.86 ps nm^{-1} km^{-1}. By Mapping MCF cores to SPADs, an effective fill factor of 46 % was achieved which is a significant improvement compared to the 1 % fill factor of SPADs itself. By carefully optimising the MCF-PL parameters during fabrication and with custom imaging systems, it is possible to achieve near 100 % optical fill factor enhancement in core-SPAD mapping.

Chapter 5

Quasi real-time imaging and wavelength-to-time mapping of spatial modes in a few-mode fibre

5.1 Introduction

Optical fibres have been extensively used in applications such as optical telecommunication [114–120], fibre-based sensing [121–123], fluorescence-spectroscopy [124–126], and quantum optics [127–129]. Optical fibres offer as an efficient tool for optical time-stretch, a process based on WTM [23, 25] (see Section 4.1.1). Utilising WTM in SMF is relatively simple as there is only one mode (with two orthogonal polarisations) propagating along the fibre. Light in MMFs can travel in different modes depending upon the launching conditions and fibre parameters. The different group velocities of the propagating modes results the modes arriving at different time at the fibre output. This difference in time-of-flight between various mode groups is described by differential mode delay (DMD). Providing there is no crosstalk between modes in the fibre, signals can propagate in each mode along the length of the fibre without reducing the bandwidth-length product for optical telecommunication. This method which utilises each mode as a separate channel to carry information is known as mode division multiplexing (MDM). Recent development in MDM for long-haul optical transmission systems utilises MMFs, which are mainly focussed on multiple-input and multiple-output (MIMO) digital signal processing [130–132].

A recent demonstration in optical time-stretch spectroscopy showed that higher order modes could also be excited and utilised offering more degrees of freedom for optimising and designing fibres for time-stretch imaging applications [133]. For the time-stretch imaging based on MMF and FMF, an accurate and reliable method is needed for the GVD and the DMD measurements. Current dispersion measurement techniques to characterise MMFs makes use of interferometry and the information can be extracted from the spectral

fringes caused by the inter-modal interference [134]. Conventional time-domain DMD measurements uses steak cameras or fast detectors to extract propagation speed between modes in conjunction with fast sampling oscilloscope. Imaging of the spatial modes using CCD cameras can only provide spatial information about the modes. Addressing these issues, a direct space-time imaging of propagating modes in a FMF was performed with the Megaframe, at the same time enabling the WTM of the modes within a desired wavelength region. This technique can be used to characterise FMFs and MMFs without the requirement of any complicated calibration of the instrument. This experimental demonstration will open a new route towards time-stretch imaging and WTM applications by utilising higher order modes.

5.2 Experimental details

This Section describes different experiments performed towards the quasi real-time imaging and WTM of spatial modes emerging out from a few mode fibre using Megaframe.

A standard, commercially available SMF was used in our experiment (Corning SMF-28). The fibre was designed to be single mode at λ = 1310 nm which has a core diameter of $\approx$ 8.2 μm with NA 0.14. Before performing any WTM measurements, the refractive index profile of the fibre was measured using an index profiler (IFA-100 Fiber Index Profiler) by Mrs. Dionne Haynes at the Leibniz-Institut für Astrophysik Potsdam, Germany. The numerical calculations were performed based on the refractive index profile of the fibre. Figure 5.1 shows a micrograph of SMF-28 and the measured refractive index contrast between the core and the cladding along fibre axis.

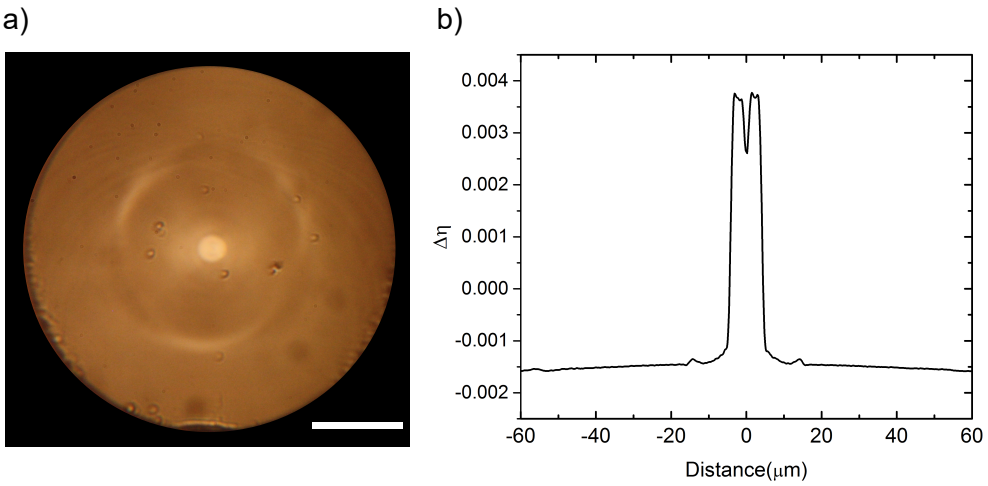

Figure 5.1: a) Micrograph of SMF-28. Scale bar, 30 μm. b) Measured refractive index profile of the core and the cladding.

The wavelength region in our measurements was carefully chosen so that the fibre supports a few modes for time-resolved imaging. All our measurements were restricted within the wavelength region of 500 nm to 610 nm. In this region, the fibre supports a maximum of six LP modes. The experimental set up for light-in-flight multimode imaging is given in Figure 5.2. The set-up consists of two different arms for the TCSPC measurement. Here, the signal from the fibre (start-arm) starts the TCSPC timer and the periodic trigger signal from the laser stops the TCSPC measurement (stop-arm).

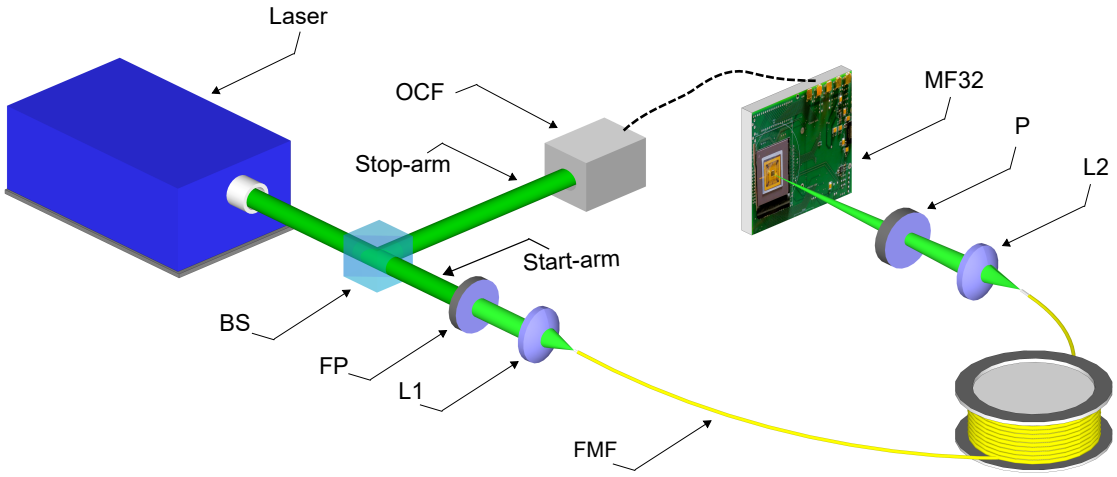

Figure 5.2: Experimental set-up for light-in-flight multimode imaging system.

In the start-arm, spectrally narrow pulses of light were selected from the supercontinuum laser operating at 19.5 MHz repetition rate using an AOTF in combination with the angle-tunable FP filter. The central wavelengths of the narrow passbands after the FP filter was measured using a conventional spectrometer (QEPro Ocean Optics Inc.). The filtered light was then focussed onto a 981.5 m long SMF-28 fibre using lens L1 ($f = 8$ mm) which excites the spatial modes in the fibre. By carefully optimising the input coupling, six LP modes were observed in the fibre when exciting with 532 nm of light. Excitation of the modes is dependent on the input coupling conditions as the relative intensity between the modes changes significantly for different regions in the fibre core. By moving the fibre facet on an *x*-*y*-*z* micro flexure stage, an overfilled condition was achieved which excites all the LP modes in the fibre. It was observed that the mode pattern changes significantly for different launching conditions in the fibre.

The length of the fibre was accurately measured using an Optical Time Domain Reflectometer (OTDR). This length was chosen in order to obtain sufficient modal dispersion in the fibre. At the output, the mode profile of the fibre was imaged onto the Megaframe using lens, L2 ($f = 4.51$ mm). In order to reduce the ambiguity in mode images due

to the degenerative modes, a polariser (P) was placed after lens L2 and the polarisation direction was set same as the input coupling light. To investigate the output mode profile of the SMF, a small portion of the output light was directed onto a CCD camera using a beam-splitter. Both the Megaframe and the CCD camera were placed on the focal plane of L2.

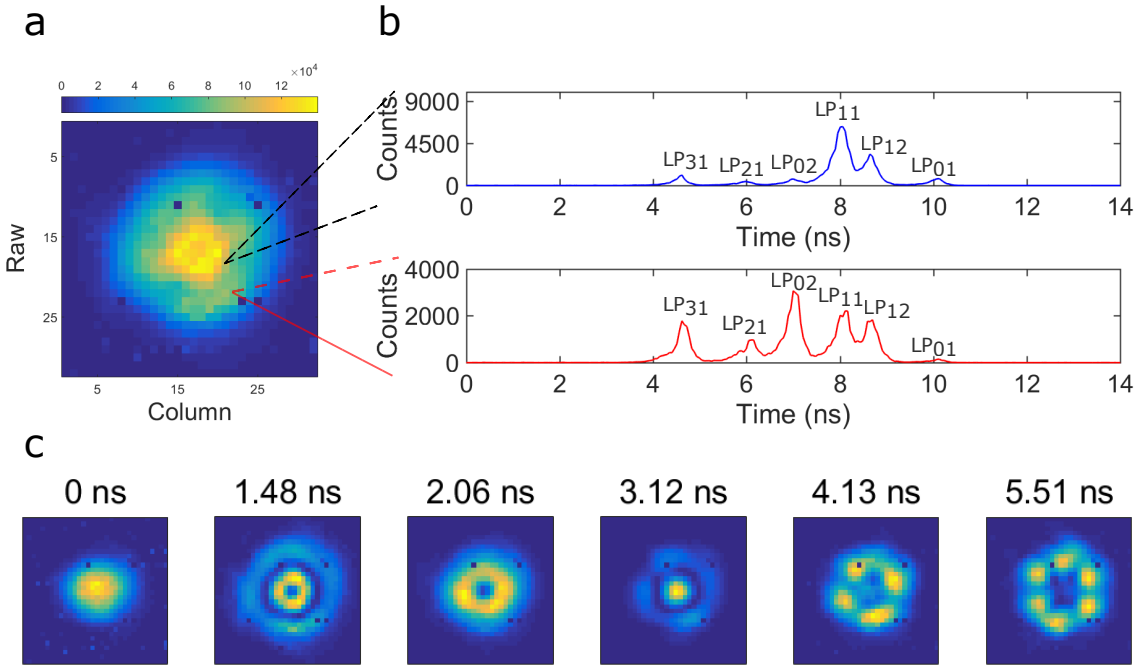

Figure 5.3: Recorded modes on the Megaframe with two representative pixels when coupling 532 nm light. a) Summed counts in each pixels at the Megaframe integrated over the laser pulse period for a set time. b) Two representative pixels with the relative intensity of different spatial modes. c) Time evolution of the modes with peak arrival times. The observed modes are, LP_{01} , LP_{12}, LP_{11}, LP_{02}, LP_{21} and LP_{31}. Note that a higher value in x-axis indicates smaller propagation time for the modes along the fibre.

In the stop-arm for TCSPC measurement, a portion of the light from the laser was tapped using a beam-splitter and coupled onto the OCF. The OCF provides a stable electrical pulse to the MF32 which stops the TCSPC measurement for each laser pulse. Due to the variation in the time delay of the stop signal, the IRFs of SPADs are aligned non-uniformly in time with a standard deviation of $\pm$ 440 ps. This shift was taken into account and corrected during the post processing of the data. Due to the CMOS fabrication intolerances, almost 2 $\%$ of the pixels possesses high noise levels which are removed from the data processing. Different peaks were observed at the Megaframe and the peaks represents the spatial modes in the fibre. As an example, Figure 5.3 (a) shows the summed counts in each pixel at the Megaframe for the entire laser pulse period (51 ns) with two representative pixels (b) showing the spatial modes for a narrow pass band of light at central

wavelength, λ = 532 nm integrated over a set time. The well resolved peaks at the two pixels represents six spatial modes supported by the fibre. The passband of the coupled light was measured to be $\approx$ 1nm FWHM. Due to chromatic dispersion in the fibre, the recorded impulse response of the fibre for each mode at the Megaframe spans a FWHM of $\approx$ 550 ps. Since Megaframe works in reverse START-STOP TCSPC mode, a longer value in the time axis represents shorter propagation time along the fibre. At 532nm, the LP_{01} mode propagates faster and arrives at the Megaframe first followed by LP_{12}, LP_{11}, LP_{02}, LP_{21}, and LP_{31}. This indicates that the group indices of the modes are higher for the successive modes. Figure 5.3 (c) presents the time evolution of the fibre modes recorded at the Megaframe. The title of each time frame represents the peak arrival time of the modes.

The time difference between slowest (LP31) and fastest mode (LP01) (maximal excursion) in differential group delay is $\approx$ 5.5 ns. The maximum achievable temporal resolution of our imaging system is determined by the length of the fibre and the timing jitter of Megaframe (contribution from both laser jitter and electronics).

5.2.1 Calibration of WTM of spatial modes

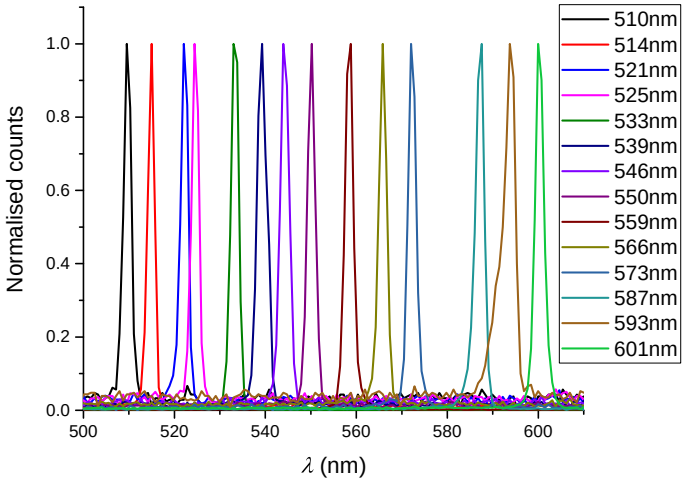

Figure 5.4: Reference spectrum for WTM of spatial modes recorded with a conventional spectrometer

To calibrate the WTM of spatial modes, different central wavelengths were selected using the AOTF and the FP filter. The central wavelengths of the narrow passbands were measured using the conventional spectrometer. Figure 5.4 presents the measured reference spectrum with different central wavelengths. The FWHM of the passbands were set to be

$<$ 2 nm using the FP filter in order to avoid the broadening of the signal at the Megaframe due to chromatic dispersion.

The wavelength-dependent arrival times of photons at different central wavelengths of different spatial modes were then obtained for 500 nm to 610 nm spectral region. The peak arrival time of the wavelengths for different spatial modes were then recorded at a single pixel on the Megaframe. Figure 5.5 (a) represents the measured (marked) and the fitted (solid lines) arrival times for five spatial modes recorded on a single pixel at the Megaframe.

The measured arrival time of photons fitted well with the fourth order polynomial. The equations of these fits can be used to convert the arrival time into wavelength within the selected spectral region.

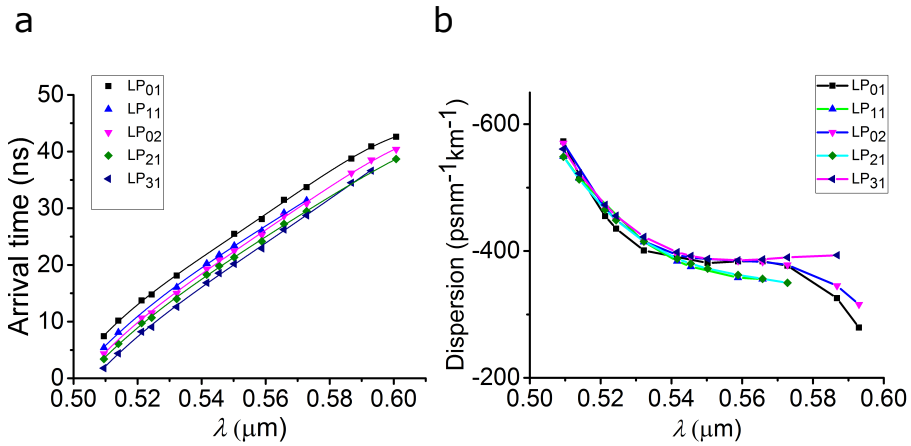

Figure 5.5: Calibration of wavelength-to-time mapping of spatial modes. a) Arrival times of photons at the Megaframe (marked) and fitted (Solid line) for five spatial modes. b) Measured chromatic dispersion from the gradient of the fit.

From the gradient of the fit, the chromatic dispersion of five modes were calculated and given in Fig. 5.5 (b). In all the measurements, the number of photons per pulse was $<$ 0.01 which ensures that the measurements were performed in the single photon regime to avoid pulse pile-up.

5.2.2 Relative modal delay

From the wavelength-dependent arrival time of photons in different spatial modes, the relative modal delay between different mode groups were measured with respect to the fundamental mode. The theoretical values were calculated from the scalar wave equations

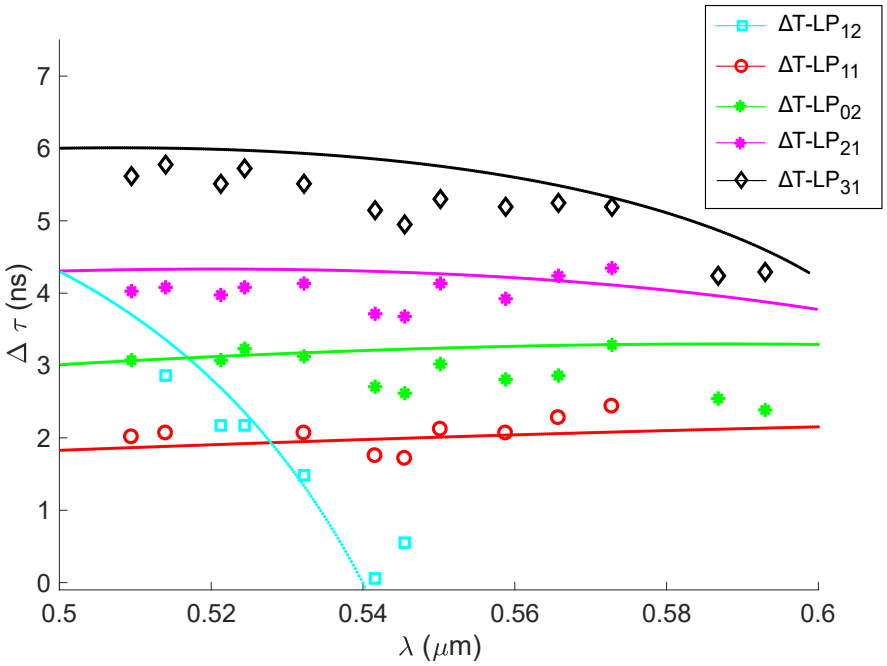

Figure 5.6: Theoretical (solid lines) and experimental (marked) relative modal delay between different mode groups with respect to the LP_{01} mode.

of a fibre with radial index profile. Based on the refractive index profile, Figure 5.6 presents the theoretical and the experimentally observed modal delay values. The small mismatch in the theoretical and experimental values are likely due to the stress induced effects as the fibre was wrapped in a fibre wheel. This effect is more evident for the LP_{31} mode as the mode electric field distribution is concentrated more towards the outer region of the core. The solid lines represents the theoretical modal delay difference of different modes with respect to LP_{01} mode as a function of wavelength. The marked points are the experimentally observed data points. There is a discrepancy in LP_{12} mode due to the cut-off wavelength around 550 nm and the behaviour of the mode is highly dependent on environmental and stress related changes in the fibre parameters.

This real-time monitoring of modes can be used to find the effective refractive index difference ($\Delta\eta_{eff}$) between the closest mode groups. The measured effective refractive index differences are in the order of 10^{-4} which is comparable with the values offered by the existing interferometric and phase shift techniques.

To compare the presented technique with other DMD characterisation approaches currently used, Table 5.1 lists the comparison between the Megaframe and some of the common approaches with basic features. Here, the comparison is focussed on the temporal resolution of the detection system. The temporal resolution in time or frequency domain

is defined as the maximum value among the FWHM of the waveforms in the DMD profile. The values given in the table is taken from the literatures [135–138] may vary for different systems as the resolution is dependent on the sampling detector and the light source.

Method	**Resolution (ps m^{-1})**	**Features**
Optical frequency domain reflectometry	0.058	Calibration required, no imaging capability
Mach-Zehnder interferometry	0.09	Calibration required, short length of fibre, no imaging capability
Frequency domain phase shift	0.013	Calibration required, high accuracy, short length of fibre, no imaging capability
Optical time domain reflectometry	0.088	Calibration required, low noise, high interference contrast, no imaging capability
Megaframe 32	0.56	No need of calibration, long length of fibre required, imaging capability, single photon sensitivity

Table 5.1: Comparison of DMD measurements using Megaframe and other common approaches.

The imaging technique presented here is of great interest in FMF telecommunication applications and 3D imaging. With Geiger mode APD based on InP/InGaAs(P) pixels, it is possible to extend the imaging technique to telecommunication wavelengths such as 1310 nm and 1550 nm. High performance multipixel single photon detectors are commercially available offering higher sensitivity and lower dark count rates at the telecommunication wavelengths [139]. Similar to Megaframe architecture, these detectors are integrated using CMOS technology and interfaced using FPGA. The detector offers time-of-flight measurements of each pixels with a frame rate of $\approx$ 185 KHz for 32$\times$32 pixel sensor and $\approx$ 115 KHz for 128$\times$32 pixel sensor. The challenges in FMF telecommunication for MDM including DMD and crosstalk due to cross coupling between modes can be easily addressed by combining the presented technique and Geiger mode APDs. In fibre based 3D imaging, this technique can improve the imaging capability by utilising higher order modes offering more signal to noise ratio.

5.3 Chapter summary

To summarise, making use of the TCSPC capability of the Megaframe, quasi real-time imaging and WTM of different spatial modes in a FMF is realised. A commercially available SMF was used as a FMF by choosing a shorter wavelength region. First, light at 532 nm was selected using a combination of an AOTF and FP filter and coupled onto the SMF. At this wavelength, the fibre supports 6 LP modes and all the modes were excited using an overfilled condition at the fibre input. The output profile of the fibre was imaged onto the Megaframe and the real-time imaging of spatial modes was performed. Six peaks with varying amplitudes were observed at the Megaframe pixels, each representing different spatial modes. Due to the chromatic dispersion in the fibre, the FWHM of each LP mode spans $\approx$ 550 ps at the Megaframe. Narrow passbands of light within 500-600 nm region was then selected using a combination of an AOTF and FP filter. The central wavelength of each signals were recorded using a commercial spectrometer. To reduce the chromatic dispersion and the broadening of signal at the pixels, the FWHM of the passbands were restricted to < 2 nm by angle tuning the FP filter. The wavelength-dependent arrival time of photons in spatial modes were then recorded at the Megaframe. The measured arrival times across the wavelength region fits well with the fourth order polynomial. The chromatic dispersion of modes were calculated from the derivative of the fit. The differential mode delay of the modes with respect to the fundamental mode were also measured with picosecond timing accuracy. The experimental values matches well with the theoretical values across the wavelength region. The proposed method can also be used to calculate the effective refractive index difference between the closest mode groups in the order of 10^{-4} which is comparable with the current interferometric techniques. This experimental demonstration on time-resolved imaging of spatial modes will find applications in areas such as time-stretch spectroscopy, MDM, and real-time soliton imaging.

Chapter 6

Time-resolved discrete imaging in photonic lattices using state-recycling

6.1 Introduction

The propagation of light in lattices of coupled waveguides is analogous to electrons travelling in semiconductor crystals. The spatial refractive index distribution of the periodic photonic structure enables the discretised hopping of light inside the waveguide structures and therefore plays an important role in scientific and fundamental research. In coupled waveguide arrays with discrete translational symmetry, the confinement and evolution of light is quantized. The phenomenon is known as discrete diffraction [140–142] were the electromagnetic wave is a discrete function of space and time. The first theoretical realisation of discrete diffraction was in 1965 by Jones [143] and later experimentally demonstrated on gallium arsenide arrays a few years later [144]. However, the diffraction pattern can be tailored upon introducing an inhomogeneity in the lattice. For example, one can localise the electromagnetic field inside the lattice by introducing an inhomogeneity in the lattice . Remarkably, the diffraction suppression in periodic lattices can lead to Bloch oscillations where the electromagnetic wave exhibits periodic oscillations in the lattice. Observed early this century, Bloch and Zener [26, 27] predicted that electrons in a perfect crystal exhibits oscillatory motion rather than uniform under the influence of a constant electric field. The existence of Bloch oscillations was first observed experimentally in semiconductor super lattices [145]. Optical waveguide systems offers the ability to visualise phenomenon such as Block oscillations with photons. Observing Bloch oscillations in periodic lattices can be achieved by several ways. One can introduce a linear variation in the effective refractive index profile of the waveguides and the photons behave same as that of electrons in a periodic crystal with constant electric field [146]. The period of Bloch oscillations depends on the ramp of the linear potential. The ramp in potential can also be realised using a temperature gradient across the lattice axes [147] or by synchronously curving the axes of the optical waveguides [148, 149].

One of the most widely accepted methods to fabricate low-loss photonic lattices in transparent dielectrics is ultrafast laser inscription (ULI), which involves tight focussing of fs-laser pulses in a small volume of the transparent material inducing nonlinear light matter interactions [150, 151] at the focus spot. ULI enables integration of compact 3D photonic structures for lab-on-a-chip applications with exceptional material flexibility [152–157]. ULI has already found applications in fabricating integrated photonic devices including Mach-Zehnder interferometer [158], directional couplers [159], micro-lens arrays [160], Bragg gratings [161], PL [162], and topological insulators [163]. The main disadvantage of the ULI is the length of the inscribed photonic structures. As the waveguide structures are inscribed by translating the dielectric material on high precision *x*-*y*-*z* stages, the maximum possible lattice length is determined by the translation limit of the stages. As we demonstrate here, one way to address this issue is to fabricate the waveguide structures on a small length of transparent material and coat the end facets of the sample with a highly reflecting material. By coating the end facets of the lattice, one can effectively increase the lattice length making use of multiple reflections at the facets. However, observing the diffraction phenomena in such lattices in space and time is challenging and time consuming. The major limitation in discrete imaging in guided-optics is the lack of novel detectors which can perform space-time (x-t) imaging. This limitation can be overcome with Megaframe in conjunction with TCSPC technique. By placing the lattice in a linear cavity and using each SPAD pixels as individual detector channels, direct time-resolved discrete imaging is demonstrated for the first time. With custom imaging technique, the evolution of light in the waveguide array was monitored in quasi real-time using the Megaframe SPAD pixels. The state-recycling technique [165] and demonstration on real-time imaging of discrete system will open new possibilities in direct observation of discrete phenomena in guided-optics.

6.2 Experimental details

The following Subsections deals with various experimental demonstrations involved in time-resolved discrete imaging in 1D lattices using state-recycling. The fabrication and preparation of the lattices and the state-recycling techniques are explained.

6.2.1 Fabrication of photonic lattices

This Section describes the fabrication of two different types of 1D lattices using ULI technique[1]. The refractive index distribution in the lattices was controlled using the slit-beam shaping method [152]. The material modification depends on parameters such as laser pulse energy, pulse duration, wavelength and polarisation, translation speed and the lens configuration. The fabrication parameters and lattice specifications are described below.

a). Slowly-driven 1D lattice

A set of periodically driven waveguide was fabricated on a 15 mm long borosilicate glass sample (Corning Eagle^{2000}). The waveguides were designed to be in slowly-driven regime. Slowly-driven periodic system indicates that the driving frequency is of the order of the coupling constant between the waveguides [163]. A pulsed femtosecond laser (350-fs pulses) operating at 500 kHz repetition rate at 1030 nm was used to inscribe the waveguides by translating the glass sample at a speed of 9mm/sec. The fabrication parameters were optimised to produce the waveguides by single scan and the waveguides were single-mode within the wavelength range 780-980 nm. The structure of two adjacent waveguides resembles that of a directional coupler where the strength of evanescent coupling between the waveguides entirely depends on the coupling constant and the lattice constant. Synchronously bent waveguides were fabricated to turn the bonds "ON" and "OFF" by coupling of light at the interaction region. A schematic of two such waveguides (WG1 and WG2) is given in Fig. 6.1. The translation speed and scanning parameters were set so that the waveguides are uncoupled initially with a maximum inter-waveguide separation (d_{max}) of 40 μm. By translating the waveguides in *x*-*y*-*z*, the inter-waveguide separation was then reduced synchronously forming a straight region where the separation is minimum (d_{min}).

At the interaction region (L_2), the waveguides will act as two straight waveguides in which the bond turns "ON" for the desired wavelengths. As the coupling constant is a function of wavelength [164], the strength of the evanescent coupling can be changed by tuning the wavelength of light injection. Light reaching at the interaction region will evanescently coupled between the waveguides for a particular wavelength. After the interaction region, the inter-waveguide separation is set in the reverse order. The magnitude of the coupling

[1]Fabrication was performed by Dr. Sebabrata Mukherjee

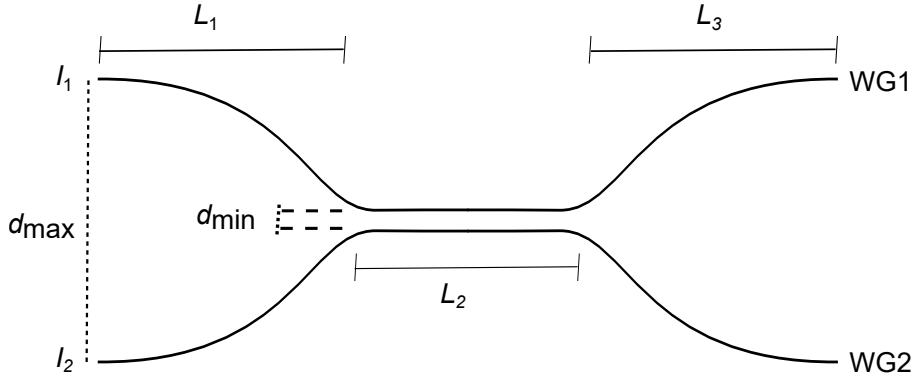

Figure 6.1: Schematic diagram of two synchronously bending waveguides, WG1 and WG2.

constant can be controlled by changing the waveguide separation and varying the wavelength of light injection. At the bending region (regions L_1 and L_3), the output intensities of WG1 and WG2 follows sine-squared function. The normalised output intensities in WG1 and WG2 when exciting WG1 is given by [163, 166],

$$I_1 = \cos^2(\phi); \quad I_2 = \sin^2(\phi) \tag{6.1}$$

$$where \quad \phi = \int_0^z k(z)dz \tag{6.2}$$

Twelve such units were fabricated on the sample. Each unit is a 50:50 directional coupler, see also [167]. Each waveguide in the directional coupler has a MFD of ≈ 8 μm.

b). Straight 1D lattice

To observe the discrete phenomena in straight coupled waveguide arrays, a second set of lattices were fabricated on a 30 mm long sample (Corning Eagle^{2000}) using the ULI. As given in Fig. 6.2 (a), the lattice consists of 1-D waveguide array with one waveguide per basis, $\Delta n(x+a) = \Delta n(x)$, where a is the lattice constant.

Twenty straight periodic waveguides were inscribed by translating the sample at a translation speed of 9mm/sec with single scan. The refractive index profile of the waveguides were controlled using slit beam shaping method as described above. The fabrication parameters were optimised so that the waveguides confines light only as the fundamental mode at 780-980 nm wavelength region. The inter-waveguide separation were set to be 19 μm with a MFD of ≈ 8 μm. Figure 6.2 (a) represents a schematic diagram of a finite

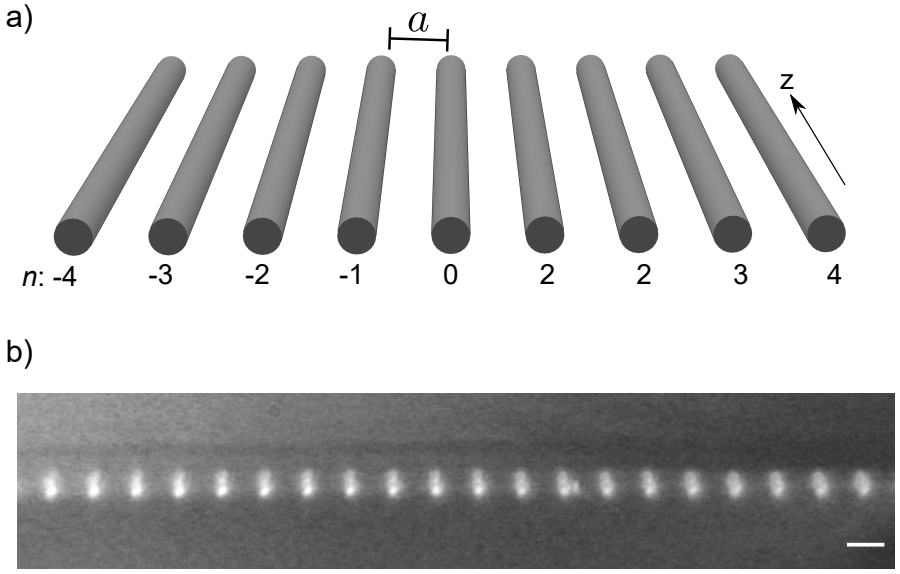

Figure 6.2: (a) Schematic diagram of the coupled waveguide array consisting of 9 straight waveguides. a is the lattice constant and z is the propagation direction of light. (b) A white-light micrograph of the fabricated array consists of 20 waveguides. Scale bar, 20 μm.

1D array with lattice constant a and propagation direction z. Figure 6.2 (b) shows a white-light transmission micrograph of the fabricated straight 1D lattices with twenty straight waveguides. Neglecting the small refractive index variations along the lattice due to laser power fluctuations, we assume that the waveguides are identical with same propagation constant and coupling constant values.

6.2.2 Photonic lattice - linear cavity preparation

First, the end facets of the two lattices were polished using a waveguide polishing machine. The facets were cleaned using acetone and coated with silver (99.99 % pure silver) using vacuum thermal evaporation technique (EDWARDS AUTO 306 vacuum chamber), forming a linear cavity. Initially, the coating reflectivity was characterised using an optical fibre circulator (Nortel Network HRC-1550-Q_3-1010). A continuous wave laser operating at 1550 nm was used as the source. A SMF (SMF-28) bare terminated at one end was held inside the coating chamber close to the sample as the test fibre. One port of the circulator was connected to the test fibre (SMF-28) and the other to an optical spectrum analyser (ADVANTEST Q8384). The Fresnel reflection from the bare fibre end was recorded and the power was noted in the optical spectrum analyser. Taking the initial power value as a reference, the power value was estimated for any desired reflection value from the fibre facet. The increase in power upon silver coating was then monitored in real-time using

the spectrum analyser. The coating was stopped at a desired power value at the spectrum analyser. This method provides control over coating reflectivity within an error $\pm$ 3 %. The source of this error is primarily due to the error in Fresnel reflection measurement induced by the imperfect cleaving of the fibre facet.

The reflections at the end facets were carefully chosen to minimise the cavity round trip loss. Reflectivity at the end facets is an important factor in photon counting measurement as it relates to the quality factor of the cavity. A smaller reflection value will lead to low quality factor as more light transmitted and hence lost after each cavity round trip. The reflectivity at the end facets of the slowly-driven lattice were measured to be $\approx$ 92 % and $\approx$ 90 % respectively at 780 nm. The cavity round trip loss at the coated end facets is there for $\approx$ 18 % which is negligible compared to the $\approx$ 3 dB round trip propagation loss in the waveguide itself. For the straight waveguides, the reflectivity from the end facets were measured to be $\approx$ 87 % and $\approx$ 92 % respectively at 780 nm.

6.2.3 Time-resolved discrete imaging in a slowly-driven 1D lattice

Time-resolved discrete imaging in a slowly driven 1D lattice using state-recycling was demonstrated for the first time. The experimental layout for the time-resolved discrete imaging system is given in Fig. 6.3. A supercontinuum laser with variable repetition rate from 2 MHz to 78 MHz was used as the source. As mentioned in previous chapters, the TCSPC set-up consists of start and stop arms for the time-resolved imaging.

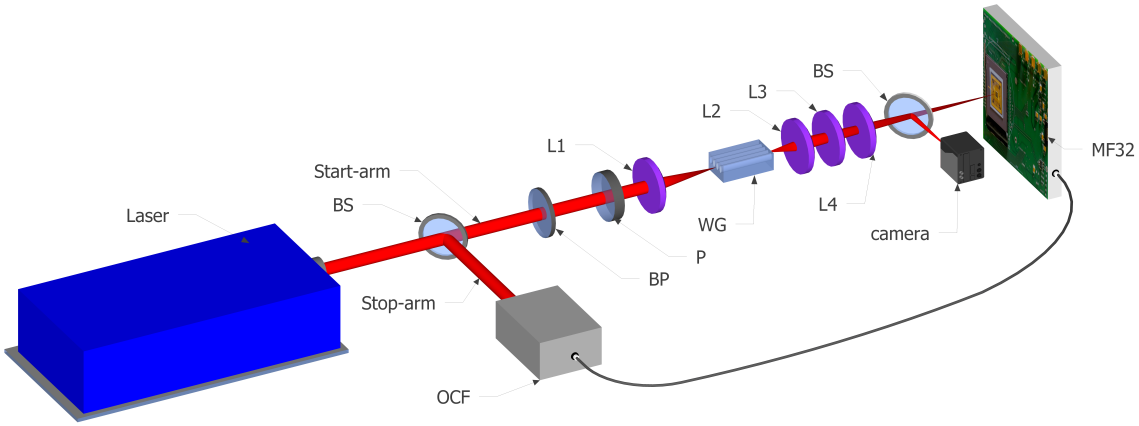

Figure 6.3: Experimental layout for time-resolved discrete imaging

In the start-arm, spectrally narrow pulses of light was selected from the supercontinuum laser using an AOTF in combination with the angle-tunable FP filter. The central wavelengths of the narrow passbands after the FP filter were measured using the conventional

spectrometer. The end waveguide on the input of the 15 mm long lattices was then excited using lens L1 ($f = 8$ mm) (indicated by red arrow in Fig. 6.4 (a)). As explained in Section 6.2.1, each unit consisting of two waveguides with periodically varying bond strengths $J_{1,2}$ (t) in time (Fig. 6.4 (b)). The sample was mounted on a nm-precision five axis flexure stage to achieve maximum alignment control. For optimum coupling, the NA of light injection should match with the NA of the waveguide in the lattice. This was achieved using a variable iris just before the input lens L1. The NA of light injection could be varied by varying the aperture size of the iris. Optimum NA of light injection and maximum coupling efficiency was achieved for a particular aperture size. At the output, the output intensity pattern of the waveguide array was imaged onto the Megaframe using L2 ($f = 15$ mm), L3 ($f = 200$ mm) and L4 ($f = 200$ mm). The magnification of the imaging system was chosen in such a way that the successive waveguide modes are imaged onto alternative pixels at the Megaframe. This will reduce any cross talk between the pixels due to scattering. A CCD camera was used to investigate the magnification of the imaging system. As mentioned earlier, the waveguides are separated by 40 μm and a magnification of 2.5 is required to image the modes into alternative individual pixels (mode spacing is 100 μm after this magnification). At this magnification, the MFD of the waveguide modes are $\approx$ 25 μm which is highly overfilled compared to the $\approx$ 6 μm active area of SPADs. The precise tuning of magnification was achieved by moving the lenses, L2, L3 and L4. Both the Megaframe and the CCD camera were placed at the focal plane of L4. The optimisation of magnification and the waveguide-SPAD mapping was achieved from the correlation between photon counts at the CCD camera image and the photon counts at the Megaframe pixels. Figure 6.5 is a schematic representation of the mode-SPAD imaging after optimising the imaging parameters. Setting the exact magnification is crucial in the TCSPC measurements as any offset in mode mapping will results an asymmetry in photon distribution at the Megaframe pixels.

In the stop-arm for TCSPC measurement, a portion of the light from the supercontinuum was tapped using a beam-splitter and coupled onto the OCF. The OCF provides stable electrical pulses to the MF 32 which stops the TCSPC measurement for each laser pulse.

By placing the lattice inside a cavity, the output state of the lattice were fed back to the cavity. The transfer of light into the nearest waveguides upon reflections from the lattice facets were observed at the Megaframe in a quasi real-time manner. Each mapped SPADs contains histogram of photon distribution from individual modes as a function of cavity round trip time. As given in Fig. 6.4 (a), light coupled into the end waveguide will be distributed to two waveguides and the relative intensities at the two waveguide modes are entirely dependent on the coupling constant which is a function of wavelength. The

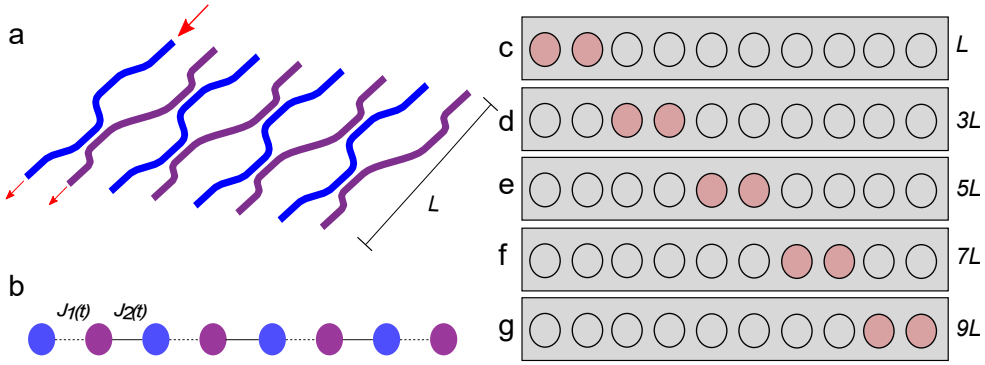

Figure 6.4: a) Layout of the slowly-driven 1D lattice used for the experiment. b) 1D representation of the lattice with bond strengths which are periodically varying in time ($J_{1,2}$ (t)). c-g) Expected intensity distribution in the waveguides when coupling light at the edge mode for cavity lengths L, $3L$, $5L$, $7L$ and $9L$.

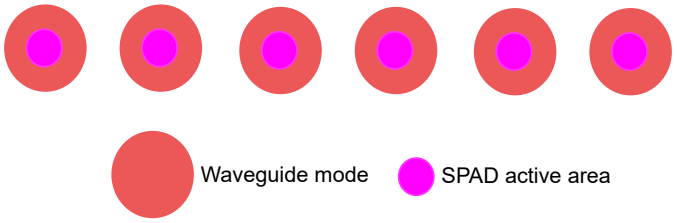

Figure 6.5: Schematic representation of mode-SPAD mapping. The size of the waveguide mode or SPAD active area does not represent the actual physical dimensions.

injection wavelength and thus the coupling constant was chosen in such a way that 50 % of light transfers into the nearest waveguide. This was achieved with an injection wavelength of 862 nm. The light was expected to hope from one unit to another for each cavity round trip. The expected light distribution in the output facet of the lattice for lattice lengths, L, $3L$, $5L$, $7L$ and $9L$ is given in Fig. 6.4 (c-g).

The polarisation state of the coupling light was set to be parallel with respect to the direction of light propagation. The relative intensity in the first two waveguides was then calculated from the total counts in the first two corresponding mapped pixels (pixels 1 and 2 in Fig. 6.6 (b)) which was found to be 49.3 % and 50.7 % respectively. This indicates that almost 50 % of light from the excited site transfers into the nearest waveguide. As given in Section 6.2.1, light coupled on a single waveguide will be evanescently coupled to the nearest waveguide at the interaction region enabling the bonds turning "ON" and "OFF" for each cavity round trip. The transfer of light (shift in spectrum at the Megaframe pixels) as a function of cavity round trip (time) is given in Fig. 6.6 (a). The duration of light transfer in the waveguides completely depends upon the length of the interaction

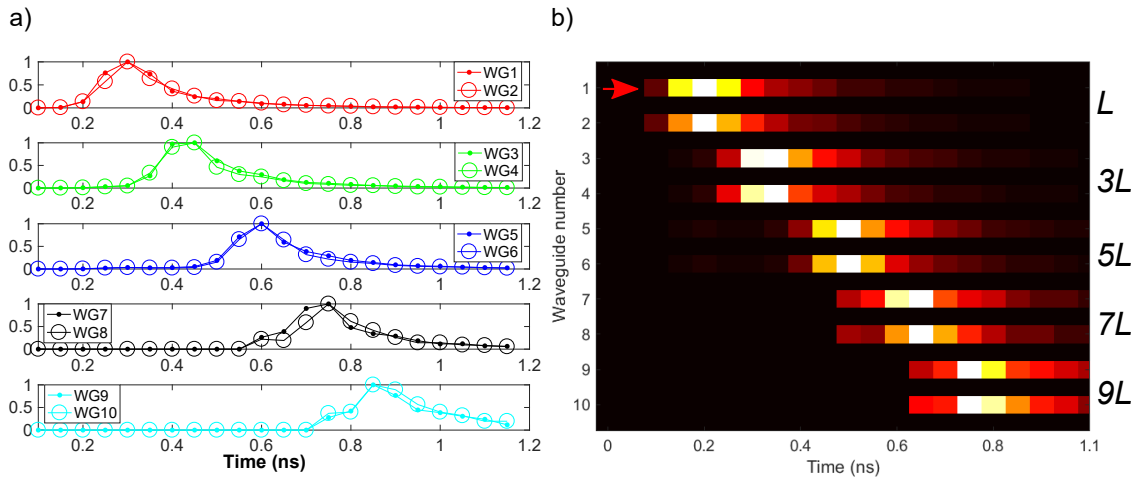

Figure 6.6: a) Observed time-resolved spectrum at the Megaframe pixels. b) A surface image of mapped SPADs showing the discretized propagation of light in the lattice for cavity lengths L, $3L$, $5L$, $7L$ and $9L$. Red arrow indicates the injection site (waveguide1).

region and the lattice length. For the 15 mm long sample, the cavity round trip time is $\approx$ 150 ps. This indicates a total time difference of 3 bins ($\approx$ 150 ps, with each bin $\approx$ 50 ps) between successive round trips at the Megaframe SPADs. Four cavity round trips were observed at the Megaframe with a clear indication of discrete transfer of light in the lattice. As mentioned, two nearby waveguides are considered as one unit. Figure 6.6 (b) presents the normalised time-resolved surface map of discrete propagation of light in the lattice for multiple round trips obtained from (a). The red arrow in Fig. 6.6 (b) indicates the excitation waveguide. The photon signal level was $<$ 0.1 per pulse which ensures the measurement was in single photon regime and the entire acquisition took $\approx$ 41,000 s. The power of light transfer between the waveguides can be controlled by tuning the wavelength of light injection.

6.2.4 Time-resolved discrete imaging in a straight 1D lattice

In a perfectly periodic 1D lattices, the photon intensity pattern after a certain length will be governed by linear discrete diffraction. A second demonstrations on discretised propagation and evolution of light in straight coupled waveguide array was performed using the Megaframe using the same state-recycling scheme. For the measurement, the slowly-driven lattices were replaced with a periodic 1D array. As given in Section 6.2.1, the fabrication parameters were set so that the waveguides confines light only in the fundamental mode above 780 nm. To understand the propagation of light in the array, we are considering the simplest situation were only one waveguide is excited at the input. Light

at 870 nm was selected from the supercontinuum laser (78 MHz repetition rate) was used to excite a single site in the waveguide array using lens L1.

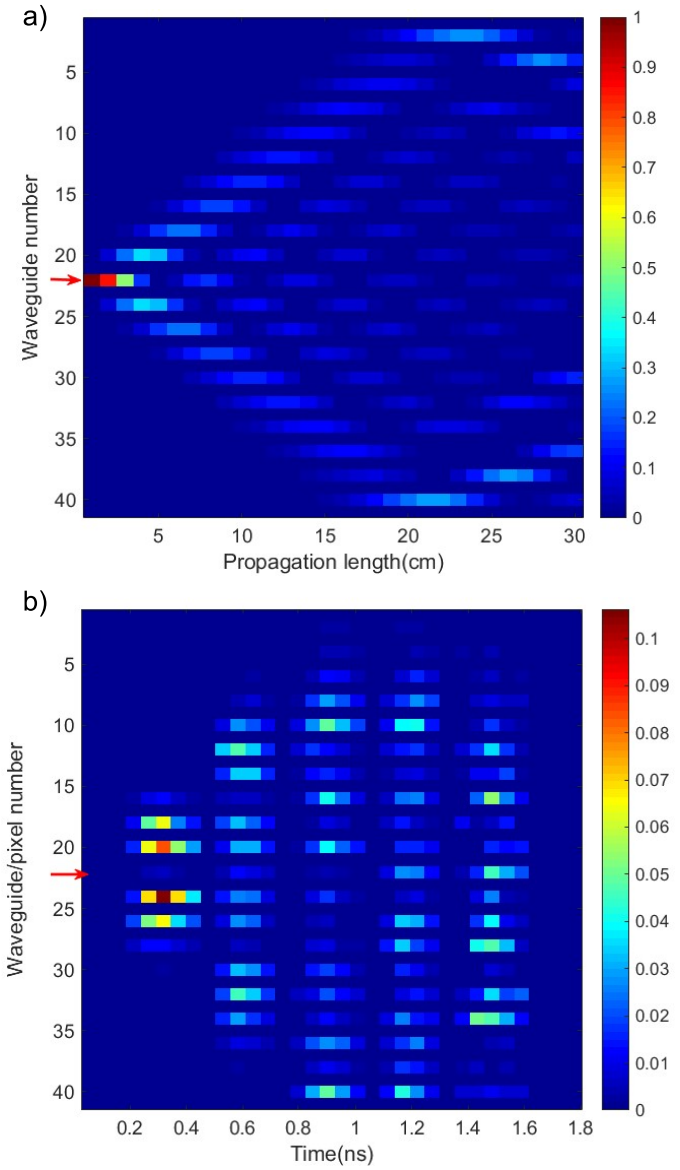

Figure 6.7: a) Simulated diffraction pattern for a 30 cm long lattice. (b) Experimentally observed diffraction pattern over an effective lattice length of 27 cm.

The output intensity distribution of the array was then imaged onto the Megaframe after exciting a waveguide in the middle (WG10) of the lattice. Here also, the output intensity distribution of the lattice was coupled back to the cavity effectively increasing the lattice length for each cavity round trip. This time the magnification was set so that each waveguide mode is imaged onto individual SPADs at the Megaframe. To image twenty modes with inter-waveguide separation 19 μm into twenty SPADs, a magnification of 2.63 is

required. This was achieved by using the output lenses L2, L3, and L4 and the over all magnification was investigated from the correlation between the CCD camera image and photon counts at individual SPADs at the Megaframe as mentioned earlier.

The imaging was then performed after optimising the magnification and waveguide-SPAD mapping. For the 30 mm long lattice, the cavity round trip time is $\approx$ 300 ps and therefore the peaks were expected to be separated by 6 time bins at the Megaframe SPADs. Four round trips were observed with a total time duration of $\approx$ 1.5 ns. This time indicates an effective lattice length of 270 mm. The photon counts per pulse was measured to be < 0.1 for the maximum illuminated pixel indicating that the TCSPC measurements were performed in single photon regime.

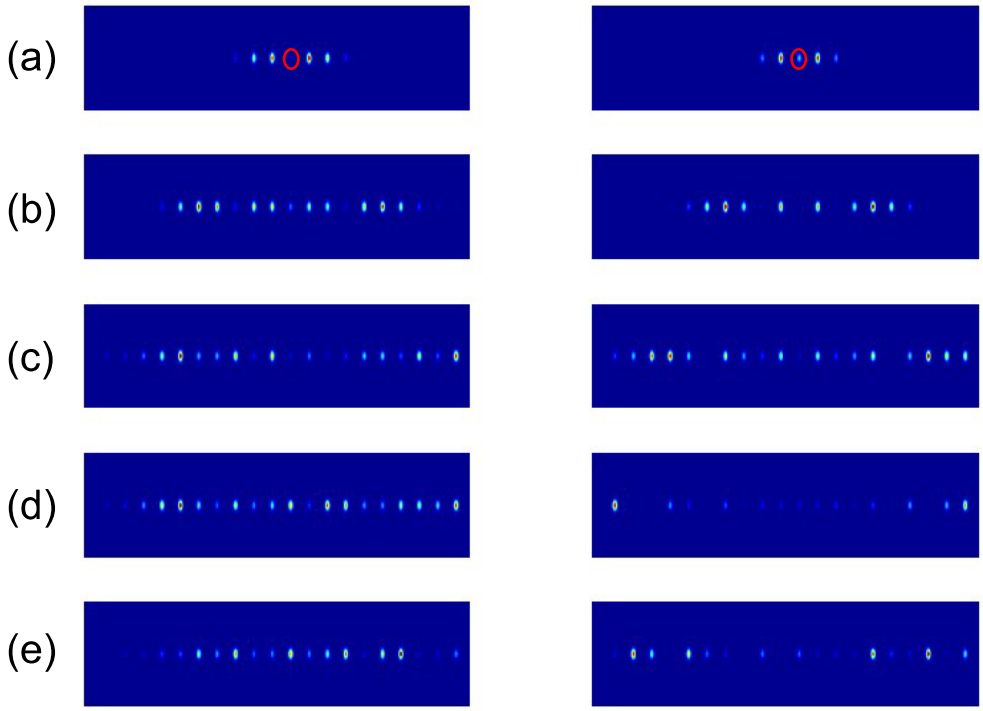

Figure 6.8: Experimental (left) and theoretical (right) diffraction pattern for lengths L (a), $3L$ (b), $5L$ (c), $7L$ (d), and $9L$ (e) obtained from Fig. 6.7.

Based on the lattice parameters, a computer simulation was then performed to investigate the experimentally observed diffraction pattern with corresponding numerical results [168]. As the first step, the coupling constants in the periodic system were investigated. We assume, the waveguides are identical and the coupling constants are same for all waveguides ie, $C_{m,n} = C_{n,m} = C$. Figure 6.7 confirms this assumption by comparing the experimentally observed diffraction pattern with the numerical results.

Figure 6.7 (a) represents the simulated theoretical diffraction pattern[2] and Fig. 6.7 (b)

[2]Simulation was performed by Dr. Sebabrata Mukherjee, see also [165]

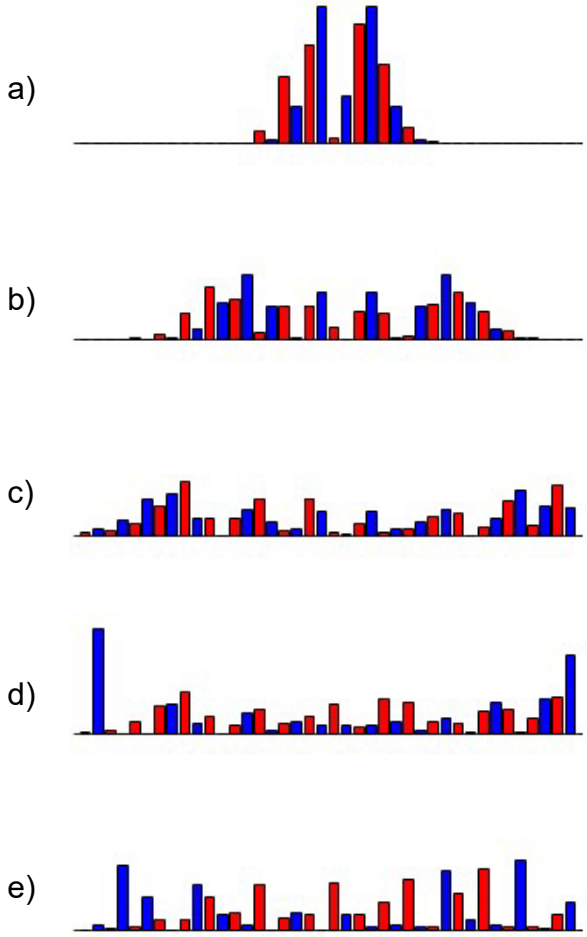

Figure 6.9: The match between experimental and the theoretical diffraction pattern for lengths L (a), $3L$ (b), $5L$ (c), $7L$ (d), and $9L$ (e) reproduced from Fig. 6.8. The red bar represents experiment and blue bar represents theory.

presents the experimental data. The red arrow in the figures indicates the injection site. The best match between the experiment and theory was achieved for a coupling constant value of 0.0275 mm^{-1}. The match between experiment and theory for cavity lengths L, $3L$, $5L$, $7L$, and $9L$ (a,b,c,d, and e respectively) are presented in Fig. 6.8. The left Figure presents experimental photon intensity distribution and the right Figure represents numerical results. The match between the experimental (red bar) and theoretical diffraction pattern (blue bar) is presented in Fig. 6.9. Both the experiment and theory confirms the discretised light propagation in a periodic array which is governed by linear discrete diffraction.

However, there is a mismatch in the experimentally observed diffraction pattern (d and e in Figures 6.8 and 6.9) compared to theoretical diffraction pattern. The reason for this

mismatch could be the phase induced effects at the lattice facets. This can occur during the sample polishing as the polishing tolerance associated with the waveguide polisher is $\pm$ 0.3 degrees. Any small misalignment of the sample in the polishing mount will introduce an angle at the end facets upon polishing. This angle can induce a phase difference between the adjacent waveguides upon reflections at the facets. To confirm this phase changes at the lattice facets, further investigations were carried out by tuning the wavelength.

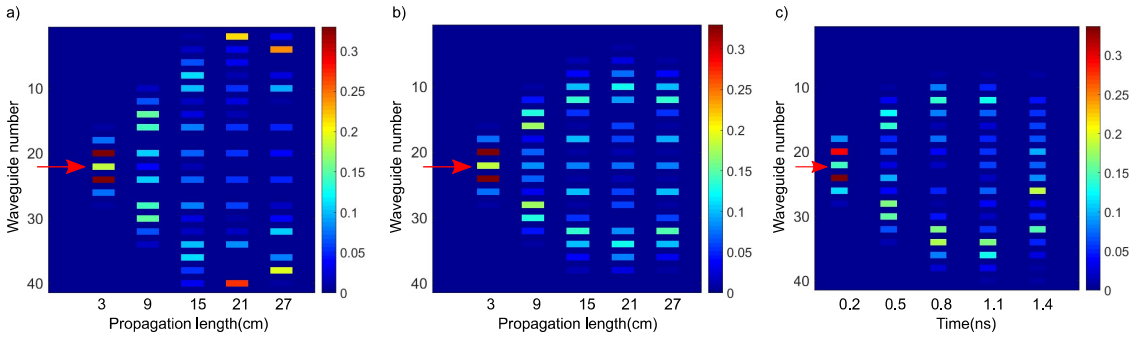

Figure 6.10: Theoretically simulated diffraction pattern without a phase difference (a) with a phase $\pi/7$ (b) and the experimentally observed diffraction pattern (c).

This time, the wavelength of light injection was reduced so that any phase change will be more evident in the diffraction pattern as the phase difference is inversely proportional to wavelength. Horizontally polarised light at 800 nm was coupled into the single waveguide (WG10) and the diffraction pattern is observed over a time duration of $\approx$ 1.5 ns. This time indicates an effective lattice length of 27 cm. The experimental and numerical results are given in Fig. 6.10. Figure 6.10 (a) represents a theoretically simulated diffraction pattern for a perfectly periodic waveguide array. The intensity pattern is expected to be linear discrete diffraction. For a perfectly periodic lattice, the light will reach the waveguide boundaries after a propagation length 5L (15 cm) as given in Fig. 6.10 (a) . Further numerical simulations were carried out to investigate how a phase change between the waveguides affects the discrete evolution of light inside the lattice. A second set of theoretical simulation was performed by introducing a phase between the adjacent waveguides. Figure 6.10 (b) shows the numerical results after introducing a phase difference of $\pi/7$ between the two nearby waveguides. It is clear that the diffraction pattern changes significantly after introducing the phase and the light tends to localise inside the lattice. The numerical result with a phase factor matches well with the experimentally observed diffraction pattern, Fig. 6.10 (c). This indicates that there is a $\pi/7$ phase difference between the waveguides in the lattice. As mentioned earlier, the reason for this could be

an angle in the facets introduced during the sample polishing. The best match between the theory and experiment was observed for a coupling constant value of 0.027 mm^{-1}. Generally speaking, the pattern is similar to Bloch oscillations observed in inhomogeneous waveguide lattices. As an example, Bloch oscillations can be observed in lattices with an introduction of linear variation in the effective refractive index across the array. A phase difference in our experiment induces the linear localisation of the electromagnetic field inside the lattice instead of unlimited spreading of light.

6.3 Chapter summary

To summarise, the discrete propagation and evolution of light in periodic 1D lattices was demonstrated for the first time using state-recycling technique. The lattices were fabricated using the ULI technique. Firstly, a set of slowly-driven synchronously bending waveguides were fabricated on a 15 mm long glass sample. Twelve units of waveguides were fabricated on the glass sample and each unit is a directional coupler. The transfer of light between the waveguides were achieved at an interaction region along the axial direction of the directional coupler. The lattice facets were then polished and coated with silver, making a linear cavity. The hopping of light to the adjacent waveguides for different cavity round trips was observed at the Megaframe SPADs by feeding the output mode profile back to the cavity. By allowing the light to reflect at the lattice facets, the propagation of light in the lattice was observed for an effective lattice length of $\approx$ 135 mm which indicates a time duration of $\approx$1.1 ns.

Secondly, discrete propagation and evolution of light in periodic straight 1D waveguide array was performed using the Megaframe. A periodic 1D array consisting of twenty straight waveguides were fabricated on a 30 mm long glass sample. The sample was polished and coated with silver allowing the re-injection of output intensity profile back to the lattice. A single site at the waveguide array was excited with monochromatic light and the waveguides are evanescently coupled. The change in field dynamics was observed over multiple round trips for an effective length of $\approx$ 270 mm which indicates total time duration of $\approx$ 1.5 ns in a quasi real-time manner. Numerical simulations were performed to justify the experimental results. A mismatch between the experimental and theoretical diffraction pattern was observed. The reason for this mismatch would be a phase change induced upon reflections at the lattice facets due to imperfect polishing of the sample. Further experiments were carried out by coupling shorter wavelengths to the lattice so that any phase change will have large impact on the diffraction pattern. The numerical results match well with the experiments indicating a phase difference of $\pi/7$ between the

nearby waveguides in the array. The localisation of light at lower wavelength suggests an angle induced periodic potential in the lattice. The discrete pattern resembles closely with that of Bloch oscillations observed on periodic potential systems. In future, different discrete phenomena in optical waveguides such as Talbot effect [29], and Anderson localisation [28] would be observed using the demonstrated technique.

Chapter 7

Conclusions

This thesis mainly focussed on the potential applications of a novel multipixel single photon sensitive detector array, Megaframe 32, based on TCSPC technique. Three key experiments in time-resolved photonic imaging is demonstrated. A literature review on single photon detectors and their applications are presented in Chapter 2. Early stage single photon detectors such as PMT, MCP-PMT, APD, and SPAD are introduced with their working principles. Design of PMTs and MCP-PMTs are described with their applications in single photon detection. A comparison of thick and thin junction Si-SPAD designs is given with relevant literature review on their characteristic parameters. The electric field distribution, multiplication gain, noise, SNR of APDs are explained with theoretical derivations. The quenching circuits in APDs are given with their respective circuitry. A comparison of different single photon detector technologies is given with their relative merits. Working principle of TCSPC is explained with basic TCSPC architecture. The Chapter also introduced the Megaframe 32, a novel multipixel single photon detector consisting of 32×32 square array of Si-SPAD pixels with individual TDC for TCSPC. The block diagram, TDC architecture, single pixel layout of Megaframe detector were presented along with the key detector parameters. The PDE of the Megaframe SPADs is presented for different excess bias voltages. Due to the bandgap of silicon, the spectral sensitivity of the Megaframe is limited from 400 nm to 1100 nm spectral region. The maximum PDE is reported to be 28% for an excess bias 1.4 V.

A literature review on guided wave optics is presented in Chapter 3. Dispersion and loss in optical fibres were explained. Modal, material and waveguide dispersions in the fibres were briefly explained. Extrinsic and intrinsic losses in fibres were explained with their effects in signal transmission. Extrinsic and intrinsic losses in optical fibres have been presented. Extrinsic losses are classified into bending losses, launching losses and connector losses. The effect of fibre bend radius on attenuation is outlined. It is observed that bending loss is higher for small bending radius. The launching losses in the fibre can be

greatly minimised by choosing the lens with the same NA that of the optical fibre. The major intrinsic loss in optical fibres is caused by the OH^- molecule present in the fibre which absorbs in the NIR-IR portion of the spectrum. Linear and non-linear scattering loss mechanisms in optical fibres is explained. With a λ^{-4} dependence, Rayleigh scattering is the most predominant linear scattering loss mechanism in optical fibres. Guided modes in optical waveguides were explained with theoretical derivation of mode parameters. The coupled mode theory in a two waveguide system is derived. The transfer of power in evanescently coupled waveguides depends on the propagation constant of the modes. Finally, the Chapter introduced fibre-photonic lantern, with their fabrication techniques and important characterisation parameters. The fibre tapering process is explained with the example of a SMF.

In the first experimental demonstration, Chapter 4 discussed multiplexed single-mode WTM of multimode light using the Megaframe. The WTM concept in optical fibres was explained. A PL was introduced for the efficient collection and reformatting of multimode states of light into an array of Megaframe SPAD pixels. First, the MCF-PL was characterised in detail. The cross coupling between MCF cores, MCF cores positions, MCF mode-field diameter, MCF propagation loss were experimentally measured. From the cross coupling measurements, it was observed that the cross talk is negligible between the MCF cores below 620 nm. The core-to-core separation in the MCF was measured using near field imaging. A computer simulation was then performed to measure the deviation of MCF core positions from a perfectly square grid. A minimum RMS value of 0.54 μm was obtained between the measured core positions and the grid for a grid spacing of 10.53 μm. The MFD of the MCF cores were measured from calibrated imaging system. The MCF cores exhibit a $1/e^2$ MFD of 1.83 μm $\pm$ 0.04 μm in one axis and 1.85 μm $\pm$ 0.05 μm on the other. A propagation loss of $\approx$ 0.1 dBm^{-1} was measured using fibre cutback method. The NA and insertion loss of multimode end of PL were calculated. The NA of the multimode end of the PL was measured to be 0.15 using near field imaging. The insertion loss of PL was calculated to be $\approx$ 1.2 dB for an NA 0f 0.03. The WTM instrument was characterised in detail and well calibrated over a wavelength region of 500-600 nm. By mapping 121 MCF cores onto 121 SPADs on the Megaframe, core specific dispersions in MCF was calculated from the arrival time of photons at the SPADs. Across the MCF, the dispersion in the cores at 550 nm was measured to be 500.34 $\pm$ 30.86 ps nm^{-1} km^{-1}. Multiplexed WTM of multimode light was then performed across the 500-600 nm spectral region. An effective fill factor improvement of SPADs by factor of 46 was achieved using custom imaging system which is a significant improvement compared to 1 % fill-factor of the detector array.

Light-in-flight imaging of spatial modes in a FMF is demonstrated in Chapter 5. With a timing resolution of ≈ 50 ps, the linearly polarised modes were imaged on the Megaframe SPADs using TCSPC technique. Initially, light at central wavelength 532 nm was coupled onto ≈ 1 km length of SMF-28 fibre. At this wavelength, the fibre supports six LP modes and all the modes were excited at the input of the fibre with an overfilled launching condition. The output of the fibre was then imaged onto the Megaframe and light-in-flight imaging of spatial modes were performed. From the FWHM of the DMD profile at the Megaframe, the resolution of the instrument was calculated to be ≈ 0.56 psm^{-1}. The experiment was repeated by coupling short passbands of light across the 500 nm to 600 nm spectral region onto the fibre. The passbands were selected by the combination of bandpass filters and an angle tunable FP filter. The FWHM of the passbands were restricted to < 2 nm by angle tuning the FP filter to reduce the pulse broadening at the pixels due to chromatic dispersion. The WTM of spatial modes was performed for all passbands of light and the chromatic dispersion of the modes were measured from the arrival time of photons at the Megaframe. The relative modal delay of spatial modes with respect to the fundamental mode and the effective refractive index difference between the closest mode groups were then measured. The result obtained from the experiment is comparable with the values offered by current fibre characterisation techniques. A comparison of DMD measurements using the demonstrated technique and other common approaches is given.

Finally, to showcase the application of Megaframe in discrete optics, time-resolved discrete imaging in photonic lattices was realised using state-recycling technique in Chapter 6. Two types of 1D lattices were fabricated using ULI technique to demonstrate the discrete propagation and evolution of light. First, the hopping of light in synchronously bending waveguide array was observed at the SPAD pixels in space-time by placing the 15 mm long lattice in a linear cavity. By coating the end facet of the lattice with silver, the output state of the waveguide array is re-injected back to the lattice and the evolution of light was observed at the Megaframe pixels in real-time for each cavity round trip. Five cavity round trips were monitored on Megaframe SPADs indicating an effective lattice length of ≈ 135 mm which is equal to a time duration of $\approx$1.1 ns. Secondly, the discretised dynamics of light in an array of straight 1D waveguides was monitored at the Megaframe pixels. The facets of a 30 mm long lattice was coated with silver and light was coupled onto a single site of the lattice. The evolution of light was observed over multiple round trips for an effective length of ≈ 270 mm which indicates total time duration of ≈ 1.5 ns in a quasi real-time manner. The mismatch in the recorded time-resolved mode pattern at the Megaframe and the theoretical mode pattern indicated there is a phase induced effect in the diffraction pattern. To justify the experimental results,

numerical simulations were performed by introducing a $\pi/7$ phase difference between the waveguides. Both the theory and experiment confirms the discrete behaviour of light in waveguide lattices.

7.1 Future scope of work

The experimental demonstrations using Megaframe opens endless possibilities in real-time photonic applications. Especially, WTM can find application in photon-starved applications such as Raman spectroscopy, Coherent LIDAR and quantum optics. In life science applications, the fast sampling capability and high detection efficiency of Megaframe could be used to acquire fluorescence signals without any significant loss. Since each SPAD acts as individual detector channels, higher SNR can be achieved which is a major concern in medical applications. In LIDAR, the collection efficiency and single mode conversion of PL can be effectively used for clean heterodyne mixing. As an effective space-time imaging tool, the Megaframe opens a new route towards real-time soliton imaging, time-stretch microscopy, and time-resolved back scattering imaging. By utilising higher order modes in fibre, more degrees of freedom can be achieved in time-stretch confocal microscopy and imaging. In discrete optics, the state recycling technique using Megaframe can be used to observe phenomena in optical waveguides such as Anderson localisation, Wannier-Stark localisation, Talbot's effect, two particle interactions, and topological edge states which are not possible with other existing imaging techniques.

Chapter 8

References

[1] W. Heisenberg, *The Physical content of quantum kinematics and mechanics,* (Princeton, NJ: Princeton University Press), 62–84 (1983).

[2] C. H. Bennett, and G. Brassard, *Quantum cryptography:public key distribution and coin tossing,* Proc. Int. Conf. on Computers, Systems & Signal Processing (Bangalore,India) 175–9 (1984).

[3] E. Knill, R. Laflamme, and G. J. Milburn, *A scheme for efficient quantum computation with linear optics,* Nature 409, 46 (2001).

[4] P. Lodahl, *Quantum-dot based photonic quantum networks,* Quantum Sci. Technol. 3, 013001 (2018).

[5] J. S. Massa, A. M. Wallace, G.S. Buller, S. J. Fancey, and C. A. Walker, *Laser depth measurement based on time–correlated single photon counting,* Opt. Lett. 22, 543–5 (1997).

[6] S. Bellis, C. Jackson, and A. Konig, *Photon counting sensors for medical and biophotonic applications*, Laser+Photonik, 534–8 (2005).

[7] *http://sales.hamamatsu. com/index.php?id = 13195879*

[8] S Cova, M Ghioni, A Lacaita, C Samori, and F Zappa, *Avalanche photodiodes and quenching circuits for single-photon detection,* In: Applied optics 35, 1956–76 (1996).

[9] G. S. Buller and R. J. Collins, *Single-photon generation and detection,* In: Measurement Science and Technology 21, 012002 (2010).

[10] J. Wu, D. Wang, C. J. Rosen, and M. E. Bauer, *Comparison of petiole nitrate concentrations, SPAD chlorophyll readings, and QuickBird satellite imagery in detecting nitrogen status of potato canopies,* In: Field Crops Research 101.1, 96–103 (2007).

[11] I. Samsone, U. Andersone, M. Vikmane, B. Ievi¸na, G. Pakarna, and G. Ievinsh, *Nondestructive methods in plant biology: an accurate measurement of chlorophyll content by a chlorophyll meter,* In: Acta Univ. Latv 723, 145–154 (2007).

[12] X Michalet, O. H. W. Siegmund, J. V. Vallerga, P. Jelinsky, J. E. Millaud, and S. Weiss, *Detectors for single-molecule fluorescence imaging and spectroscopy* In: Journel of Modern Optics 54.2-3, 239–289 (2007).

[13] L. Q. Li, and L. M. Davis, *Single photon avalanche diode for single molecule detection,* In: Review of Scientific Instruments 64.6, 1524 (1993).

[14] G. Bonanno, M. Belluso, F. Zappa, S. Tisa, S. Cova, P. Maccagnani, D. Calia, R. Saletti, R. Roncella, and S. Billotta, *Spada: An Array of Spad Detectors For Astrophysical Applications* In: Experimental Astronomy 19.1-3, 163–168 (2005).

[15] M. Legré, R. Thew, H. Zbinden, and N. Gisin, *High resolution optical time domain reflectometer based on 1.55μm up-conversion photon-counting module,* Opt. Express 15.13, 8237–8242 (2007).

[16] S. Burri and E. Charbon, *SPAD Image Sensors: From Architectures to Applications,* In: Imaging and Applied Optics Technical Papers. Optical Society of America, ITu4C.1 (2012).

[17] P. Antognetti, S. Cova, and A Longoni, *A study of the operation and performances of an avalanche diode as a single-photon detector,* Proc. 2nd ISPRA Nuclear Electronics Symp. (Stresa, Italy) pp 453–6 (1975).

[18] S. Cova, A. Longoni and A. Andreoni, *Towards picosecond resolution with single-photon avalanche diodes,* Rev. Sci. Instrum. 52 408–12 (1981).

[19] R.J. McIntyre, *Recent developments in silicon avalanche photodiodes,* Measurement 3 (4),146–152 (1985).

[20] A. Rochas, A. R. Pauchard, P. A. Besse, D. Pantic, Z. Prijic, and R. S. Popovic, *Low-noise silicon avalanche photodiodes fabricated in conventional CMOS technologies,* IEEE Trans. Electron Devices 49, 387 (2002).

[21] J. Richardson, R. Walker, L. Grant, D. Stoppa, F. Borghetti, E. Charbon, M. Gersbach, and R. K. Henderson, *A 32×32 50ps resolution 10 bit time to digital converter array in 130nm CMOS for time correlated imaging,* 2009 IEEE Custom Integrated Circuits Conference, San Jose, CA, 77-80 (2009).

[22] S P. Poland, N. Krstajić, J. Monypenny, S. Coelho, D. Tyndall, R. J. Walker, V. Devauges, J. Richardson, N. Dutton, P.l Barber, D. D. Li, K. Suhling, T. Ng, R. K. Henderson, and S. M. Ameer-Beg, *A high speed multifocal multiphoton fluorescence lifetime imaging microscope for live-cell FRET imaging,* Biomed. Opt. Express 6 (2015).

[23] H. K. Chandrasekharan, F. Izdebski, I. Gris-Sánchez, N. Krstajić, R. Walker, H. L. Bridle, P. A. Dalgarno, W. N. MacPherson, R. K. Henderson, T. A. Birks, and R. R. Thomson, *Multiplexed single-mode wavelength-to-time mapping of multimode light,* Nat. Comm. 8 (2017).

[24] G. Gariepy, N. Krstajić, R. Henderson, C. Li, R. R. Thomson, G. S. Buller, B. Heshmat, R. Raskar, J. Leach, and D. Faccio, *Single-photon sensitive light-in-flight imaging,* Nat. Comm. 6 (2015).

[25] Z. Meng, G. I. Petrov, S. Cheng, J. A. Jo, K. K. Lehmann, V. V. Yakovlev, and M. O. Scully, *Lightweight Raman spectroscope using time-correlated photon-counting detection,* PNAS 112, 12315–12320 (2015).

[26] F. Bloch, *Über die Quantenmechanik der Elektronen in Kristallgittern,* Z. Phys. 52, 555–600 (1928).

[27] C.Zener, *A theory of the electrical breakdown of solid dielectrics,* Proc. R. Soc. London Ser. A 145, 523–529 (1932).

[28] L. Martin, G. D. Giuseppe, A. Perez-Leija, R. Keil, F. Dreisow, M. Heinrich, S. Nolte, A. Szameit, A. F. Abouraddy, D. N. Christodoulides, and B. E. A. Saleh, *Anderson localization in optical waveguide arrays with off-diagonal coupling disorder,* Opt. Express 19, 13636-13646 (2011).

[29] Z. Chen, Y. Zhang, and M. Xiao, *Discrete Talbot effect in two-dimensional waveguide arrays,* Opt. Express 23, 14724-14733 (2015).

[30] G. Petrov, V. Yakovlev, and V. Shcheslavskiy, *Raman spectroscopy without spectrometer,* in CLEO:2011 - Laser Applications to Photonic Applications, OSA Technical Digest (CD) (Optical Society of America, 2011), paper PDPB6.

[31] F. Zappa, A. L. Lacaita , S. D Cova, and P. Lovati, *Solid-state single-photon detectors,* Opt. Eng.35 938–45 (1996).

[32] G. A. Morton, *Photomultipliers for scintillation counting,* RCA Rev.10, 525–553 (1949).

[33] *New gated MCP-PMTs and their performances in comparison with semiconductor type detectors for SLR applications,* `http://cddis.gsfc.nasa.gov/lw18/docs/papers/Posters/13-Po28-Taguchi.pdf.(2015).`

[34] *Photomultiplier Tubes, http://www.olympusmicro.com/primer/digitalimaging.html*

[35] *Phtotmultiplier Tubes: Basics and Applications,* Third edition, Hamamatsu (2007).

[36] *http://jp.hamamatsu.com/resources/products/etd/pdf/m-h7422e.pdf.*

[37] J. Gower, *Optical Communications Systems,* 2nd edn. (Englewood Cliffs, NJ: Prentice Hall) (1993).

[38] H. Kume, K. Koyama, K. Nakatsugawa, S. Suzuki, and D. Fatlowitz, *Ultrafast microchannel plate photomultipliers,* Appl. Opt.27, 1170–1178 (1988).

[39] W. Becker, A. Bergmann, C. Biskup, L. Kelbauskas, T. Zimmer, N. Klocker, and K. Benndorf, *High resolution TCSPC lifetime imaging,* In: Biomedical Optics 2003. International Society for Optics and Photonics, 175–184 (2003).

[40] A. D. Guerra, N. Belcari, M. G. Bisogni, F. Corsi, M. Foresta, P. Guerra, S. Marcatili, A. Santos, and G. Sportelli, *Silicon Photomultipliers (SiPM) as novel photodetectors for PET,* In: Nuclear Instruments and Methods in Physics Research Section A: Accelerators, Spectrometers, Detectors and Associated Equipment 648.0, S232–S235 (2011).

[41] Y. Acharya, S. Sharma, and H. Chandra, *Signal induced noise in PMT detection of lidar signals,* In: Measurement 35.3, 269–276 (2004).

[42] W. G. Lawrence, G. Varadi, G. Entine, E. Podniesinski, and P. K. Wallace, *A comparison of avalanche photodiode and photomultiplier tube detectors for flow cytometry,* In: Proc. SPIE 6859, 68590M–68590M–11 (2008).

[43] M. Razeghi, *Technology of Quantum Devices,* Vol. 1. Springer US (2010).

[44] F. Izdebski, *Quantum correlations measured with multi-pixel detectors,* PhD thesis. Heriot-Watt University School of Engineering and Physical Sciences (2013).

[45] L. Z. Jie, *Characterisation of Single Photon Avalanche Detectors*, http://www.qolah.org/thesis/thesis_janet.pdf.

[46] A. G. Chynoweth, *Ionization rates for electrons and holes in Silicon,* Phys. Rev., vol. 109, no. 5, 1537–1540 (1958).

[47] http://www.hamamatsu.com/jp/en/community/optical_sensors/articles/guide_to_detector_selection/index.html

[48] D.V Perepelitsa, *Johnson noise and shot noise,* Analysis 2, 2-5 (2006).

[49] E. Charbon, M. Fishburn, R. Walker, R. K. Henderson, and C. Niclass, *SPAD Based Sensors,* Ed. by F. Remondino and D. Stoppa, Springer Berlin Heidelberg (2013).

[50] R. J. McIntyre, *On the avalanche initiation probability of avalanche diodes above the breakdown voltage,* IEEE Trans. Electron Devices20(7), 637–641 (1973).

[51] F. Zappa, S. Tisa, S. Cova, P. Maccagnani, D. B. Calia, R. Saletti, R. Roncella, G. Bonanno, and M. Belluso, *Single-photon avalanche diode arrays for fast transients and adaptive optics* In: Instrumentation and Measurement, IEEE Transactions on 55.1, 365–374 (2006).

[52] S. Cova, M. Ghioni, A. Lotito, I. Rech, and F. Zappa, *Evolution and prospects for single-photon avalanche diodes and quenching circuits*, Journal of modern optics, vol.51, no.9–10, 1267–1288 (2004).

[53] R. H. Hadfield, *Single-photon detectors for optical quantum information applications,* In: Nat. Phot. 3. 12, 696–705 (2009).

[54] *http://www.microphotondevices.com/products_pdm.asp.*

[55] *http://optoelectronics.perkinelmer.com/content/RelatedLinks/SpecificationSheets-/SPC_PhotoDetectors.pdf.*

[56] C. Gobby, Z. L. Yuan, and A.J Shields, *Quantum key distribution over 122 km of standard telecom fiber,* Appl. Phys. Lett. 84, 3762–3764 (2004).

[57] A. R. Dixon, Z. L. Yuan, J. F. Dynes, A. W. Sharpe, and A. J. Shields, *Gigahertz decoy quantum key distribution with 1 Mbit/s secure key rate,* Opt. Express 16, 18790-18797 (2008).

[58] *http://jp.hamamatsu.com/resources/products/etd/pdf/m-h7422e.pdf*

[59] *http://jp.hamamatsu.com/resources/products/etd/pdf/NIR-PMT_APPLI_TPMO1-040E02.pdf.*

[60] H. Takesue, S. W. Nam, Q. Zhang, R. H. Hadfield, T. Honjo, K. Tamaki, and Y. Yamamoto, *Quantum key distribution over a 40-dB channel loss using superconducting single photon detectors,* Nat. Phot. 1, 343–8 (2007).

[61] *https://www.idquantique.com/single-photon-systems/products/id281/*

[62] Q. Zhang, H. Takesue, T. Honjo, K. Wen, T. Hirohata, M. Suyama, Y. Takiguchi, H. Kamada, Y. Tokura, O. Tadanaga, Y. Nishida, M. Asobe and Y. Yamamoto, *Megabits secure key rate quantum key distribution,* New J. Phys. 11, 045010 (2009).

[63] D. Rosenberg, A E. Lita, A. J. Miller, and S. W. Nam, *Noise-free high-efficiency photon-number-resolving detectors,* Phys. Rev. A 71, 061803 (2005).

[64] A. Migdall, S. V. Polyakov, J. Fan, and J. C. Bienfang, *Single-Photon Generation and Detection: Physics and Applications,* Academic Press (2013).

[65] P. A. Hiskett, G. Bonfrate, G. S. Buller, and P. D. Townsend, *Eighty kilometre transmission experiment using an InGaAs/InP SPAD-based quantum cryptography receiver operating at 1.55 μm,* In: Journal of Modern Optics 48. 13, 1957–1966 (2001).

[66] M. Benetti, M. Popleteeva, G.-F. Dalla Betta, L. Pancheri, and D. Stoppa, *Characterization of a CMOS SPAD sensor designed for fluorescence lifetime spectroscopy,* In: 2011 7th Conference on Ph.D. Research in Microelectronics and Electronics (PRIME), 185–188 (2011).

[67] W. Becker, *Advanced Time- Correlated Single Photon Counting Techniques,* Ed. by A. Castleman, J. J. P. Toennies, and W. Zinth, Springer (2005).

[68] *http://www.indeco.jp/indeco_online/main/pdf/ei_what_is_TCSPC.pdf.*

[69] Justin A. Richardson, *Time resolved single photon imaging in nanometer scale CMOS technology,*, Thesis (2010).

[70] J. A Richardson, and R. K Henderson, *Low dark count single-photon avalanche diode structure compatible with standard nanometer scale CMOS technology,* IEEE Photonic Technol. Lett. 21, 1020–1022 (2009).

[71] M. Ghioni, S. Cova, I. Rech, and F. Zappa, *Monolithic dual-detector for photon correlation spectroscopy with wide dynamic range and optical 70-ps resolution,* In: Quantum Electronics, IEEE Journal of 37.12, 1588–1593 (2001).

[72] T. A. Birks, I. Gris-Sánchez, S. Yerolatsitis, S. G. Leon-Saval, and R. R. Thomson, *The photonic lantern,* Adv. Opt. Photonics 7, 107–167 (2015).

[73] M. J. Senior, *Optical Fiber Communications: Principles and Practice,* Ed. by J.Midwinter, A. Snyder, and B. Weiss. 2nd. 2. Prentice Hall (1992).

[74] L. Thevenaz, J. Pellaux, N. Gisin, V. Weid, and J. Pierre, *Review of chromatic dispersion measurements techniques,* In EFOC/LAN" 89 Technical Digest, no. EPFL-CONF-173763, 217-220, IGI-Europe, (1989).

[75] *http://www.fiber-optic-cable-sale.com/overview-of-single-mode-fiber-types.html*

[76] C. R. Paiva, *Fotónica, Fibras Ópticas,* DEEC, IST (2008).

[77] G. P. Agrawal, *Fiber-Optic Communications Systems,* Third Edition, John Wiley & Sons (2002).

[78] M. Miyagi, and S. Nishida, *Pulse spreading in a single-mode fiber due to third-order dispersion,* Appl. Opt. 18, 678-682 (1979).

[79] L. Ramos, R. Ramos, and H. Salgado, *Characterization of Fiber Bragg Grating for Dispersion Compensation* Universidade do Porto, 2004, `http://luisrio.no.sapo.pt/faculdade/projecto/report.html`.

[80] D. Marcuse, and C. Lic, *Low dispersion single-mode fiber transmission—the question ofpractical versus theoretical maximum transmission bandwidth,* IEEE J. Quantum Electron., QE-17, 869-878 (1981).

[81] N. Lagakos, J. H. Cole, and J. A. Bucaro, *Microbend fiber-optic sensor,* Appl.Opt., vol. 26, no. 11, 2171 (1987).

[82] G. Aldabaldetreku, G. Durana, J. Zubia, J. Arrue, F. Jiménez, and J. Mateo, *Analysis of intrinsic coupling loss in multi-step index optical fibres,* Opt. Express 13, 3283-3295 (2005).

[83] A. W. Snyder, and J. D. Love, *Optical Waveguide Theory,* Chapman and Hall, London (1983).

[84] M. Kawachi, A. Kawana, and T. Miyashita, *Low-Loss single-mode fibre at the material-dispersion-free wavelength of 1.27 μm,* Electronics Letters, vol. 13, no. 15, 442-443 (1977).

[85] R. Kitamura, L. Pilon, and M. Jonasz, *Optical constants of silica glass from extreme ultraviolet to far infrared at near room temperature,* Appl. Opt. 46, 8118-8133 (2007).

[86] J. M. Florence, C. C. Allshouse, F. W. Glaze, and C. H.Hahner, *Absorption of Near-Infrared Energy by Certain Glasses,*Journal of Research of the National Bureau of Standards, Vol 45, No.2, 2118, August (1950).

[87] D. Gloge, *Weakly Guiding Fibers,* Appl. Opt. 10 (1971).

[88] J. C. Bose *On the influence of the thickness of air-space on total reflection of electric radiation,* Proceedings of the Royal Society of London, 62, no. 379-387, 300-310 (1898).

[89] J. R. Pierce, *Coupling of Modes of Propagation,* Journal of Applied Physics, 179-183 (1954).

[90] S. E. Miller, *Coupled wave theory and waveguide applications,* BellSyst. Tech. J. 33, 661-719 (1954).

[91] A. W Snyder, *Coupled-mode theory for optical fibers,* J.Opt. Soc. Am. 62, 1267-1277 (1972).

[92] D. Marcuse, *Coupled mode theory of round optical fibers,* Bell Syst. Tech. J. 52, 817-842 (1973).

[93] A. Yariv, *Coupled-mode theory for guided-wave optics,* IEEE Journal of Quantum Electronics, 919-933 (1973).

[94] H. Kogelnik, *Theory of dielectric waveguides,* in Integrated Optics, T. Tamir, ed. Springer-Verlag, New York (1975).

[95] Wei-Ping Huang, *Coupled-mode theory for optical waveguides: an overview,* J. Opt. Soc. Am. A 11, 963-983 (1994).

[96] A. Yariv, *Quantum Electronics,* -3rd Ed. John Wiley & Sons New York (1989).

[97] Sebabrata Mukherjee, *Experimental simulation of solid-state phenomena using photonic lattices,* Thesis, Heriot Watt University (2016).

[98] S. G. Leon-Saval, T. A. Birks, J. Bland-Hawthorn, and M. Englund, *Multimode fiber devices with single-mode performance,* Opt. Lett. 30, 2545–2547 (2005).

[99] J. D. Love and W. M. Henry, *Quantifying loss minimisation in single-mode fibre tapers,* Electron. Lett. 22, 912-914 (1986).

[100] J. D. Love, W. M. Henry, W. J. Stewart, R. J. Black, S. Lacroix, and F. Gonthier, *Tapered single-mode fibres and devices. I. Adiabaticity criteria,* IEE Proc. Pt. J 138, 343-354 (1991).

[101] K. Saitoh, M. Koshiba, K. Takenaga, and S. Matsuo, *Crosstalk and core density in uncoupled multi-core fibers,* IEEE Photon Technol Lett. 24 (21), 1898–901 (2012).

[102] A. Perperidis, H. E. Parker, A. Karam-Eldaly, Y. Altmann, K. Dhaliwal, R. R. Thomson, M. G. Tanner, and S. McLaughlin, *Characterization and modelling of inter-core coupling in coherent fiber bundles,* Opt. Express 25, 11932-11953 (2017).

[103] X. Chen, K. L. Reichenbach, and C. Xu, *Experimental and theoretical analysis of core-to-core coupling on fiber bundle imaging,* Opt. Express 16, 21598-21607 (2008).

[104] T. Hayashi, T. Taru, O. Shimakawa, T. Sasaki, E. Sasaoka, *Design and fabrication of ultra-low crosstalk and low-loss multi-core fiber,* Opt. Express 19, 16576–92 (2011).

[105] T. Hayashi, T. Taru, O. Shimakawa, T. Sasaki and E. Sasaoka, *Ultra-low-crosstalk multi-core fiber feasible to ultra-long-haul transmission,* 2011 Optical Fiber Communication Conference and Exposition and the National Fiber Optic Engineers Conference, Los Angeles, CA, 1-3 (2011).

[106] T. Saito, K. Watanabe, K. Suematsu and M. Shiino, *Confirmation of Core Pitch Accuracy of Fiber Bundle Type Fan-Out for MCF,* 2014 IEEE Photonics Society Summer Topical Meeting Series, Montreal, QC, 168-169 (2014).

[107] C. D.Hussey, and F.Martinez, *Approximate analytical forms for the propagation characteristics of single-mode optical fibres,* Electron. Lett. 21, 1103–1104 (1985).

[108] M. Young, *Mode-field diameter of single-mode optical fiber by far-field scanning,* Appl. Opt. 37, 5605-5619 (1998).

[109] T. Matsui, K. Nakajima, and T. Sakamoto, *Effective mode-field diameter for few-mode fibers for considering splice loss characteristics,* Appl. Opt. 56, 7484-7490 (2017).

[110] A. T. Pedersen, L. Gruner-Nielsen and K. Rottwitt, *Low Wavelength Loss of Germanium Doped Silica Fibers,* OFC/NFOEC 2008 - 2008 Conference on Optical Fiber Communication/National Fiber Optic Engineers Conference, San Diego, CA, 1-3 (2008).

[111] S. Sakaguchi, and S. Todoroki, *Optical properties of GeO_2 glass and optical fibers,* Appl. Opt. 36, 6809-6814 (1997).

[112] A. Horton, R. Content, S. Ellis, and J. Lawrence, *Photonic lantern behaviour and implications for instrument design,* Advances in Optical and Mechanical Technologies for Telescopes and Instrumentation, Navarro, Cunningham, Barto, Editors, Proc. SPIE 9151, 9151-72 (2014).

[113] D. Noordegraaf, P. M. W. Skovgaard, M. D. Maack, J. Bland-Hawthorn, R. Haynes, and J. Lægsgaard, *Multi-mode to single-mode conversion in a 61 port Photonic Lantern,* Opt. Express 18, 4673-4678 (2010).

[114] N. Bai, E. Ip, Y. Huang, E. Mateo, F. Yaman, M. Li, S. Bickham, S. Ten, J. Liñares, C. Montero, V. Moreno, X. Prieto, V. Tse, K. M. Chung, A. P. T. Lau, H. Tam, C. Lu, Y. Luo, G. Peng, G. Li, and T. Wang, *Mode-division multiplexed transmission with inline few-mode fiber amplifier,* Opt. Express 20 (2012).

[115] R. G. H. van Uden, R. Amezcua Correa, E. Antonio Lopez, F. M. Huijskens, C. Xia, G. Li, A. Schülzgen, H. de Waardt, A. M. J. Koonen, and C. M. Okonkwo, *Ultra-high-density spatial division multiplexing with a few-mode multicore fibre,* Nat. Phot. 8 (2014).

[116] D. J. Richardson, J. M. Fini, and L. E. Nelson, *Space-division multiplexing in optical fibres*, Nat. Phot. 7 (2013).

[117] S. Randel, R. Ryf, A. Gnauck, M. A. Mestre, C. Schmidt, R. Essiambre, P. Winzer, R. Delbue, P. Pupalaikis, A. Sureka, Y. Sun, X. Jiang, and R. Lingle, *Mode-Multiplexed 6×20-GBd QPSK Transmission over 1200-km DGD-Compensated Few-Mode Fiber,* in Optical Fiber Communication Conference, OSA Technical Digest (Optical Society of America), paper PDP5C.5 (2012).

[118] R. Ryf, S. Randel, N. K. Fontaine, M. Montoliu, E. Burrows, S. Chandrasekhar, A. H. Gnauck, C. Xie, R. Essiambre, P. Winzer, R. Delbue, P. Pupalaikis, A. Sureka, Y.

Sun, L. Gruner-Nielsen, R. V. Jensen, and R. Lingle, *32-bit/s/Hz Spectral Efficiency WDM Transmission over 177-km Few-Mode Fiber,* in Optical Fiber Communication Conference/National Fiber Optic Engineers Conference 2013, OSA Technical Digest (online) (Optical Society of America), paper PDP5A.1 (2013).

[119] J. Sakaguchi, Y. Awaji, N. Wada, A. Kanno, T. Kawanishi, T. Hayashi, T. Taru, T. Kobayashi, and M. Watanabe, *109-Tb/s (7×97×172-Gb/s SDM/WDM/PDM) QPSK transmission through 16.8-km homogeneous multi-core fiber,* in Optical Fiber Communication Conference/National Fiber Optic Engineers Conference 2011, OSA Technical Digest (CD) (Optical Society of America), paper PDPB6 (2011).

[120] E. Ip, N. Bai, Y. Huang, E. Mateo, F. Yaman, S. Bickham, H. Tam, C. Lu, M. Li, S. Ten, A. P. T. Lau, V. Tse, G. Peng, C. Montero, X. Prieto, and G. Li, *88×3×112-Gb/s WDM Transmission over 50-km of Three-Mode Fiber with Inline Multimode Fiber Amplifier,* in 37th European Conference and Exposition on Optical Communications, OSA Technical Digest (CD) (Optical Society of America), paper Th.13.C.2 (2011).

[121] S. O'Keeffe, W. Zhao, W. Sun, D. Zhan, *An Optical Fibre- Based Sensor for Real-Time Monitoring of Clinical Linear Accelerator Radiotherapy Delivery,* IEEE Journal of Selected Topics in Quantum Electronics, vol. 22, 1-8 (2016).

[122] Y.J. Rao, *In-fibre Bragg grating sensors,* Meas. Sci. Technol., 8, 355–375 (1997).

[123] G F. Fernando, T. Liu, P. Crosby , C. Doyle, A. Martin, D. Brooks, B. Ralph, and R. Badcock, *A multi-purpose optical fibre sensor designed for fibre reinforced composite materials,* Meas. Sci. Technol. 8 (1997).

[124] S. H. Lieberman, S. M. Inman, G. A. Theriault, *Laser-induced fluorescence over optical fibers for real-time in situ measurements of petroleum hydrocarbons in seawater,* Proceedings Oceans 91, vol. 1, 509-514 (1991).

[125] H. Berthou and C. K. Jörgensen, *Optical-fiber temperature sensor based on upconversion-excited fluorescence,* Opt. Lett. 15 (1990).

[126] M. Plöschner, V. Kollárová, Z. Dostál, J. Nylk, T. Barton-Owen, D. E. K. Ferrier, R. Chmelík, K. Dholakia, and T. Čižmár, *Multimode fibre: Light-sheet microscopy at the tip of a needle,* Scientific Reports 5 (2015).

[127] H. Defienne, M. Barbieri, I. A. Walmsley, B. J. Smith and S. Gigan, *Two-photon quantum walk in a multimode fiber,* Sci. Adv 2 (2016).

[128] A. Mair, A. Vaziri, G. Weihs, and A. Zeilinger, *Entanglement of the orbital angular momentum states of photons,* Nature 412 (2001).

[129] M. Plöschner, T. Tyc, and T. Čižmár, *Seeing through chaos in multimode fibres,* Nat. Phot. 9 (2015).

[130] S. Randel, R. Ryf, A. Sierra, P. J. Winzer, A. H. Gnauck, C. A. Bolle, R. Essiambre, D. W. Peckham, A. McCurdy, and R. Lingle, *6×56-Gb/s mode-division multiplexed transmission over 33-km few-mode fiber enabled by 6×6 MIMO equalization,* Opt. Express 19 (2011).

[131] R. Ryf, S. Randel, A. H. Gnauck, C. Bolle, A.o Sierra, S. Mumtaz, M. Esmaeelpour, E. C. Burrows, R. Essiambre, P. J. Winzer, D. W. Peckham, A. H. McCurdy, and R. Lingle, *Mode-Division Multiplexing Over 96 km of Few-Mode Fiber Using Coherent 6×6 MIMO Processing,* J. Lightwave Technol. 30 (2012).

[132] J. Liang, Q. Mo, S. Fu, M. Tang, P. Shum, and D. Liu, *Design and fabrication of elliptical-core few-mode fiber for MIMO-less data transmission,* Opt. Lett. 41 (2016).

[133] Y. Qiu, J. Xu, K. K. Y. Wong, and K. K. Tsia, *Exploiting few mode-fibers for optical time-stretch confocal microscopy in the short near-infrared window,* Opt. Express 20, 24115-24123 (2012).

[134] T. Ahn, Y. Park, D. J. Moss, S. Ramachandran, and J. Azaña, *Frequency-domain modal delay measurement for higher-order mode fiber based on stretched pulse interference,* Opt. Lett. 33 (2008).

[135] T. Ahn, S. Moon, S. Kim, K. Oh, D. Y. Kim, J. Kobelke, K. Schuster, and J. Kirchhof, *Frequency-domain intermodal interferometer for the bandwidth measurement of a multimode fiber,* Appl. Opt. 45, 8238-8243 (2006).

[136] J. Y. Lee, T. Ahn, and D. Y. Kim, *Low coherent hybrid detection technique for differential mode delay in a multimode optical fiber,* Appl. Opt. 47, 725-730 (2008).

[137] S. E. Mechels, J. B. Schlager and D. L. Franzen, *High-resolution differential-mode delay measurements in optical fibers using a frequency-domain phase-shift technique,* IEEE Photonics Technology Letters, 794-796 (1997).

[138] Y. Painchaud, M. A. Duguay, and F. Ouellette, *Interferometric time measurements of intermodal dispersion in optical fibers by using a CCD photodetector array,* Opt. Lett. 17, 1423-1425 (1992).

[139] M. A. Itzler, M. Entwistle, U. Krishnamachari, M. Owens, X. Jiang, K. Slomkowski, S. Rangwala, *SWIR Geiger-mode APD detectors and cameras for 3D imaging*, Proc. SPIE 9114, Advanced Photon Counting Techniques VIII, 91140F (2014).

[140] A. Kanshu, C. E. Rüter, D. Kip, P. P. Beličev, I. Ilić, M. Stepić, and V. M. Shandarov, *Linear and nonlinear light propagation at the interface of two homogeneous waveguide arrays,* Opt. Express 19, 1158-1167 (2011).

[141] G. D. Valle, S. Longhi, and P. Laporta, *Discrete diffraction in waveguide arrays: A quantitative analysis by tunneling optical microscopy,* Appl. Phys. Lett. 90, 261118 (2007).

[142] S. Longhi, *Discrete diffraction and shape-invariant beams in optical waveguide arrays,* Phys. Rev. A, 033847 (2009).

[143] A. L. Jones, *Coupling of Optical Fibers and Scattering in Fibers,* J. Opt. Soc. Am. 55, 261-271 (1965).

[144] S. Somekh, E. Garmire, A Yariv, H. L. Garvin, and R. G. Hunsperger, *Channel optical waveguide directional couplers,* Appl. Phys. Lett. 22, 46–48 (1973).

[145] C. Waschke, H. G. Roskos, R. Schwedler, K. Leo, H. Kurz, and K. Köhler, *Coherent submillimeter-wave emission from Bloch oscillations in a semiconductor superlattice,* Phys. Rev. Lett. 70, 3319–3322 (1993).

[146] U.Peschel, T. Pertsch, and F. Lederer, *Optical Bloch oscillations in waveguide arrays,* Opt. Lett. 23, 1701–1703 (1998).

[147] T. Pertsch, P. Dannberg, W. Elflein, A. Bräuer, and F. Lederer, *Optical Bloch oscillations in temperature tuned waveguide arrays,* Phys. Rev. Lett. 83, 4752 (1999).

[148] G. Lenz, I. Talanina, and C. Martijn de Sterke, *Bloch oscillations in an array of curved optical waveguides,* Phys. Rev. Lett. 83, 963 (1999).

[149] N. Chiodo, G. Della Valle, R. Osellame, S. Longhi, G. Cerullo, R. Ramponi, P. Laporta, and U. Morgner, *Imaging of Bloch oscillations in erbium-doped curved waveguide arrays,* Opt. Lett. 31, 1651-1653 (2006).

[150] K. M. Davis, K. Miura, N. Sugimoto, and K. Hirao, *Writing waveguides in glass with a femtosecond laser,* Opt. Lett. 21, 1729-1731 (1996).

[151] R. R. Gattass, and E. Mazur, *Femtosecond laser micromachining in transparent materials,* Nat. Phot. 2, 219-225 (2008).

[152] M. Ams, G. D. Marshall, D. J. Spence, and M. J. Withford, *Slit beam shaping method for femtosecond laser direct-write fabrication of symmetric waveguides in bulk glasses,* Opt. Express 13, 5676-5681 (2005).

[153] S. M. Eaton, H. Zhang, M. L. Ng, J. Li, W. Chen, S. Ho, and P. R. Herman, *Transition from thermal diffusion to heat accumulation in high repetition rate femtosecond laser writing of buried optical waveguides,* Opt. Express 16, 9443-9458 (2008).

[154] N. D. Psaila, R. R. Thomson, H. T. Bookey, S. Shen, N. Chiodo, R. Osellame, G. Cerullo, A. Jha, and A. K. Kar, *Supercontinuum generation in an ultrafast laser inscribed chalcogenide glass waveguide,* Opt. Express 15, 15776-15781 (2007).

[155] S. M. Eaton, H. Zhang, P. R. Herman, F. Yoshino, L. Shah, J. Bovatsek, and Al. Y. Arai, *Heat accumulation effects in femtosecond laser-written waveguides with variable repetition rate,* Opt. Express 13, 4708-4716 (2005).

[156] J. Burghoff, S. Nolte, and A. Tünnermann, *Origins of waveguiding in femtosecond laser-structured $LiNbO_3$,* Applied Physics A, vol.89, 127-132 (2007).

[157] A. G. Okhrimchuk, A. V. Shestakov, I. Khrushchev, and J. Mitchell, *Depressed cladding, buried waveguide laser formed in a YAG:Nd^{3+} crystal by femtosecond laser writing,* Opt. Lett. 30, 2248-2250 (2005).

[158] K. Minoshima, A. M. Kowalevicz, E. P. Ippen, and J. G. Fujimoto, *Fabrication of coupled mode photonic devices in glass by nonlinear femtosecond laser materials processing,* Opt. Express 10, 645-652 (2002).

[159] A. M. Streltsov and N. F. Borrelli, *Fabrication and analysis of a directional coupler written in glass by nanojoule femtosecond laser pulses,* Opt. Lett. 26, 42-43 (2001).

[160] D. Choudhury, A. Arriola, J. R. Allington-Smith, C. Cunningham, R. R. Thomson, *Towards freeform microlens arrays for near infrared astronomical instruments,* Proc. SPIE 9151, Advances in Optical and Mechanical Technologies for Telescopes and Instrumentation, 915146 (2014).

[161] G. D. Marshall, M. Ams, and M. J. Withford, *Direct laser written waveguide-Bragg gratings in bulk fused silica,* Opt. Lett. 31, 2690-2691 (2006).

[162] R. R. Thomson, T. A. Birks, S. G. Leon-Saval, A. K. Kar, and J. Bland-Hawthorn, *Ultrafast laser inscription of an integrated photonic lantern,* Opt. Express 19, 5698-5705 (2011).

[163] S. Mukherjee, A. Spracklen, M. Valiente, E. Andersson, P. Öhberg, N. Goldman, and R. R. Thomson, *Experimental observation of anomalous topological edge modes in a slowly driven photonic lattice,* Nat. Comm. 8, 13918 (2017).

[164] S. Mukherjee, D. Mogilevtsev, G. Y. Slepyan, T. H. Doherty, R. R. Thomson, and N. Korolkova, *Dissipatively coupled waveguide networks for coherent diffusive photonics,* Nat. Comm. 8, 1909 (2017).

[165] S. Mukherjee, H. K. Chandrasekharan, P. Öhberg, N. Goldman, and R. R. Thomson, *State-recycling and time-resolved imaging in topological photonic lattices,* arXiv preprint arXiv:1712.08145 (2017).

[166] W. Huang, and H. A. Haus, *Self-consistent vector coupled-mode theory for tapered optical waveguides,* J. Lightwave Technol. 8, 922–926 (1990).

[167] B. Matthieu, M. Claire, Z. Haisu, T. Stelios and D. Pierre, *Non-diffracting states in one-dimensional Floquet photonic topological insulators,* EPL (Europhysics Letters), 119 (1), 14003 (2017).

[168] F. Dreisow, M. Heinrich, A. Szameit, S. Döring, S. Nolte, A. Tünnermann, S. Fahr, and F. Lederer, *Spectral resolved dynamic localization in curved fs laser written waveguide arrays,* Opt. Express 16, 3474-3483 (2008).